Department of Physics and Astronomy

University of Heidelberg

Master thesis

in Physics

submitted by

Anselm Klenner

born in Tuttlingen (Germany)

2015

A Study of Quench Dynamics in Ultracold Spinor Bose Gases in Comparison with Experiments

This Master thesis has been carried out by

Anselm Klenner

at the

Kirchhoff-Institut für Physik

under the supervision of

Prof. Dr. Thomas Gasenzer

Abstract

In this thesis the non-equilibrium dynamics of a three-component, ultracold Bose gas in one spatial dimension is numerically and analytically studied. Thereby two types of initial conditions are investigated. In the first case the system is prepared in the polar phase in which the magnetic-field-dependent components are initially empty. To compare the influence of vacuum fluctuations with the influence of real particles we prepare the system in the second case in a state where the side components are initially weekly occupied. In both cases an external magnetic field is applied which drives the system out of equilibrium. At early times a primary mode grows exponentially. Subsequently the particles of this mode interact with the remaining condensate and with each other and secondary modes get excited. We can calculate the momenta of these modes analytically and in the case of high densities we can also determine their growth rates. We compare our results with experiments with ^{87}Rb and find a high agreement between numerical and experimental data. In the parameter regime of the experiment the primary and the first secondary mode can be observed in the autocorrelation functions of the densities. At late times topological defects dominate the system and the spectrum falls off exponentially. The system stays for long times in a quasi-stationary state.

Zusammenfassung

In dieser Arbeit wird die Nicht-Gleichgewichts-Dynamik eines drei-komponentigen, ultrakalten Bose-Gases in einer Raumdimension numerisch und analytisch untersucht. Dabei werden zwei Arten von Anfangszuständen verglichen. In einem Fall wird das System in der polaren Phase präpariert, in der die magnetfeldabhängigen Komponenten anfangs unbesetzt sind. Um den Einfluss von Vakuumfluktuationen mit dem Einfluss von realen Teilchen zu vergleichen, wird das System im zweiten Fall in einen Zustand präpariert, in dem die Seitenkomponenten anfangs schwach besetzt sind. In beiden Fällen wird das System durch ein äußeres Magnetfeld aus dem Gleichgewicht gebracht. In der Anfangsphase kann die Anregung einer primären Mode beobachtet werden. Anschließend wechselwirken die Teilchen dieser Mode mit dem restlichen Kondensat und mit sich selbst und es werden sekundäre Moden angeregt. Die Positionen der Peaks können analytisch berechnet werden und im Falle von hoher Dichte können auch ihre Wachstumsraten bestimmt werden. Es kann eine große Übereinstimmung der numerischen Daten mit Ergebnissen von Experimenten mit ^{87}Rb gefunden werden. Mit den Parametern, die im Experiment genutzt werden, kann die primäre Mode und die erste sekundäre Mode in den Autokorrelationsfunktionen der Dichten beobachtet werden. Zu späten Zeiten wird das System von topologischen Defekten dominiert und das Spektrum fällt exponentiell ab. Das System bleibt für lange Zeiten in einem quasi-stationären Zustand.

Contents

1

Introduction

In modern physics all fundamental particles can be divided into two categories: bosons with integer spin $(0, 1, 2, \cdots)$ and fermions with odd half-integer spin $(1/2, 3/2, \cdots)$. Presumably the most important difference between them is that fermions can occupy each quantum state only once, while bosons can have any number of particles in a single quantum state. This led Satyendra Nath Bose and Albert Einstein already in 1924 to the prediction of a new state of matter for bosons [1, 2] in which a single quantum state of a system is occupied by a macroscopic number of particles. Nowadays this state is called Bose-Einstein condensate (BEC) and can be reached by cooling a gas of bosons to temperature close to absolute zero. In this case, a large fraction of particles occupy the state with the lowest energy.

The first time a BEC was created in laboratory was in 1995 [3]. ^{87}Rb atoms were captured in a magnetic trap and subsequently evaporatively cooled down below the critical temperature. This systems have the disadvantage that interactions, which change the hyperfine state of the atoms, lead to untrapped states. One can remove this limitation by using only optical traps. This was first achieved in 1998 using ^{23}N atoms [4]. Bose gases with several hyperfine states can be described in a spin basis and are therefore called spinor BEC. Above the critical temperature the condensate has a $SO(3) \times U(1)$ symmetry, which is spontaneously broken at lower temperatures. The number of ground states depends on the number of hyperfine states and can be further increased by an external magnetic field, which changes the energy of the hyperfine states. The occupation number of each magnetic sublevel can change during the time evolution via spin-changing collisions.

Today BECs are a great tool to study strongly isolated, many particle quantum systems. A high controllability gives the possibility to prepare the systems in a wide range of initial conditions and drive it subsequently out of equilibrium. This allows the study of many different non-equilibrium phenomena. They

can be used to investigate phase transitions [5, 6], prethermalised states [7, 8] and so called non-thermal fixed points (NTFP) [9–11]. Also the formation of topological defects such as solitons [12, 13], vortices [14] and domains [15, 16] can be observed. The defects can play an important role in the time evolution of the condensate [17]. It was shown that universal behavior can occur at NTFPs [11, 13, 17–19]. During the non-equilibrium dynamics many physical observables behave almost identical for a wide range of initial conditions. They only depend on the dimension of the system and the symmetry of the order parameter.

In this thesis, we concentrate on the spin-1 system in one spatial dimension. The order parameter is a vectorial quantity, whose components are given by the hyperfine states of the Bose gas. The number of hyperfine states is given by $2F + 1 = 3$, where $F = 1$ is the spin of the atoms. Without an external magnetic field this system has two different ground states [20, 21]: the anti-ferromagnetic state, in which the spin of the system vanishes, and the ferromagnetic phase, in which the spin is fully polarized and point into an arbitrary direction. If the spin of the system is conserved this can lead to domain formation [22]. A magnetic field breaks the $SO(3)$ symmetry of the system to $SO(2) \rtimes \mathbb{Z}_2$[1] and increases the number of phases in the equilibrium phase diagram to four [23].

The high number of degrees of freedom make spinor Bose gases to a very interesting system. The high amount of equilibrium ground states allow the study of various phase transitions of different order [24, 25]. Another interesting possibility is the investigation of spin turbulence [26–28]. Thereby the system can create a large number of topological defects [14] which can not occur in scalar systems such as fractional vortices [23, 29, 30]. The possibility to describe the state of the condensate using a spin basis allows the comparison with condensed matter physics [31].

In this work, we use analytic and numerical tools to study the non-equilibrium dynamics of ^{87}Rb atoms after a quench. The initial conditions and the parameters are motivated by experiments of the group of Prof. Markus Oberthaler [32]. In the experiment ^{87}Rb atoms in $F = 2$ are captured in an optical trap. High magnetic fields are used to shift the energy levels of the $m = \pm 2$ states far away from the rest of the system. For short times this modes decouple from the system and no occupation can be observed. Hence the experiment can be described effectively by a three component system. For the parameter of the effective description the system can have two different ground states depending on the external magnetic field: the polar phase, in which all particles

[1] The symbol $\rtimes$ indicates the semi-direct product. It denotes that the two symmetries are not independent, but the elements of $\mathbb{Z}_2$ have an influence on the elements of $SO(2)$.

are in $m = 0$ and the paramagnetic phase, in which all particles are equally distributed in the side modes.

In the experiment two different initial conditions are used. In the first case the particles are prepared in the polar phase, in which only the $m = 0$ hyperfine state is occupied. The side modes are initially empty and there are only vacuum fluctuations present. In the second case the system is first prepared in the polar phase and subsequently a radio-frequency-pulse is used to transfer some particles into the side modes. This corresponds in spin space to a rotation around the x-axis. In this work, we call this *seeded* initial conditions, while the first case is called *unseeded*. The idea of these two preparations is to study the differences between a classical seed with real particles and a quantum seed in which only vacuum fluctuations are present. Where possible, we compare the results of the simulations and the experiment.

The evolution of early times can be described by Bogoliubov theory [33, 34]. It can be used to calculate the infrared modes of the Bose gas. If the system is driven out of equilibrium, some of these get unstable and start to grow exponentially. This can be observed in the occupation spectra $n(k)$ of the Bose gas.

This thesis starts with Hamiltonian description of a Bose gas in the $F = 1$ and $F = 2$ states (Chap. 2). The different terms and their physical meaning are discussed. This leads to the phase diagram and the ground states of the different phases. In the end we discuss how to describe the $F = 2$ system with three components. Chap. 3 gives a short description of the experimental setup and the used parameters. Also the numerical methods and their implementation are discussed.

In Chap. 4 we take a detailed look at Bogoliubov theory for $F = 1$. After a general discussion we focus on the Bogoliubov modes of the polar phase. We find that some of them get unstable for certain magnetic fields. Thereby the momentum region of unstable modes depend on the strength of the magnetic field. In the end we compare the theory of $F = 1$ and $F = 2$ and see that they predict the same results in the early time evolution.

The numerical results for the quench from the polar phase is discussed in Chap. 5. One can observe pattern formation and the excitation of the Bogoliubov modes. This mode interact with the remaining condensate and with each other and create secondary modes, which are not predicted by Bogoliubov. These modes can grow even faster than the primary modes. Such secondary excitations can also be found studying parametric resonances in quantum field theory [35–37]. Parametric resonances can be used to describe the preheating process of the universe after inflation [38–40] or the non-equilibrium time

evolution of heavy ion collisions [41, 42]. We compare both the position and the growth rates of the modes with theory. Thereby we find that the latter depends on the density on the condensate. At later times the time evolution of the system slows down. The occupation numbers of the modes stay almost constant. The occupation spectra of all modes fall off exponentially $n(k) \sim \exp(-k^{-1})$. The system is dominated by topological defects and one can observe soliton-like excitations. In the end we compare the density-density correlations calculated in the simulations with results of the experiment. We find a high agreement between the data, if we use slightly different parameters as calculated for the experiment.

The time evolution of the seeded initial conditions shows new phenomena and is discussed in Chap. 6. In the beginning large particle oscillations between the $m = 0$ component and the two side components can be observed. They can be described in a single mode approximation, which is solved by complete elliptical integrals of the first kind [43]. The oscillation can also be seen in the experiment, where they have very similar frequencies. At later times this approximation breaks down and excitations comparable to the unseeded case can be observed. The excitations appear at later times and have slightly higher momenta. There are also new excitations, which can be explained by interactions of the small, initial condensate in the side modes with the excitations already known from the unseeded case. The comparison of the density-density correlations with results of the experiment show a high agreement, if we use the same parameters, which we used to reproduce the data in the unseeded case. In the last chapter (Chap 7) we summarize our results.

2

The System

The aim of this work is to get a better understanding of the non-equilibrium dynamics of ^{87}Rb atoms in the hyperfine states of $F = 2$ after a quench. Initially and during early states of the time evolution the $m = 2$ and $m = -2$ components are unoccupied. They decouple from the rest of the system. Hence an effective description as a spin-1 Bose-Einstein condensate with only three hyperfine states $m = -1, 0, 1$ is possible. In this chapter, we investigate both at the Hamiltonian of the $F = 1$ and $F = 2$ system and discuss the effective description of the $F = 2$ system. This leads us to the phase diagram in $F = 1$. Throughout this thesis we work in units where $\hbar = 1$.

2.1 Hamiltonian

Weakly interacting Bose-Einstein condensates are well described by non-relativistic scalar field theories. Each component of the condensate corresponds to one component of the field $\hat{\psi}_i(t, \boldsymbol{x})$. The fields fulfill the usual anticommutator relation of bosons: $[\hat{\psi}_i(t, \boldsymbol{x}), \hat{\psi}_j(t', \boldsymbol{y})] = i\delta_{i,j}\delta(t - t')\delta(\boldsymbol{x} - \boldsymbol{y})$. In this work, we want to describe the $F = 2$ system, which has five hyperfine states, by a system with only three components. Both the Hamiltonian of the five-component and of the three-component system can be divided in three parts

$$\hat{H} = \hat{H}_0 + \hat{H}_\mathrm{I} + \hat{H}_\mathrm{Z}\,. \tag{2.1}$$

$\hat{H}_0$ is the free Hamiltonian of a non-interacting particle. It consists of the kinetic term and the external potential $U(\boldsymbol{r})$. It is given by

$$\hat{H}_0 = \int \mathrm{d}\boldsymbol{r} \sum_{m=-F}^{F} \hat{\psi}_m^\dagger \left[-\frac{\nabla^2}{2M} + U(\boldsymbol{r}) \right] \hat{\psi}_m\,, \tag{2.2}$$

where M is the mass of an atom. $\hat{H}_\mathrm{I}$ is the interaction part. It can be divided in the different spin channels with total spin F_c. There are $2F$ channels and the magnetization M of each channel can take values between $-F_c$ and F_c:

$$\hat{H}_\mathrm{I} = \sum_{F_c=0}^{2F} \frac{g_{F_c}}{2} \sum_{M=-F_c}^{F_c} \langle FmFm'|F_cM\rangle \langle F_cM|F\mu F\mu'\rangle \int \mathrm{d}\boldsymbol{r}\, \hat{\psi}_m^\dagger(\boldsymbol{r})\hat{\psi}_{m'}^\dagger(\boldsymbol{r})\hat{\psi}_\mu^\dagger(\boldsymbol{r})\hat{\psi}_{\mu'}^\dagger(\boldsymbol{r})\,. \tag{2.3}$$

The Glebsch-Gordon coefficients $\langle FmFm'|F_cM\rangle \langle F_cM|F\mu F\mu'\rangle$ are needed. $\hat{H}_\mathrm{Z}$ describes the Zeeman energy of the system with the linear Zeeman effect p and the quadratic Zeeman effect q,

$$\hat{H}_\mathrm{Z} = \int \mathrm{d}\boldsymbol{r} \sum_{m=-F}^{F} \hat{\psi}_m^\dagger \left[-pm + qm^2\right] \hat{\psi}_m\,. \tag{2.4}$$

Here we rotate the coordinate system such that the magnetic field points in z-direction.

2.1.1 Interactions

The interaction part Eq. (2.3) is divided into spin channels with total spin F_c. The corresponding coupling strength is $g_{F_c} = 4\pi a_{F_c}/M$, where a_{F_c} is the s-wave scattering length of the spin channel with total spin F_c. Since we consider only s-wave scattering, all channels with odd F_c vanish. Hence we only have the case $F_c \in \{0, 2\}$ in $F = 1$ and $F_c = \{0, 2, 4\}$ in $F = 2$. It is possible to rearrange the terms to make the expression more simple. In the $F = 1$ system we obtain one term that is proportional to the square of the total density and one term that is proportional to the square of the spin of the system:

$$\hat{H}_\mathrm{I}^{F=1} = \frac{1}{2}\int \mathrm{d}\boldsymbol{r} \left[c_0 : \hat{\rho}(\boldsymbol{r})\hat{\rho}(\boldsymbol{r}) : + c_1 \sum_{\mu=x,y,z} : \hat{F}_\mu(\boldsymbol{r})\hat{F}_\mu(\boldsymbol{r}) :\right], \tag{2.5}$$

where $\hat{\rho}(\boldsymbol{r}) = \sum_i \hat{\psi}_i^\dagger(\boldsymbol{r})\hat{\psi}_i(\boldsymbol{r})$ and $:\ :$ denotes normal ordering. This means that all creation operators in this expression are on the left and all annihilation operators are on the right. We introduce the spin-independent and spin-dependent coupling constants:

$$c_0 = \frac{g_0 + 2g_2}{3} \qquad c_1 = \frac{g_2 - g_0}{3} \tag{2.6}$$

The spin vector is given by $\hat{F}_\mu = \hat{\psi}_m^\dagger f_\mu \hat{\psi}_m$, where f_μ are the spin-matrices ($\mu = x, y, z$). They full fill the spin angular momentum algebra $\mathfrak{su}(2)$: $[f_\mu, f_\nu] = i\epsilon_{\mu,\nu,\lambda} f_\lambda$. In $F = 1$ they are given by

$$f_x = \frac{1}{\sqrt{2}} \begin{pmatrix} 0 & 1 & 0 \\ 1 & 0 & 1 \\ 0 & 1 & 0 \end{pmatrix} , \; f_y = \frac{i}{\sqrt{2}} \begin{pmatrix} 0 & -1 & 0 \\ 1 & 0 & -1 \\ 0 & 1 & 0 \end{pmatrix} , \; f_z = \begin{pmatrix} 1 & 0 & 0 \\ 0 & 0 & 0 \\ 0 & 0 & -1 \end{pmatrix} \tag{2.7}$$

Therefore the spins are given by

$$\hat{F}_x = \frac{1}{\sqrt{2}} \left(\hat{\psi}_0^\dagger (\hat{\psi}_1 + \hat{\psi}_{-1}) + (\hat{\psi}_1^\dagger + \hat{\psi}_{-1}^\dagger) \hat{\psi}_0 \right) , \tag{2.8}$$

$$\hat{F}_y = \frac{i}{\sqrt{2}} \left(\hat{\psi}_0^\dagger (\hat{\psi}_1 - \hat{\psi}_{-1}) - (\hat{\psi}_1^\dagger - \hat{\psi}_{-1}^\dagger) \hat{\psi}_0 \right) , \tag{2.9}$$

$$\hat{F}_z = \hat{\psi}_1^\dagger \hat{\psi}_1 - \hat{\psi}_{-1} \hat{\psi}_{-1}^\dagger . \tag{2.10}$$

All interactions, which are included in the c_0 term, do not change the hyperfine states of the particles. On the other hand there are both spin-changing and spin-preserving interactions in the c_1 term. To see them we write down the second expression in brackets of Eq. (2.5)) explicitly:

$$c_1 : \left[2\hat{\psi}_0^\dagger \hat{\psi}_0^\dagger \hat{\psi}_1 \hat{\psi}_{-1} + 2\hat{\psi}_1^\dagger \hat{\psi}_{-1}^\dagger \hat{\psi}_0 \hat{\psi}_0 + \hat{\rho}_0 (\hat{\rho}_1 + \hat{\rho}_{-1}) + (\hat{\rho}_1 - \hat{\rho}_{-1})^2 \right] : . \tag{2.11}$$

The first two terms describe spin-changing collisions. There are only interactions allowed which preserve the total angular momentum of the system. Two atoms in the $m = 0$ state can interact so that one of them goes into the $m = 1$ and the other in the $m = -1$ state, and vice versa. In the $F = 2$ system more spin-changing interactions are possible. The last two terms describe interactions, where the hyperfine states do not change, but they also can have a strong influence on the system. The last term for example can cause the formation of spin-z domains if $c_1 < 0$.

The spin of the system depends both on the occupation and on the phases of the three modes. To get a better understanding, we look at a general normalized state ($|\psi|^2 = 1$). We can take out one global phase

$$\begin{aligned} \psi &= (\sqrt{\rho_1} e^{i\varphi_1'}, \sqrt{\rho_0} e^{i\varphi_0}, \sqrt{\rho_{-1}} e^{i\varphi_{-1}'}) \\ &= e^{i\varphi_0} (\sqrt{\rho_1} e^{i\varphi_1}, \sqrt{\rho_0}, \sqrt{\rho_{-1}} e^{i\varphi_{-1}}) , \end{aligned} \tag{2.12}$$

with ($\varphi_1 = \varphi_1' - \varphi_0, \varphi_{-1} = \varphi_{-1}' - \varphi_0$ and $\rho_m \in \mathbb{R}$). Inserting this into Eqs. (2.8)) – (2.10) results in

$$F_x = \sqrt{2}\sqrt{\rho_0}\sqrt{\rho_{-1}} \cos(\varphi_{-1}) + \sqrt{2}\sqrt{\rho_0}\sqrt{\rho_1} \cos(\varphi_1) , \tag{2.13}$$

$$F_y = \sqrt{2}\sqrt{\rho_0}\sqrt{\rho_{-1}} \sin(\varphi_{-1}) - \sqrt{2}\sqrt{\rho_0}\sqrt{\rho_1} \sin(\varphi_1) , \tag{2.14}$$

$$F_z = \rho_1 - \rho_{-1} . \tag{2.15}$$

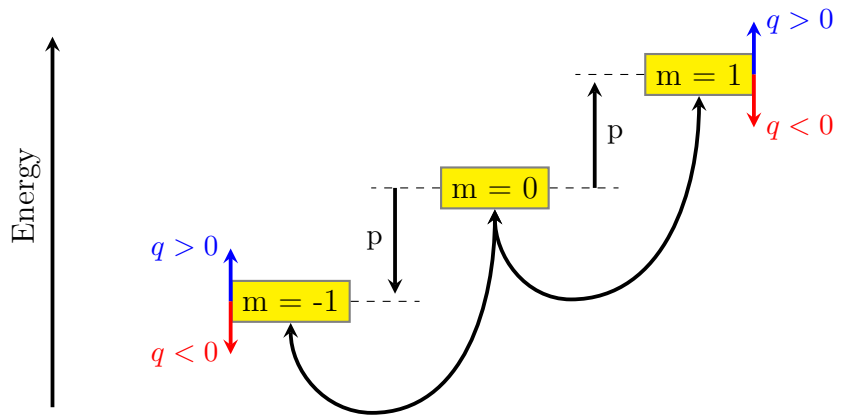

Figure 2.1: Energy levels and spin-changing interactions in $F = 1$ hyperfine splitting. The energy difference between the three hyperfine states depends on the Zeeman effect. The linear part lowers the energy of $m = -1$ by p and increases the energy of $m = -1$ by the same amount. It has no influence on the spin-changing collisions. The quadratic part q shifts energy of both side modes in the same direction. For $q < 0$ one atom in each side component has a lower Zeeman energy than two atoms in the $m = 0$ component. For $q > 0$ it is the other way around.

In contrast to the two component system, where the absolute value of the spin is always 1/2 and only the direction can change, here it is possible to have spin zero. This is for example the case for $\varphi_1 = 0, \varphi_{-1} = \pi$ and $\psi_1 = \psi_{-1}$ or for the state, in which all atoms are in the $m = 0$ component.

The states with fully polarized spin in x-,y- and z-direction are given by

$$\psi_{F_x=1} = \begin{pmatrix} 0.5 \\ \sqrt{2} \\ 0.5 \end{pmatrix}, \qquad \psi_{F_y=1} = \begin{pmatrix} 0.5 \\ i\sqrt{2} \\ -0.5 \end{pmatrix}, \qquad \psi_{F_z=1} = \begin{pmatrix} 1 \\ 0 \\ 0 \end{pmatrix}. \tag{2.16}$$

For $F = 2$ an additional term is needed to describe all interactions:

$$\hat{H}_{\mathrm{I}}^{F=2} = \hat{H}_{\mathrm{I}}^{F=1} + \frac{1}{2}\int \mathrm{d}\boldsymbol{r} \left[c_2 \hat{A}_{00}^{\dagger}(\boldsymbol{r}) \hat{A}_{00}(\boldsymbol{r})\right]. \tag{2.17}$$

There $\hat{A}_{00} = \sum_{m=-F}^{F} (-1)^{F-m} \hat{\psi}_{-m} \hat{\psi}_m$ is the singlet-pair operator proportional to a third coupling constant c_2. The coupling constants in $F = 2$ are given by

$$c_0 = \frac{4g_2 + 3g_4}{7}, \qquad c_1 = \frac{g_4 - g_2}{7}, \qquad c_2 = \frac{7g_0 - 10g_2 + 3g_4}{35}. \tag{2.18}$$

There is also a different convention, where a factor 1/5 from the coupling c_2 is already included in the definition $\hat{A}_{00}(\boldsymbol{r})$.

2.1.2 Zeeman Effect

For a suitable description of our system we have to consider the Zeeman effect up to second order. The linear effect lowers the energy of the $m = -1$ state by $p = -g_F \mu_B B$ and increase the energy of the $m = 1$ state by the same amount. B is the magnetic field, g_F the Landé g-factor, $\mu_B = e/2m_e$ the Bohr magneton, e the elementary charge and m_e the mass of the electron. Since the total spin in z-direction is conserved in our system, also the energy given by the linear Zeeman effect stays constant. The only effect of the linear Zeeman shift is a rotation of the spin vector around the magnetic field with the Larmor frequency $\omega_L = p$. By transforming into the rotating frame of reference we can neglect p. On the other hand the quadratic Zeeman-effect $q = (g_F \mu_B B)^2 / \Delta E_{hf}$ plays an important role. Here ΔE_{hf} is the hyperfine splitting energy. In $F = 1$ it shifts the energy of both side modes in the same direction. This is illustrated in Figure 2.1. A negative q lowers the energy of the side modes with respect to $m = 0$. This means that two particles in the $m = 0$ component can lower their Zeeman energy by a spin-changing collision into the side components. For positive q it is the other way around. Therefore q plays an important role for the ground state of the system (see Section 2.2).

The full Hamiltonian in $F = 1$ is given by

$$\begin{aligned}\hat{H} = \int \mathrm{d}\boldsymbol{r} \sum_{m=-1}^{1} \hat{\psi}_m^\dagger \left[-\frac{\nabla^2}{2m} + U(\boldsymbol{r}) - pm + qm^2 \right] \hat{\psi}_m \\ + \frac{c_0}{2} : \hat{\rho}(\boldsymbol{r}) \hat{\rho}(\boldsymbol{r}) : + \frac{c_1}{2} \sum_{\mu=x,y,z} : \hat{F}_\mu(\boldsymbol{r}) \hat{F}_\mu(\boldsymbol{r}) : \, . \end{aligned} \tag{2.19}$$

In the following we want to consider the case where we have no external potential $U(\boldsymbol{r}) = 0$. Then the equations of motions for the three components, which are also called Gross-Pitaevskii equations, are given by:

$$i\frac{\partial \psi_1}{\partial t} = \left(-\frac{\nabla^2}{2M} + c_0\rho + c_1 F_z - p + q \right) \psi_1 + \frac{c_1}{\sqrt{2}} (F_x - iF_y)\psi_0 \, , \tag{2.20}$$

$$i\frac{\partial \psi_0}{\partial t} = \left(-\frac{\nabla^2}{2M} + c_0\rho \right) \psi_0 + \frac{c_1}{\sqrt{2}} \left((F_x + iF_y)\psi_1 + (F_x - iF_y)\psi_{-1} \right) \, , \tag{2.21}$$

$$i\frac{\partial \psi_{-1}}{\partial t} = \left(-\frac{\nabla^2}{2M} + c_0\rho + c_1 F_z + p + q \right) \psi_{-1} + \frac{c_1}{\sqrt{2}} (F_x + iF_y)\psi_0 \, . \tag{2.22}$$

2.1.3 Effective Description of the $F = 2$ System

As already mentioned, we want to describe the early stage of the time evolution of the $F = 2$ system with only three components. Since the occupation numbers

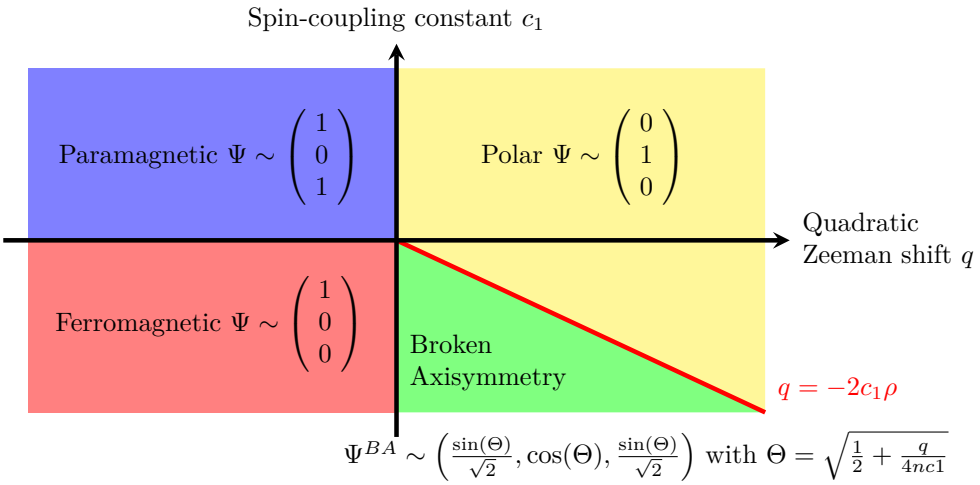

Figure 2.2: Phase diagram for the ground state in $F = 1$ without linear Zeeman effect $p = 0$, positive spin independent coupling $c_0 > 0$ and a vanishing total magnetization in z-direction $\int \mathrm{d}\boldsymbol{V}\, F_Z = 0$. The ground state depends on the spin-coupling constant c_1 and the quadratic Zeeman-effect q. There are four different phases. The phase transition between the polar phase and the broken axisymmetric phase is of second order. All other transitions are of first order.

of the $m \pm 2$ sublevels vanishes, we can neglect all terms including $\psi_{\pm 2}$. The remaining terms can also be found in the Hamiltonian of $F = 1$. We can find effective coupling constants by comparing the prefactors of these terms:

$$c_{0,\text{eff.}}^{F=1} = c_0^{F=2} + c_2^{F=2} = \frac{7g_0 + 10g_2 + 18g_4}{35}\,, \tag{2.23}$$

$$c_{1,\text{eff.}}^{F=1} = 3c_1^{F=2} - c_2^{F=2} = \frac{12(g_4 - g_2) + 7(g_2 - g_0)}{35}\,. \tag{2.24}$$

2.2 Phase Diagram

In this section, we discuss the phase diagram for the $F = 1$ system. We only consider the case where the spin independent coupling constant c_0 is positive and the total longitudinal magnetization vanishes $\langle F_z \rangle = 1/V \int \mathrm{d}\boldsymbol{V}\, F_z = 0$. Since the magnetization in z-direction is conserved, the ground state depends on the initial value of $\langle F_z \rangle$. In this work, we study initial conditions with $\langle F_z \rangle = 0$. This ensures that the total number of atoms in the side components is always equal.

If there is no external field, the system has two ground states: the ferromagnetic state for $c_1 < 0$ and the anti-ferromagnetic state for $c_1 > 0$. In the ferromagnetic ground state the spin is fully polarized and points in an arbitrary

direction. The ground state spontaneously breaks the $SO(3)$ symmetry. In the anti-ferromagnetic case the spin vanishes and the symmetry is preserved.

If an external magnetic field is applied the $SO(3)$ symmetry is explicitly broken to $SO(2) \rtimes \mathbb{Z}_2$. Here $\mathbb{Z}_2 \cong \{1, \exp(-if_x\pi)\}$ and $\rtimes$ is the semi-direct product. The system has four phases and the ground state depends on c_1 and q. For $q < 0$ the spin-changing interactions into the side modes decrease the Zeeman energy of the system and for $q > 0$ the Zeeman energy is lowered by a high occupation of $m = 0$. For $c_1 < 0$ the formation of a spin in the system is energetically preferred. For $c_1 > 0$ the ground state has no spin. Therefore the occupation of both side modes is identical. Figure 2.2 shows the phase diagram for $F = 1$.

We now want to discuss the equilibrium ground states, if an external magnetic field is applied. First we look at the case $q > 0$ and $c_1 < 0$. In the ground state all particles are in the $m = 0$. This is called the polar state

$$\Psi_{\text{Polar}} = \sqrt{\rho} \begin{pmatrix} 0 \\ e^{i\phi_0} \\ 0 \end{pmatrix}, \tag{2.25}$$

which has no magnetization. If we keep c_1 positive and go to negative q the ground state has again no spin but this time all particles are in the side modes. This is the paramagnetic phase

$$\Psi_{\text{Paramagnetic}} = \sqrt{\frac{\rho}{2}} \begin{pmatrix} e^{i\phi_1} \\ 0 \\ e^{i\phi_{-1}} \end{pmatrix}. \tag{2.26}$$

For $q < 0$ and $c_1 < 0$ also all particles are in the side mode, but a spin in the system is preferred. Hence the system creates domains, where the spin points in positive and negative z-direction. It is the ferromagnetic phase:

$$\Psi_{\text{Ferro},\uparrow} = \sqrt{\rho} \begin{pmatrix} e^{i\phi_1} \\ 0 \\ 0 \end{pmatrix} \qquad \Psi_{\text{Ferro},\downarrow} = \sqrt{\rho} \begin{pmatrix} 0 \\ 0 \\ e^{i\phi_{-1}} \end{pmatrix} \tag{2.27}$$

The last case is $q > 0$ and $c_1 < 0$. Here are two conflicting effects. Because of the negative Zeeman effect the $m = 0$ mode is energetically preferred. On the other hand the state with all particles in $m = 0$ has no spin. Therefore the system stays in the polar phase for large negative Zeeman effect $q > -2c_1\rho$. For small values $0 > q > -2c_1\rho$ the ground state of the system has a spin in the x-y-plane. The spin can point in any direction in this plane. Hence the $SO(2)$ symmetry of the system is spontaneously broken. This phase is

therefore called broken-axisymmetry phase

$$\Psi_{BA} = \sqrt{\rho} e^{i\phi_0} \begin{pmatrix} \frac{\sin(\Theta)}{\sqrt{2}} e^{-i\phi_z} \\ \cos(\Theta) \\ \frac{\sin(\Theta)}{\sqrt{2}} e^{i\phi_z} \end{pmatrix}, \tag{2.28}$$

where $\Theta = \sqrt{\frac{1}{2} + \frac{q}{4nc1}}$. ϕ_z determines the direction of the spin. The length of the spin is given by

$$|F_\mu|^2 = 1 - \left(\frac{q}{2c_1\rho}\right)^2. \tag{2.29}$$

There is a second order phase transition between the polar phase and the broken-axisymmetry phase. All other transitions are of first order.

For ^{87}Rb in $F = 1$ the spin-dependent coupling c_1 is negative. Hence its phases are described by the lower part of the diagram in Figure 2.2. On the other hand c_1 is positive in the effective description of ^{87}Rb in $F = 2$ (Eqs. (2.23) and (2.24)). Hence the ground states are described by the upper part of the diagram. In this work, we study the phase transition from the polar phase to the paramagnetic phase in detail.

3

Method

3.1 Experimental Setup and Parameters

One part of this work is the comparison of the simulations with experiments performed by the group of Prof. Markus Oberthaler [32]. In the experiments ^{87}Rb atoms in $F = 2$ are captured in a longitudinal, cigar-shaped trap. The trap frequencies in radial direction are both $\omega_\perp = 130$ Hz and the one in longitudinal direction is $\omega_\parallel = 2.2$ Hz. The radial radius of the condensate is of the order of the healing length and most excitations in these directions are frozen out (more details in Sec. 3.1.1). Therefore we can describe the Bose gas in a one dimensional framework. The density of the condensate is approximately described by a Thomas-Fermi distribution. In this approximation one assumes that all particles have zero momentum. For one dimensional system the time independent state is given by

$$(U(x) + c_0\rho(x) - \mu)\psi(x) = 0\,, \tag{3.1}$$

where $U(x) = \frac{M}{2}x^2\omega_\parallel^2$, μ is the chemical potential and we neglect the c_1 term, which is zero for our initial conditions. We get the density by setting the terms in brackets to zero

$$\rho(x) = \frac{1}{c_0}\left(\mu - \frac{M}{2}x^2\omega_\parallel^2\right)\,. \tag{3.2}$$

The roots of the density correspond to the radius of the condensate

$$R_{\mathrm{TF}} = \sqrt{\frac{2\mu}{M\omega_\parallel^2}}\,. \tag{3.3}$$

If the number of particles N in the condensate is known one can use the condition

$$\int_0^{R_{\mathrm{TF}}} \mathrm{d}x\,\rho(x) = \frac{N}{2} \tag{3.4}$$

to calculate the chemical potential μ_{TF}

$$\mu_{\mathrm{TF}} = \left(\frac{3}{4\sqrt{2}} \sqrt{M} c_0 \omega_{\parallel} N \right)^{\frac{2}{3}} . \tag{3.5}$$

In the experiment the total length of the trap is ~ 250 µm. To minimize the effects of the trap, all analyses in the experiment use only the central 125 µm. In the TF approximation the density varies by 25% in this region.

There are four parameters in the Hamiltonian Eq. (2.19), which have to be determined: The density ρ, the magnetic Zeeman effect q, the spin-independent coupling c_0 and the spin dependent-coupling c_1. The number of particles in the central area of the trap can be tuned. Typically values between 20000 – 35000 are used. There are particle losses in the experiment. The number of particle decreases by approximately 10% – 20% in 100 ms. If not stated otherwise we use in our simulations a homogeneous density corresponding to 25000 particles, which evaluates to a linear density of $200 \cdot 10^6$ m^{-1}. We compare our results mainly with experiments using a similar density.

To calculate the q value, which we use in the simulation, we have to consider not only the quadratic Zeeman effect q_{B} described in Sec. 2.1.2, but also an additional effect q_{EM} induced by a linearly polarized microwave field. The quadratic Zeeman effect shifts the energies of $m = \pm 1$ by q_B and the energies of $m = \pm 2$ by $4q_B$ with $q_B = (g_F \mu_B B)^2 / \Delta E_{\mathrm{hf}}$. For $F = 2$ we have $g_F = 1/2$ and $E_{\mathrm{hf}} = -6.8$ GHz. In the experiment high magnetic fields are used to shift the $m = \pm 2$ modes far away from the rest of the system. These modes effectively decouple from the system in the early time evolution. But it also results in high energy differences between the remaining three modes. To reduce them the additional linearly polarized microwave field is used. This field shifts the energy of the $m = 0$ state and is used to reduce the energy differences between $m = 0$ and $m = \pm 1$. It is calculated by $q_{\mathrm{EM}} = -\Omega^2/(4\delta)$. Ω is the Rabi frequency and δ the detuning. In the experiment δ is used to change $q = q_{\mathrm{B}} + q_{\mathrm{EM}}$. Typical values for q are between 0 and 30 Hz.

The coupling constants of ^{87}Rb in $F = 2$ can be calculated using Eq. (2.18). For $F = 2$ the scattering lengths are: $a_0 = 87.4 \pm 1.0\ a_{\mathrm{B}}$, $a_2 = 92.4 \pm 1.0\ a_{\mathrm{B}}$ and $a_4 = 100.5 \pm 1.0\ a_{\mathrm{B}}$ [25]. Here $a_{\mathrm{B}} = 5.29 \cdot 10^{-11}$ m is the Bohr radius. We use these values for the calculation of c_0. To get c_1 and c_2, the difference of the scattering lengths are needed. Thereby the errors, which are on the order of 1% for the scattering lengths, add up and get very large. To calculate c_1 and c_2 we use therefore direct measurements of $(a_2 - a_0) = 3.51 \pm 0.31\ a_{\mathrm{B}}$ and $(a_4 - a_2) = 6.95 \pm 0.35\ a_{\mathrm{B}}$ performed by Widera et al. [44].

The coupling constants in $F = 2$ can then be used to calculate effective coupling constants in $F = 1$ as described in Eqs. (2.23) and (2.24). Finally

^{87}Rb	c_0	c_1	c_2
$F = 1$	8.451	0.030	-
$F = 2$	8.033	0.083	-0.009
$F = 2$ eff.	8.024	0.258	-

Table 3.1: Coupling constants for ^{87}Rb in one dimensional trap with radial trap frequencies $\omega_\perp = 126$ Hz in units of $\hbar/(\mu\text{m})$. The couplings for $F = 1$, $F = 2$ and the effective description of the $F = 2$ system are given. The values are taken from [25, 44]. For $F = 1$ we used: $a_0 = 101.8 \pm 0.2\ a_\text{B}$, $a_2 = 100.4 \pm 0.1\ a_\text{B}$ and $a_2 - a_0 = -1.07 \pm 0.07\ a_\text{B}$. The values for $F = 2$ are given in the text.

one has to convert these 3D couplings into 1D couplings

$$c(1D) = \frac{c(3D)}{2\pi r_\parallel^2}\,, \tag{3.6}$$

where the radius of the condensate in vertical direction $r_\parallel = (M\omega_\perp)^{-0.5}$ is needed. The values can be found in Table 3.1. The healing length of the system depends on the density. For a density of $200 \cdot 10^6$ m^{-1} the healing length is $\zeta = 1/\sqrt{2M\rho_0 c_0} = 0.48$ µm and the spin healing length $\zeta_S = 1/\sqrt{2M\rho_0 c_1} = 2.66$ µm.

3.1.1 Validity of the 1D Description

The 1D approximation is only valid, if the condensate is confined in the vertical directions strongly enough. This requires that the chemical potential is smaller than the trap frequency

$$\frac{N a_\text{s} r_\perp}{r_\parallel^2} \ll 1\,, \tag{3.7}$$

$$r_\perp = \sqrt{\frac{1}{M\omega_\perp}} = 0.96\ \mu\text{m}\,, \tag{3.8}$$

$$r_\parallel = \sqrt{\frac{1}{M\omega_\parallel}} = 7.32\ \mu\text{m}\,, \tag{3.9}$$

where a_s is the s-wave scattering length. It is $a_\text{s} = 95.6\ a_\text{B}$ for the spin-independent and $a_\text{s} \sim 3.7\ a_\text{B}$ for the spin-dependent scattering length. For 25000 particles we get

$$\frac{N a_\text{s} r_\perp}{r_\parallel^2} = 2.27\,, \tag{3.10}$$

$$\frac{N a_\text{s} r_\perp}{r_\parallel^2} = 0.088\,. \tag{3.11}$$

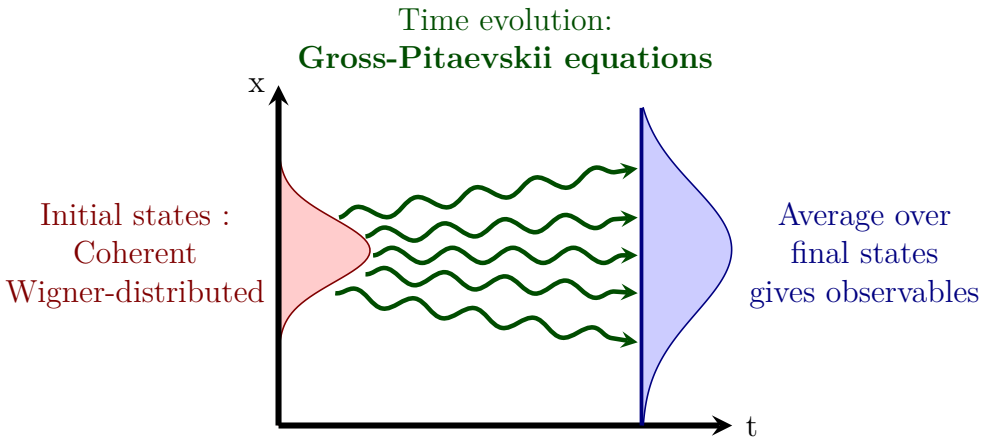

Figure 3.1: Illustration of the truncated Wigner method: The time evolution of a large sample of initial states, given by the Wigner distribution, is calculated by the Gross-Pitaevskii equation. Physical quantities are obtained by averaging over all trajectories.

Spin excitations have larger length scales than density excitations. The former are frozen out in the radial directions. However, the approximation fails for density fluctuations. We will see in Chap. 4 that the dominant excitations in our parameter regime are spin fluctuations. Some phenomena show small quantitative deviations between the experiment and the simulations. Presumably the agreement can be improved, if the finite radial extension of the trap is taken into account.

3.2 Truncated Wigner Method

In this work we simulate the time evolution of an ultracold Bose gas. Thereby we are interested in the low-momentum region of the gas where the occupation numbers of the momentum modes are high. It was shown that the time evolution of this region is very well described by classical fields [45–48]. In our simulations we use the truncated Wigner approximation (TWA) [45, 49] which is a quasi-classical, statistical approach where quantum fluctuations are included into the initial conditions but the propagation of the fields is entirely classical. The method approximates the time evolution of the Wigner function which is a unique phase space representation of the density matrix. It can be found for each density matrix by a Weyl transformation. In the limit of small temperatures the infrared modes of an ultracold Bose gas are strongly occupied and the gas is well described by a coherent state which has a positive definite Wigner function. In this case the Wigner function is a probability

distribution. Because of the uncertainty principle the Wigner function always has a finite width in phase space which corresponds to quantum fluctuations. Therefore the TWA goes beyond mean field calculations and takes a wide range of quantum effects into account. In the TWA the time evolution of the Wigner function is decomposed into the evolution of a sample of classical fields, which evolve according to the Gross-Pitaevskii equations Eqs. (2.20) – (2.22). Thereby the Wigner function gives the probability distribution of the initial states of the fields. Physical quantities are obtained by averaging over the whole sample. The described procedure is sketched in Figure 3.1.

To implement the initial states we expand the field in a series of mode functions M

$$\psi_m(\boldsymbol{r_i}) = \sum_i M_{i,m}(\boldsymbol{r_i})\alpha_{i,m}\,, \tag{3.12}$$

where α_i^2 are the coefficients of the modes. They include both the initial occupations of the modes and the quantum fluctuations. In this work we expand the field in Fourier modes to implement the initial state. We start with a perfect Bose condensate in which only the modes $M_{0,m}$ corresponding to the $k = 0$ modes are initially occupied. We have to set quantum fluctuations in all other modes $M_{j,m}$ $(j > 0)$. Therefore we set in the coefficients $\alpha_{j,m}$ $(j > 0)$ Gaussian distributed, uncorrelated noise

$$\langle \alpha_{i,m} \rangle = 0\,, \tag{3.13}$$

$$\langle \alpha_{j,n}\alpha_{i,m} \rangle = \frac{1}{2}\delta_{n,m}\delta_{i,j}\,. \tag{3.14}$$

The average occupation corresponds to half a particle per mode.

3.3 Numerical Implementation

In this work, we solve the equations of motion (2.20) – (2.22) for the three condensates numerically. A one dimensional grid consisting of either $N_S = 16384$ or $N_s = 8192$ grid points and periodic boundary conditions is used. The distance between two grid points has to be smaller than the condensate healing length, which is the smallest physical length scale of the system. The number of grid points corresponding to the healing length varies in this work but we use at least $\xi \approx 8$ grid points.

To simulate the time evolution we use the split step method, which keeps the energy and the particle number of the system numerically conserved to double precision. This method takes advantage of the fact that the kinetic part of

the Hamiltonian is diagonal in momentum space, while the potential energy part is diagonal in position space. The Hamiltonian is divided into two parts: $H = T + V$. T is the kinetic energy

$$T_{i,j} = \delta_{i,j} \frac{\Delta^2}{2M} \tag{3.15}$$

and V includes the Zeeman effect, the interactions and, if present, the trap $U(\boldsymbol{r})$:

$$V = \begin{pmatrix} c_0\rho + q + c_1 F_z + U(\boldsymbol{r}) & \frac{c_1}{\sqrt{2}}(F_x - iF_y) & 0 \\ \frac{c_1}{\sqrt{2}}(F_x + iF_y) & c_0\rho + U(\boldsymbol{r}) & \frac{c_1}{\sqrt{2}}(F_x - iF_y) \\ 0 & \frac{c_1}{\sqrt{2}}(F_x + iF_y) & c_0\rho + q - c_1 F_z + U(\boldsymbol{r}) \end{pmatrix}. \tag{3.16}$$

Using the Baker-Campbell-Hausdorff formula we can approximate the time evolution as follows:

$$\begin{aligned} \psi_i(\boldsymbol{r}, t + \Delta t) &= e^{-iH_{i,j}\Delta t}\psi_j(\boldsymbol{r}, t) \\ &= e^{-iT_{i,k}\Delta t/2} e^{-iV_{k,l}\Delta t} e^{-iT_{l,j}\Delta t/2}\psi_j(\boldsymbol{r}, t) + \mathcal{O}(\Delta t)^3)\,. \end{aligned} \tag{3.17}$$

The two exponential parts including T can be easily calculated in Fourier space, where we simply have $T = k^2/(2M)$. Here we can use the very effective "Fast Fourier Transformation" (FFT) [50] to switch between real and Fourier space. This algorithm stays very fast for large grids. The time needed to transform a grid with n grid points scales as $\mathcal{O}(n \log(n))$. The algorithm for the multiplication with $\exp(-iV\Delta t)$ is more complicated. Here we sketch it only briefly: In each time step the eigenvalues of V are calculated using a numerical stable expression taken from McKelvey [51, 52]. Then one can use Putzer algorithm [53], which gives an explicit expression for all nine matrix elements $(e^{-iV\Delta t})_{i,j}$. More details to this method can be found in the work of S. Heupts [54], who implemented a large extend of the used code. Since each time step begins and ends with the multiplication of $e^{-iT_{l,j}\Delta t/2}$ one can combine the end of one time step with the beginning of the next. Hence only two Fourier transformations and two matrix multiplications are needed for each time step.

It turns out that the ratio of the number of real particles N_0 to the number of particles added to simulation through the quantum noise N_{Noise},

$$R = \frac{N_0}{N_{\text{Noise}}}\,, \tag{3.18}$$

is an important quantity. For small values of R the quantum noise is more important. Mean field descriptions break down at earlier times and the system

is more chaotic. Also excitation of modes can be seen earlier. On the other hand for large R the quantum noise is less important and the system gets more classical. The system stays very regular for long times and all phenomena can be seen more clearly. There are several different methods to set the noise and also to simulate the influence of the noise on the real particles. A good overview can be found in [45]. In the method described in Eqs. (3.13) and (3.14) for each mode on average half a particle is added to the system. During the simulation this particles are treated like real particles and thus add energy to the system. To improve the simulation we can introduce a cutoff and therefore reduce the number of particles implemented through the noise. This is possible, because high momentum modes have no influence on the time evolution in the infrared. We choose a resolution independent cutoff and only occupy modes up to twice the inverse of the healing length.

Using this method and the density of the experiment the value of $R \approx 15$ is quiet small. Here we want to point out that this should not be a prediction for the importance of the noise in the experiment. The modes in the trap are different from the modes used in the simulations. In addition there are also other factors in experiments which play an important role like the finite temperature of the condensate and effects of the trap or from external fields. They are not included in the simulation. It turns out that simulations with $R \approx 15$ agree quite well with the results in the experiment. To study the influence of the quantum noise on our results, we repeat our simulations with higher densities. Thereby we lower the coupling constants such that the healing length $\zeta \sim c_i \rho$ stays the same. For large R most phenomena are more pronounced. It is easier to compare them with analytic approximations. We can therefore use this method to get a better understanding of the physics happening in the system. On the other hand the results of simulations with small R are closer at the experimental results.

4

Bogoliubov theory

In this chapter, we describe the Bogoliubov method [33, 55, 56]. It can be used to calculate the lowest lying modes of a weakly interacting, ultracold Bose gas. If the system is driven out of equilibrium, the eigenvalues of the energy of some of the modes become imaginary. These modes start to grow exponentially. The method is based on a mean field approximation and is only true for short times.

4.1 Bogoliubov Approximation in $F = 1$

We start the calculation with the Hamiltonian (2.19) and only consider the homogeneous case $U(\boldsymbol{r}) = 0$. We expand the field operators in terms of annihilation $\hat{a}_{\boldsymbol{k},m}$ and creation operators $\hat{a}^\dagger_{\boldsymbol{k},m}$ in the momentum basis of the three condensates. They are given by

$$\hat{\psi}_m(\boldsymbol{r}) = \frac{1}{\sqrt{V}} \sum_{\boldsymbol{k}} \hat{a}_{\boldsymbol{k},m} e^{i\boldsymbol{k}\cdot\boldsymbol{x}} \,, \tag{4.1}$$

$$\hat{\psi}^\dagger_m(\boldsymbol{r}) = \frac{1}{\sqrt{V}} \sum_{\boldsymbol{k}} \hat{a}^\dagger_{\boldsymbol{k},m} e^{-i\boldsymbol{k}\cdot\boldsymbol{x}} \,. \tag{4.2}$$

The ladder operator fulfill the bosonic commutator relations $[\hat{a}_{\boldsymbol{k},d}, \hat{a}^\dagger_{\boldsymbol{k'},d'}] = \delta_{d,d'}\delta(\boldsymbol{k'} - \boldsymbol{k})$. Inserting this into the Hamiltonian gives:

$$\begin{aligned} \hat{H} = &\sum_{\boldsymbol{k}} (\epsilon_{\boldsymbol{k}} - pm + qm^2) \hat{a}^\dagger_{\boldsymbol{k},m} \hat{a}_{\boldsymbol{k},m} \\ &+ \frac{c_0}{2V} \sum_{\boldsymbol{p},\boldsymbol{k},\boldsymbol{q}} \hat{a}^\dagger_{\boldsymbol{p},m} \hat{a}^\dagger_{\boldsymbol{k},m'} \hat{a}_{\boldsymbol{k}-\boldsymbol{q},m} \hat{a}_{\boldsymbol{k}+\boldsymbol{q},m'} \\ &+ \frac{c_1}{2V} \sum_{\boldsymbol{p},\boldsymbol{k},\boldsymbol{q}} \boldsymbol{f}_{m,m'} \boldsymbol{f}_{\mu,\mu'} \hat{a}^\dagger_{\boldsymbol{p},m} \hat{a}^\dagger_{\boldsymbol{k},\mu} \hat{a}_{\boldsymbol{k}-\boldsymbol{q},m'} \hat{a}_{\boldsymbol{k}+\boldsymbol{q},\mu'} \,, \end{aligned} \tag{4.3}$$

where we introduced $\epsilon_{\boldsymbol{k}} = \boldsymbol{k}^2/2M$. The integration over d$\boldsymbol{r}$ is already performed, where we used $\int_V d\boldsymbol{r} \exp(i(\boldsymbol{k'} - \boldsymbol{k})\boldsymbol{r}) = V\delta_{\boldsymbol{k'},\boldsymbol{k}}$. The Kronecker delta removes one summation in each term. We can now use the fact that the $\boldsymbol{k} = 0$ mode is macroscopically occupied in an ultracold Bose gas. We can replace $\hat{a}_{\boldsymbol{0},m}$ and $\hat{a}^\dagger_{\boldsymbol{0},m}$ by $\mathbb{C}$-numbers $\sqrt{N_0}\zeta_m$, where $|\zeta_m|^2 = 1$ and N_0 is the number of particles with $\boldsymbol{k} = 0$. The total number of particles N is given by

$$N = N_0 + \sum_{k\neq 0,m} \hat{n}_{\boldsymbol{k},m} \,, \tag{4.4}$$

where $\hat{n}_{\boldsymbol{k},m} = \hat{a}^\dagger_{\boldsymbol{k},m}\hat{a}_{\boldsymbol{k},m}$. The next approximation is to keep only terms up to second order in the remaining ladder-operators. Because the interactions are weak and the occupation number of modes with $\boldsymbol{k} \neq 0$ is small, terms of higher order can be neglected. After these approximations the Hamiltonian is not diagonal anymore in the $\hat{a}_{\boldsymbol{k},m}$, $\hat{a}^\dagger_{\boldsymbol{k},m}$ basis and includes terms $\hat{a}^\dagger_{\boldsymbol{k},m}\hat{a}^\dagger_{\boldsymbol{k},m}$ and $\hat{a}_{\boldsymbol{k},m}\hat{a}_{\boldsymbol{k},m}$:

$$\begin{aligned}
\hat{H}_{\text{eff}} = \frac{Vn^2}{2}\Big(c_0 + c_1 \langle \boldsymbol{F}\rangle^2 - pN\langle F_z\rangle + qN\left\langle F_z^2\right\rangle\Big) \\
+ \sum_{\boldsymbol{k}\neq 0}\Big[\Big(\epsilon_{\boldsymbol{k}} - nc_1\langle \boldsymbol{F}\rangle^2 - p(m - \langle F_z\rangle) + q(m^2 - \left\langle F_z^2\right\rangle)\Big)\hat{a}^\dagger_{\boldsymbol{k},m}\hat{a}_{\boldsymbol{k},m} \\
+ nc_1\langle \boldsymbol{F}\rangle \boldsymbol{F}_{m,m'}\hat{a}^\dagger_{\boldsymbol{k},m}\hat{a}_{\boldsymbol{k},m'} \\
+ \frac{nc_0}{2}(2\hat{D}^\dagger_{\boldsymbol{k}}\hat{D}_{\boldsymbol{k}} + \hat{D}_{\boldsymbol{k}}\hat{D}_{-\boldsymbol{k}} + \hat{D}^\dagger_{\boldsymbol{k}}\hat{D}^\dagger_{-\boldsymbol{k}}) \\
+ \frac{nc_1}{2}(2\hat{\boldsymbol{\mathcal{F}}}^\dagger_{\boldsymbol{k}}\hat{\boldsymbol{\mathcal{F}}}_{\boldsymbol{k}} + \hat{\boldsymbol{\mathcal{F}}}_{\boldsymbol{k}}\hat{\boldsymbol{\mathcal{F}}}_{-\boldsymbol{k}} + \hat{\boldsymbol{\mathcal{F}}}^\dagger_{\boldsymbol{k}}\hat{\boldsymbol{\mathcal{F}}}^\dagger_{-\boldsymbol{k}})\Big] \,,
\end{aligned} \tag{4.5}$$

where we introduced new quantities to simplify the expression:

$$\langle \boldsymbol{F}\rangle = \boldsymbol{f}_{m,m'}\zeta^*_m\zeta_{m'} \,, \tag{4.6}$$

$$\hat{D}_{\boldsymbol{k}} = \zeta^*_m\hat{a}_{\boldsymbol{k},m} \,, \tag{4.7}$$

$$\hat{\boldsymbol{\mathcal{F}}}_{\boldsymbol{k}} = \boldsymbol{f}_{m,m'}\zeta^*_m\hat{a}_{\boldsymbol{k},m'} \,, \tag{4.8}$$

$$n = \frac{N}{V} \,. \tag{4.9}$$

$\hat{D}_{\boldsymbol{k}}$ describes density fluctuations and $\hat{\boldsymbol{\mathcal{F}}}_{\boldsymbol{k}}$ spin fluctuations. We now have to find a new basis $\hat{b}_{\boldsymbol{k},d}, \hat{b}^\dagger_{\boldsymbol{k},d}$, in which the Hamiltonian is diagonal. The operators of the new basis also have to satisfy the commutation relation $[\hat{b}_{\boldsymbol{k},d}, \hat{b}^\dagger_{\boldsymbol{k'},d'}] = \delta_{d,d'}\delta(\boldsymbol{k'} - \boldsymbol{k})$. Therefore the transformation has to be symplectic. The eigenvectors of this basis are called Bogoliubov modes and describe the excitations of the ground state. The change of basis is called a Bogoliubov transformation.

4.2 Bogoliubov Modes in the Polar Phase

The Hamiltonian (4.5) gets much simpler, if one looks at a specific ground state. In this work, we are interested in the Bogoliubov modes of the polar phase in $F = 1$. Hence we can set $\zeta = (0, 1, 0)$. The polar ground state has no spin and $\langle \boldsymbol{f} \rangle = 0$. We can also neglect $p = 0$ by transforming to the rotating frame of reference. This results in

$$\begin{aligned}\hat{H}_{\text{eff}}^{\text{polar-phase}} =& \frac{V n^2 c_0}{2} + \sum_{\boldsymbol{k}\neq 0} \Big[(\epsilon_{\boldsymbol{k}} + nc_0)\, \hat{a}^\dagger_{\boldsymbol{k},0} \hat{a}_{\boldsymbol{k},0} + \frac{nc_0}{2} (\hat{a}_{\boldsymbol{k},0} \hat{a}_{-\boldsymbol{k},0} + \hat{a}^\dagger_{\boldsymbol{k},0} \hat{a}^\dagger_{-\boldsymbol{k}.0}) \\ &+ (\epsilon_{\boldsymbol{k}} + q + nc_1)\, (\hat{a}^\dagger_{\boldsymbol{k},f_x} \hat{a}_{\boldsymbol{k},f_x} + \hat{a}^\dagger_{\boldsymbol{k},f_y} \hat{a}_{\boldsymbol{k},f_y}) \\ &+ \frac{nc_1}{2} (\hat{a}^\dagger_{\boldsymbol{k},f_x} \hat{a}^\dagger_{-\boldsymbol{k},f_x} + \hat{a}^\dagger_{\boldsymbol{k},f_y} \hat{a}^\dagger_{-\boldsymbol{k},f_y} + \hat{a}_{\boldsymbol{k},f_x} \hat{a}_{-\boldsymbol{k},f_x} + \hat{a}_{\boldsymbol{k},f_y} \hat{a}_{-\boldsymbol{k},f_y}) \Big] \,, \end{aligned} \tag{4.10}$$

where we introduced two new operators, which describe F_x and F_y excitations:

$$\hat{a}_{\boldsymbol{k},f_x} = \frac{1}{\sqrt{2}} (\hat{a}_{\boldsymbol{k},1} + \hat{a}_{\boldsymbol{k},-1}) \,, \tag{4.11}$$

$$\hat{a}_{\boldsymbol{k},f_y} = \frac{i}{\sqrt{2}} (\hat{a}_{\boldsymbol{k},1} - \hat{a}_{\boldsymbol{k},-1}) \,. \tag{4.12}$$

We can diagonalize the Hamiltonian by a Bogoliubov transformation into the following basis:

$$\hat{b}_{\mathbf{k},0} = \sqrt{\frac{\epsilon_{\boldsymbol{k}} + nc_0 + \omega_{\boldsymbol{k},0}}{2\omega_{\boldsymbol{k},0}}} \hat{a}_{\mathbf{k},0} + \sqrt{\frac{\epsilon_{\boldsymbol{k}} + nc_0 - \omega_{\boldsymbol{k},0}}{2\omega_{\boldsymbol{k},0}}} \hat{a}^\dagger_{-\mathbf{k},0} \,, \tag{4.13}$$

$$\hat{b}_{\mathbf{k},j} = \sqrt{\frac{\epsilon_{\boldsymbol{k}} + q + nc_1 + \omega_{\boldsymbol{k},f}}{2\omega_{\boldsymbol{k},f}}} \hat{a}_{\mathbf{k},j} + \sqrt{\frac{\epsilon_{\boldsymbol{k}} + q + nc_1 - \omega_{\boldsymbol{k},f}}{2\omega_{\boldsymbol{k},f}}} \hat{a}^\dagger_{-\mathbf{k},j} \,, \tag{4.14}$$

with $j \in \{f_x, f_y\}$. These operators fulfill the commutator relations. There are three different modes. The first mode is massless, because the ground state spontaneously breaks the $U(1)$ gauge symmetry of the system. It describes density fluctuations in the $m = 0$ component. The two other modes are degenerated and describe spin fluctuations. They are massive, if $q \neq 0$. The magnetic field breaks the rotational symmetry around the x- and y-axis. The eigenenergies ω_i of the modes are given by

$$\omega_0^2(\boldsymbol{k}) = \epsilon_{\boldsymbol{k}} \left(\epsilon_{\boldsymbol{k}} + 2nc_0\right) \,, \tag{4.15}$$

$$\omega_f^2(\boldsymbol{k}, q) = (\epsilon_{\boldsymbol{k}} + q) \left(\epsilon_{\boldsymbol{k}} + q + 2nc_1\right) \,. \tag{4.16}$$

$\omega_0^2(\boldsymbol{k})$ does not depend on q and is in our case always positive. However, $\omega_f^2(\boldsymbol{k}, q)$ becomes negative for some $\boldsymbol{k}$ if $q < 0$. The eigenenergies of the modes with

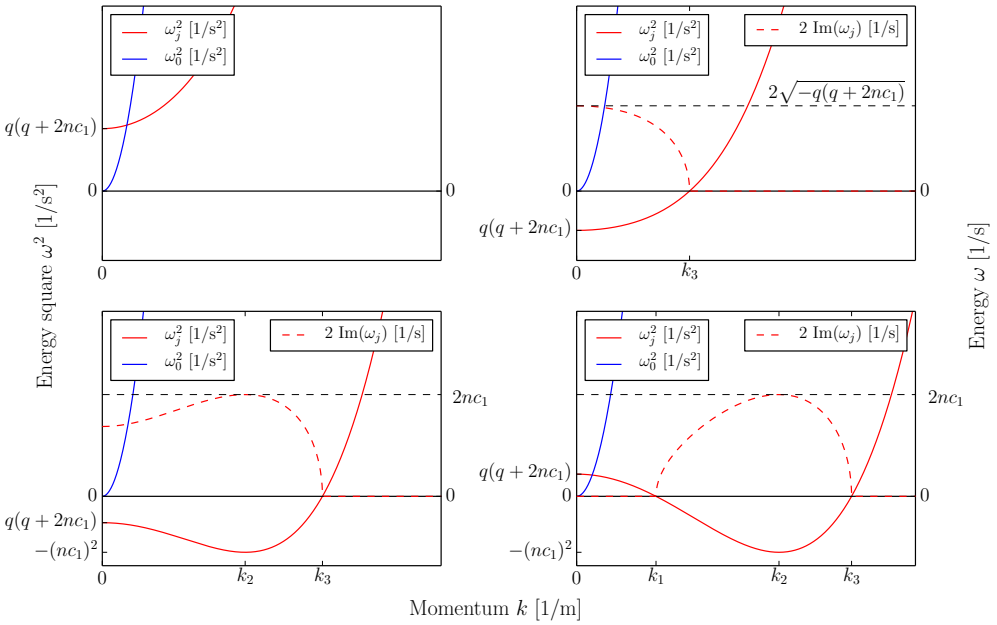

Figure 4.1: Eigenenergies of the Bogoliubov modes of the polar phase for the four different regimes: $q > 0$ (upper left), $0 < -q < nc_1$ (upper right), $nc_1 < -q < 2nc_1$ (lower left) and $2nc_1 < -q$ (lower right). The labeled momenta are given by: $k_1 = \sqrt{-2M(q+2nc_1)}$, $k_2 = \sqrt{-2M(q+nc_1)}$ and $k_3 = \sqrt{-2Mq}$. Solid lines show the square of the eigenenergies for the density fluctuations (blue) and the degenerated pair of spin fluctuations (red). For $q < 0$ the spin fluctuations have an unstable region where the eigenenergies are imaginary. In the early stages of the time evolution these modes grow exponentially with a growth rate of 2 Im(ω) (dashed line). For $0 < -q < nc_1$ the most unstable mode is at $\boldsymbol{k}^2_{\text{m.u.}} = 0$ and for $-q > nc_1$ it is at $\boldsymbol{k}^2_{\text{m.u.}} = -2M(q+nc_1)$. For $2nc_1 < -q$ the region of unstable modes does not include $\boldsymbol{k} = 0$ anymore. In this case, we can see the Bogoliubov modes as clear peaks in the spectra.

the corresponding momenta become imaginary. The time evolution operator of the modes is given by $U(t,t_0) = \sum_n \exp\left(-iE_n(t-t_0)\right)|n\rangle\langle n|$. This means that the modes with imaginary eigenvalues grow exponentially. This is only valid in the early stage of the time evolution. The approximation breaks down, if non-linear effects become important.

We now further analyze Eq. (4.16): In the effective description of ^{87}Rb in $F = 2$ we have positive c_1. The ground state of the polar phase is stable for positive q. For negative q the spin modes become unstable. The minimum of $\omega_f^2(\boldsymbol{k}, q)$ corresponds to the most unstable mode. For the region $0 < -q < nc_1$ the most

unstable mode is at $\boldsymbol{k}_{\text{m.u.}} = 0$. For higher magnetic fields the minimum is at:

$$\boldsymbol{k}^2_{\text{m.u.}} = -2M(q + nc_1) \tag{4.17}$$

In this case, the kinetic energy of the most unstable mode corresponds to the energy, which a single pair of atoms would get by scattering from $m = 0$ to the side components and thereby creating a spin excitation. Each atom gets the Zeeman energy $-q$ and needs the energy nc_1 for the creation of the spin. Therefore we have

$$\frac{k^2}{2M} = -q - nc_1\,. \tag{4.18}$$

The region of unstable modes can be found by calculating the roots of $\omega_f^2(\boldsymbol{k}, q)$. One can distinguish between two cases:

$$\left[0, \sqrt{-2Mq}\right]\,, \qquad \text{for } 0 < -q < 2nc_1\,, \tag{4.19}$$

$$\left[\sqrt{-2M(q + 2nc_1)}, \sqrt{-2Mq}\right]\,, \qquad \text{for } 2nc_1 < -q\,. \tag{4.20}$$

In our simulations we do not only see the growth of the Bogoliubov modes, but also of further modes. These excitations are generated by interactions of the Bogoliubov modes with the remaining condensate. To see secondary excitations clearly it is of advantage to have a small region of non-trivial Bogoliubov modes. Hence $k_2 - k_1 = \sqrt{2M}(\sqrt{q + 2nc_1} - \sqrt{q})$ has to be small. This is the case for small nc_1 and for large q.

The Bogoliubov method do not only predict the momenta of the modes, but also their growth rates. They given by two times the imaginary part of the eigenenergy. The growth rate of the most unstable mode $k_{\text{m.u.}}$ is

$$\tau^{-1}_{\text{Bog}} = 2\ \text{Im}(\omega(k_{\text{m.u.}})) = 2\ \text{Im}\left(\sqrt{q^2 + 2nc_1 q}\right)\,, \qquad \text{for } 0 < -q < nc_1\,, \tag{4.21}$$

$$\tau^{-1}_{\text{Bog}} = 2\ \text{Im}(\omega(k_{\text{m.u.}})) = 2nc_1\,, \qquad \text{for } nc_1 < -q\,. \tag{4.22}$$

It depends on q and nc_1. We can compare this value with our numerical results and we can also use to predict the growth rate of secondary excitations.

4.3 Comparison with Bogoliubov in F=2

The state, in which all particles are in $m = 0$ is also a ground state of the $F = 2$ system. It is called the uniaxial nematic phase. We now compare the

Bogoliubov modes of the polar phase with the modes of the uniaxial nematic phase. One can find five modes with the energies

$$(\omega_0^{F=2})^2(\boldsymbol{k}) = \epsilon_{\boldsymbol{k}}\left(\epsilon_{\boldsymbol{k}} + 2n(c_0^{F=2} + c_2^{F=2})\right) , \tag{4.23}$$

$$(\omega_f^{F=2})^2(\boldsymbol{k}, q) = (\epsilon_{\boldsymbol{k}} + q)\left(\epsilon_{\boldsymbol{k}} + q + 2n(3c_1^{F=2} - c_2^{F=2})\right) , \tag{4.24}$$

$$\omega_\pm^2(\boldsymbol{k}, q) = (\epsilon_{\boldsymbol{k}} + 4q)\left(\epsilon_{\boldsymbol{k}} + 4q - 2nc_2\right) . \tag{4.25}$$

If one introduces the effective coupling constants: Eqs. (2.23) and (2.24), the first three eigenenergies are identical to the energies of the three modes in the $F = 1$ system and also the eigenvectors are the same. The last two modes are degenerated and cannot be found in the $F = 1$ system. They describe excitations into the $m = \pm 2$ components. The corresponding eigenvectors are given by

$$\hat{b}_{\mathbf{k},\pm} = \sqrt{\frac{\epsilon_{\boldsymbol{k}} + 4q - nc_2 + \omega_{\boldsymbol{k},\pm}}{\omega_{\boldsymbol{k},\pm}}}\hat{a}_{\mathbf{k},\pm} - \sqrt{\frac{\epsilon_{\boldsymbol{k}} + 4q - nc_2 - \omega_{\boldsymbol{k},\pm}}{\omega_{\boldsymbol{k},\pm}}}\hat{a}^\dagger_{-\mathbf{k},\pm} , \tag{4.26}$$

where we introduced the operators

$$\hat{a}_{\boldsymbol{k},\pm} = \frac{1}{\sqrt{2}}(\hat{a}_{\boldsymbol{k},2} \pm \hat{a}_{\boldsymbol{k},-2}) . \tag{4.27}$$

In our case c_2 is negative and there is a region of unstable modes for $-nc_2/4 < -q$. The growth rate of the most unstable mode ($k^2_{\text{m.u.}} = 2nc_2 - 8q$) is

$$\tau^{-1}_{\text{Bog}} = 2\ \text{Im}(\omega_\pm(k_{\text{m.u.}})) = 2nc_2 \tag{4.28}$$

In ^{87}Rb we have $c_1 \approx 30|c_2|$. This means that the growth rate of the $\hat{b}_{\mathbf{k},\pm}$ modes is very small in comparison with the growth rate of the of the spin excitations in the $m = \pm 1$ modes. It explains why the occupation of the $m = \pm 2$ hyperfine states is negligible during the early stage of the time evolution and why an effective description, in which only the $m = -1, 0, 1$ modes are considered, is sufficient.

5

Unseeded Initial Conditions

In this chapter, we study the quench from the polar state into the paramagnetic regime. Initially all particles are prepared in the $m = 0$ component. In the experiment this can be achieved by a Stern-Gerlach splitting which removes all particles in the hyperfine states $m = \pm 1$. The system is then driven out of equilibrium by an instantaneous quench, which lowers the energy of the side components by q through the quadratic Zeeman effect. The new ground state of the system is the paramagnetic state, in which half of the particles are in $m = 1$ and the other half in $m = -1$:

$$\hat{\psi}_{\text{g.s.}} = \sqrt{\rho} \begin{pmatrix} 0 \\ e^{i\phi_0} \\ 0 \end{pmatrix} \xrightarrow[q<0]{\text{quench}} \hat{\psi}_{\text{g.s.}} = \sqrt{\frac{\rho}{2}} \begin{pmatrix} e^{i\phi_1} \\ 0 \\ e^{i\phi_{-1}} \end{pmatrix} .$$

We are particularly interested in the non equilibrium time evolution of the system. A sensible quantity to observe the behavior of the system after the quench is the occupation number

$$n^{(m)}(k,t) = \int d^{d-1}\Omega_d(\boldsymbol{k}) \left\langle \Psi_m^*(\boldsymbol{k},t)\Psi_m(\boldsymbol{k},t) \right\rangle_{\text{ensemble}} \tag{5.1}$$

of the different momentum modes k, where $k = |\boldsymbol{k}|$ is the radial momentum and $\Omega_d(\boldsymbol{k})$ denotes the phase space volume of mode k. In one dimension this reduces to the summation over the two modes k and $-k$. Here one has to keep in mind that on the finite grid the momenta in Fourier space are not linear distributed. There are more details in Appendix A.2.

In the experiments the momentum distributions of the three components cannot be measured directly. Instead the components can be separated by a Stern-Gerlach splitting. After this the density distribution can be measured. We therefore also calculate the Fourier transformation of the density

$$G_{\rho,\rho}^{(m)}(k,t) = \int d^{d-1}\Omega_d(\boldsymbol{k}) \left\langle \rho_m^*(\boldsymbol{k},t)\rho_m(\boldsymbol{k},t) \right\rangle_{\text{ensemble}} . \tag{5.2}$$

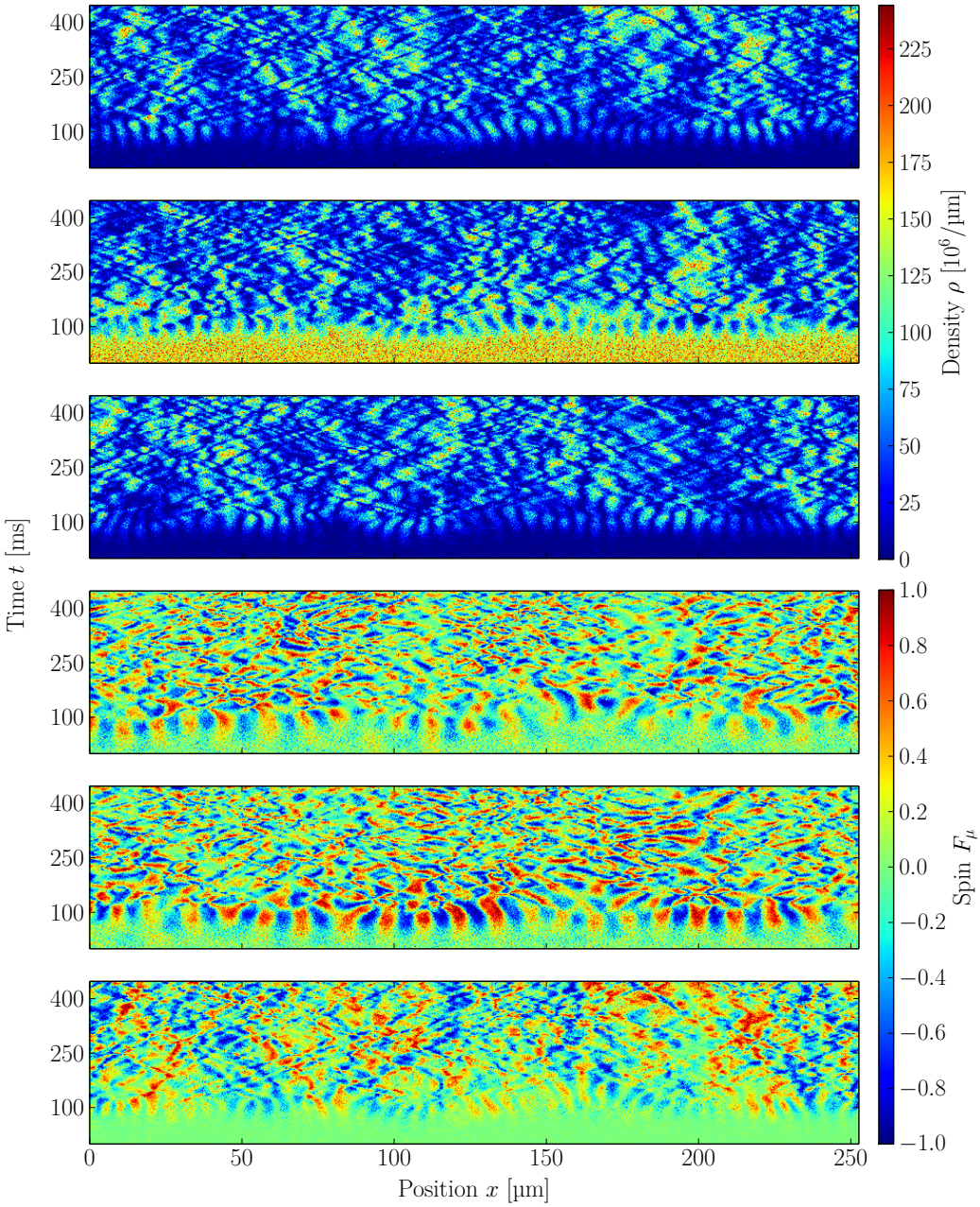

Figure 5.1: Numerical results of a single realization in position space for the unseeded initial conditions. The parameters are: $\rho = 200 \cdot 10^6$ m^{-1}, $N_s = 8192$, $L = 252.2$ µm, $q = -25$ Hz $= -3.04 \cdot nc_1$, c_0 and c_1 are given in Tab. 3.1. The first three plots show the density of the three components $m = 1$ (top), $m = 0$ (middle) and $m = -1$ (bottom). The last three plots show F_x (top) F_y (middle) and F_z (bottom). After ≈ 50 ms a pattern with a wavelength given by the Bogoliubov modes starts to appear. Particles from the $m = 0$ component scatter into the side components creating thereby a spin in x- and y-direction. They are most pronounced at $t \approx 100$ ms. Shortly after this also a pattern in F_z is visible. In addition to the Bogoliubov modes there are also long-wave excitations in F_z

In the previous chapter, we have found the modes, which get excited after the quench. These modes can be seen as peaks in $n^{(m)}(k,t)$. Although the density is just the absolute square of the wave function $\rho(\boldsymbol{r}) = \psi^*(\boldsymbol{r})\psi(\boldsymbol{r})$ the Fourier spectra of both quantities can look very different. This is important, when we want to make prediction for the form of $G^{(m)}_{\rho,\rho}(k,t)$. Therefore we have a closer look at the relation between wave function and density in the Appendix A.1.

Another interesting quantity is the spin of the condensate Eqs. (2.8) – (2.10). As we have seen in Sec. 4.2, we expect spin excitations in the system. Their momenta can be seen in the Fourier transformation of the spin. Another observable, which can be used to describe the system, are the quadrupole moments

$$Q_{i,j} = \hat{\psi}^\dagger_m (f_i f_j + f_j f_i - \frac{4}{3}\delta_{i,j})_{m,n} \hat{\psi}_n \,. \tag{5.3}$$

We start our analysis with the parameters given in experiment but we also analyze simulations with higher densities, in which some phenomena are more pronounced.

5.1 Evolution of a Single Realization in Real Space

At first we take a look at the real space evolution of a single realization. Figure 5.1 shows the density of all three components and the spin at each lattice site. The spatial volume is $L \approx 250$ µm, which is roughly the longitudinal width of the trap in experiment. We use $q = 25$ Hz to be in a regime where we expect the excitations with momenta $k \neq 0$. One can see that in the beginning most particles stay in $m = 0$ and the system has no spin. After ≈ 50 ms first excitations are visible. Particles in $m = 0$ scatter into pairs of atoms in $m = 1$ and $m = -1$. Thereby the excited modes have characteristic momenta, which are visible in the plots as regular patterns with a certain wavelength. As we will see in the occupation spectra the corresponding momenta agree very well with the momenta of the of most unstable mode in Bogoliubov theory Eq. (4.17). One can see that the modes are spin excitations. The same pattern as in the density appears in F_x and F_y. Shortly afterwards it is also visible in F_z. There is also an additional length scale in F_z: one can observe large region of roughly 50 µm where F_z has a preferred direction. This phenomenon is not included in Bogoliubov theory and needs further study.

At later times the system gets more chaotic. In the density plots lines are visible, at which the density of one component drops down. That indicates

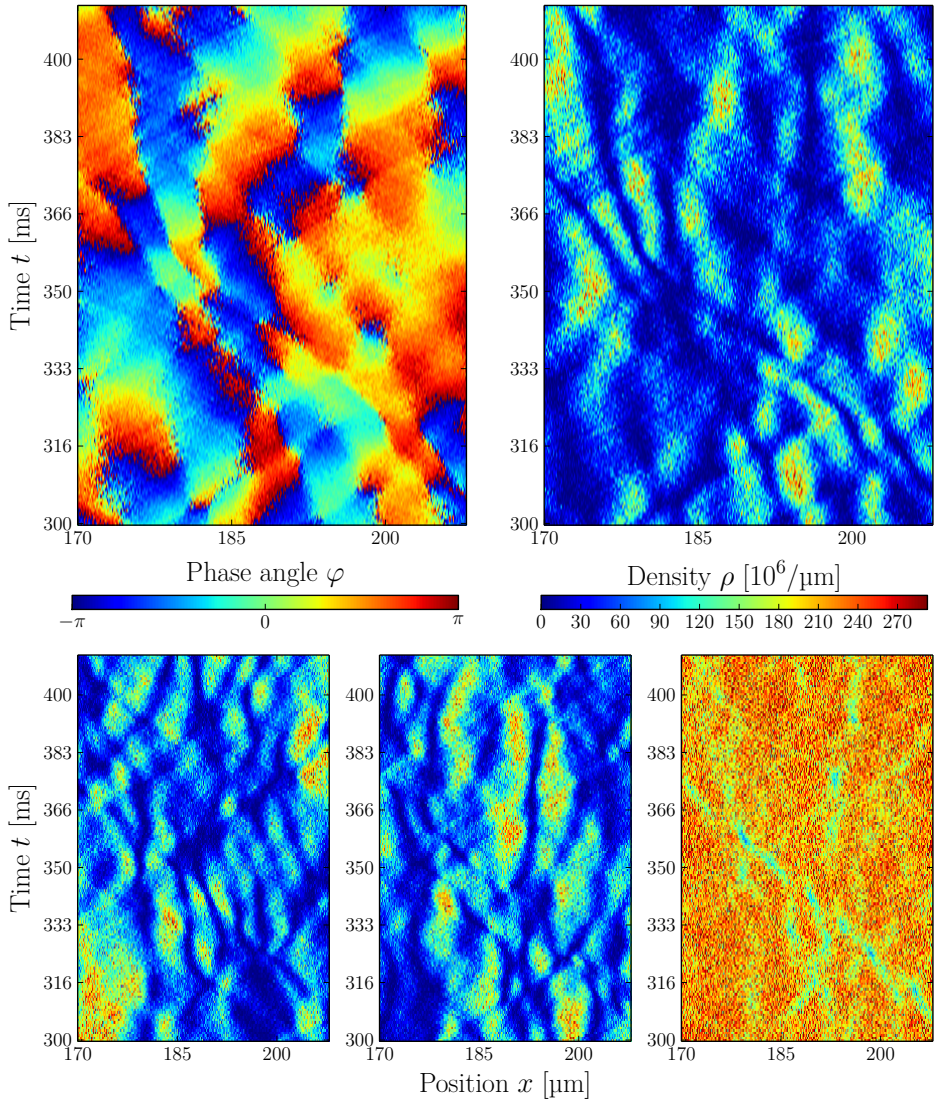

Figure 5.2: Scaled up region of Figure 5.1. Both plots in the top row show the $m = 0$ component. On the left side the phase is plotted and on the right side we see the density. In the phase plot we subtracted $1.1 \cdot c_0\rho$ to remove temporal oscillations. After the system gets more irregular, solitonic excitations can be seen. The density drops down and the phase of the wave function jumps. In the bottom row the density of the side components $m = 1$ (left) and $m = -1$ (middle) and the total density (right) are plotted for comparison.

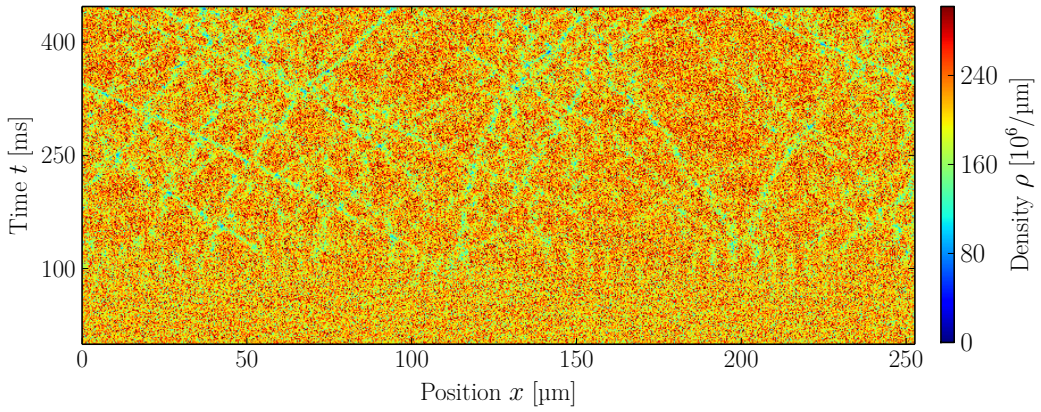

Figure 5.3: Total density in position space for the same realization as in Figure 5.1. After ≈ 100 ms lines appear along which the density drops down. The positions of the density dips move in time. This indicates the formation of gray solitons with finite velocity.

the formation of solitons. They are one dimensional solutions of the wave functions [57, 58]. For simplicity we give the solution for a one component condensate:

$$\psi(x,t) = \sqrt{\rho}\left[i\frac{v_\mathrm{s}}{c_\mathrm{s}} + \sqrt{1-\frac{v_\mathrm{s}^2}{c_\mathrm{s}^2}}\tanh\left(\sqrt{1-\frac{v_\mathrm{s}^2}{c_\mathrm{s}^2}}\frac{x-(x_0+v_\mathrm{s}t)}{\sqrt{2}\zeta}\right)\right]e^{i\mu t}\,, \quad (5.4)$$

where μ is the chemical potential $c_\mathrm{s} = \sqrt{ng/M}$ the speed of sound and v_s the speed of the soliton. The solutions for the spin-1 system are more complicated, because the density drop down in one component can be countered by a higher density in another component. Solutions of the wave function in one dimension are discussed in [59] for the case without an external magnetic field and in [60] with an external field. Solitons are quasi-topological defects, which are characterised by a phase jump of the wave function and a drop down of the density. For the time independent solution $v_\mathrm{s} = 0$ the phase changes by π and the density drops to zero. These are called black solitons. Solitons which show only weaker phase jumps and density dips, are called gray. Figure 5.2 shows a scaled up region of Figure 5.1, in which the phase and the density of the $m = 0$ is plotted. For comparison also the density of the side components and the total density are shown. The structures in the density look similar in all three hyperfine states. In the plots of $m = 0$ one can see that the density dips, which have a size of 1 – 2 µm, are accompanied by lines in the phase plot, along which the phase jumps in spacial direction. Most solitons are moving $v_\mathrm{s} \neq 0$ indicating the formation of gray solitons. The whole system looks very chaotic. It is not easy to identify a single soliton. In the phase plot the lines of phase jumps cross very often what indicates interactions of the solitonic excitations.

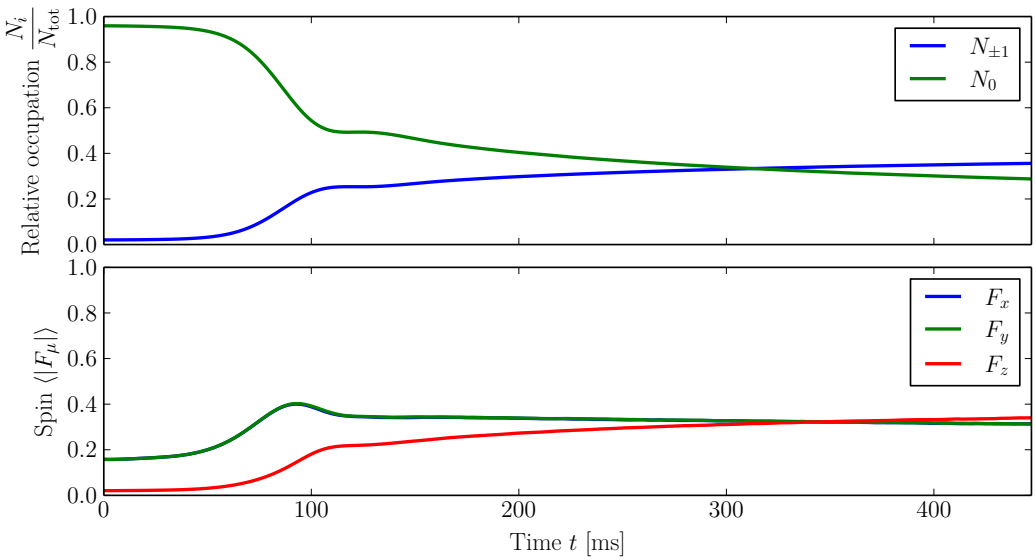

Figure 5.4: Time evolution of the relative occupation number of all magnetic sublevel (top) and of the spatially averaged, normalized spins (bottom) for the unseeded case. Parameters are the same as in Figure 5.1. The values are averaged over 1000 runs. The number of particles in the side modes is always identical. F_x and F_y are degenerated and in the bottom plot the blue and green line coincide. Initially all particles start in $m = 0$ with a small seed in the side components. In the beginning the number of particles in the side components grows exponentially. This is accompanied by the creation of a spin in x- and y-direction. Shortly afterwards also F_z starts to grow. After ≈ 120 ms the occupation numbers and the spins change only slowly.

In Figure 5.3 the total density of the whole simulation is shown and also in the total density solitonlike excitations can be seen. Here it is easier to follow the time evolution of a single topological defect. One can observe lines along which the density drops down. The mean density along these lines is not constant, but varies in time. There are no excitations during the very early stage of the time evolution. During this time, which is not shown in the phase plot, the phase is spatial very homogeneous and there are no phase jumps. The first jumps start to appear at $t \approx 130 - 150$ ms.

In Figure 5.4 the time evolution of the total occupation number of the three components and of the normalized spin is plotted. In the beginning all particles start in the $m = 0$ magnetic sublevel. The side modes have a small occupation through the quantum noise. This induces also a small initial spin in x- and y-direction. At early times the occupation number of the side modes grows exponentially. This is accompanied by a similar growth of F_x and F_y as it is predicted from Bogoliubov theory. Also a spin in z-direction is created with a delay of roughly $20 - 30$ ms. This is only possible in spatial extended traps

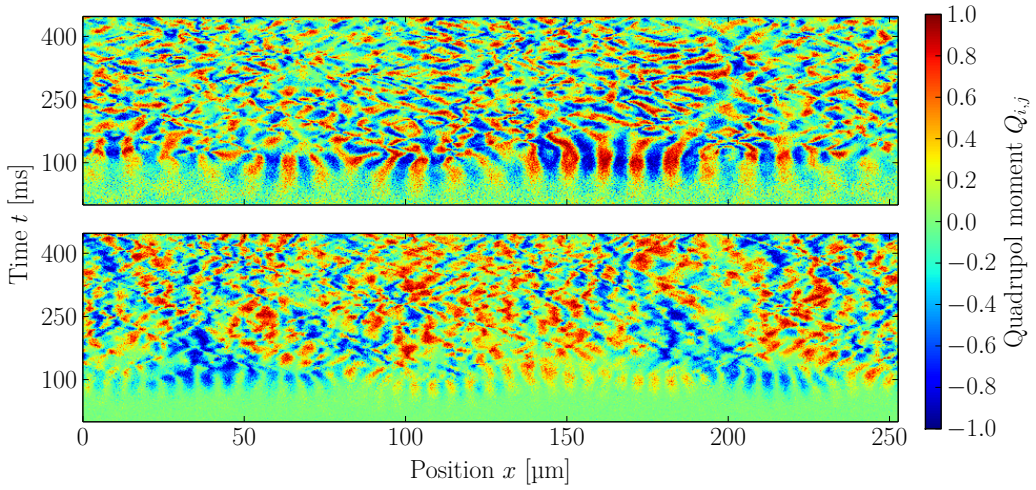

Figure 5.5: Quadrupole moments in position space for the same realization as in Figure 5.1. The plot of the quadrupole moment $Q_{x,z}$ (top) looks very similar to the plots of F_x and F_y. At early times one can observe pattern formation with a wavelength given by Bogoliubov theory. At later times the structures are smaller and less regular. The plot of $Q_{x,y}$ (bottom) shows new phenomena. Besides the length scale given by Bogoliubov, there is a second, much larger scale. It has a similar size as the scale in F_z, but the regions are stable for longer times and the total quadrupole moment is not conserved.

and cannot be seen in point like experiments. The exponential growth stops at $t \approx 100 - 120$ ms and all quantities change only very slowly.

Lastly we take a look at the quadrupole moments Eq. (5.3) in real space. The diagonal elements $Q_{i,i}$ are proportional to the square of the spin and give no new information. Because F_x and F_y are degenerated, it is sufficient to look at $Q_{x,z}$ and $Q_{x,y}$. They are plotted in Figure 5.5. The excitations of $Q_{x,z}$ are similar to those of F_x and F_y. At early times a pattern with a wavelength given by Bogoliubov theory emerges. Later the system gets more chaotic and the scales become smaller. This is different for $Q_{x,y}$, which shows similarities to F_z. In addition to the Bogoliubov length scale, a new, larger scale is visible, but the regions are longer stable than in F_z. One can also see that $Q_{x,y}$ is not a conserved quantity. For the shown realization, regions with positive values dominate.

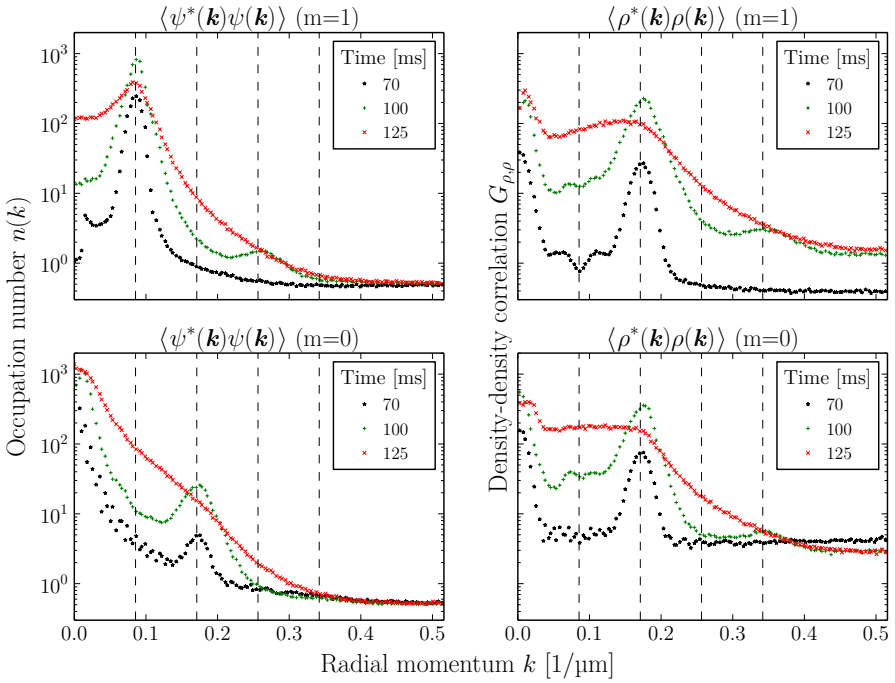

Figure 5.6: Occupation number $n^{(m)}(k)$ and density-density correlations $G^{(m)}_{\rho,\rho}(k)$ for the components $m = 0$ and $m = 1$ for three different times. The same parameters as in Figure 5.1 are used. The quantities are averaged over 1000 runs. For orientation the position of the most unstable Bogoliubov mode $k_{\text{m.u.}} = 0.085\ \mu\text{m}^{-1}$ and multiples of it are marked as dashed lines. 70 ms after the quench there is a peak around $k_{\text{m.u.}}$ in $n^{(1)}(k)$. At later times peaks at $2k_{\text{m.u.}}$ in $n^{(0)}(k)$ and at $3k_{\text{m.u.}}$ in the side modes appear. $G^{(m)}_{\rho,\rho}(k)$ looks very similar for all components: in the beginning peaks at $2k_{m.u}$ and $k = 0$ appear. At later times there is an additional, smaller peak at $4k_{\text{m.u.}}$. At late times the peaks vanish and the spectra fall off exponentially.

5.2 Spectra and Density-Density Correlations

In this section, we look at the spectrum $n^{(m)}(k)$ of the three components, of the spins and of the quadrupole moments. We also examine the density-density correlations $G^{(m)}_{\rho,\rho}(k)$. In the following k is always given in the convention $k = 1/\lambda$, which is also used in the experimental data. To compare the following results with the theoretic predictions, one has to keep in mind that in previous chapters the convention $k = 2\pi/\lambda$ is used. Figure 5.6 shows $n^{(m)}(k)$ and $G^{(m)}_{\rho,\rho}(k)$ for $m = 0$ and $m = 1$. We plot only one of the side components because the other one looks almost identical and gives no new information. The first visible excitation appears in the side component as a peak at a momentum which

agrees very well with the most unstable Bogoliubov mode $k_{\text{m.u.}} = 0.085\ \mu\text{m}^{-1}$ Eq. (4.17). The excited momentum region coincides with the predicted unstable region from Bogoliubov theory Eq. (4.20): $[0.061\ \mu\text{m}^{-1}, 0.104\ \mu\text{m}^{-1}]$.

At later times secondary modes get excited, which are created by Bogoliubov modes interacting with each other or with the remaining condensate. To make the description and analysis more simple we denote in the following momenta around the most unstable Bogoliubov mode $k_{\text{m.u.}}$ with k'. These excitations can be best observed in the spectra if $-q > 2nc_1$. In this case, the excited Bogoliubov modes have all momenta $k > 0$ and are clearly visible as isolated peaks. The first non-Bogoliubov excitation appears in $m = 0$ with momenta around $2k'$. Shortly after this a mode with $3k'$ in the side modes gets excited. In the $m = 0$ spectrum there is an additional peak at $k = 0$. It can be explained by the occupation of the stable Bogoliubov modes in $m = 0$ Eq. (4.15). Interestingly this peak has some finite value at $t \approx 100$ ms. This is confirmed by simulations with a large volume of $L = 4040\ \mu\text{m}$ and hence a better resolution in this momentum region. Its position is at $k \approx 0.015\ \mu\text{m}$. The reason for the finite value needs further study. In contrast to $n^{(m)}(k)$ the density-density correlations $G^{(m)}_{\rho,\rho}(k)$ look very similar for all components. In the beginning peaks at $k = 0$ and $2k'$ appear. Later an additional peak at $4k'$ starts to grow. The reason that they look almost identical is the high value of c_0. This keeps the density of the whole condensate very flat. Hence every density pattern in one component needs a counter part in the other components. This gives a qualitative explanation for the creation of the secondary mode at $2k'$.

In the beginning the Bogoliubov modes with momentum k' are excited. If we assume that only this mode is occupied in the side modes, the wave functions can be written as: $\psi_{\pm1}(x) = A\cos(k'x) + iB\cos(k'x + \phi)$. The density is given by the square of the wave function

$$\begin{aligned}\hat{\rho}_{\pm1}(x) =& \hat{\psi}^\dagger(x)\hat{\psi}(x) \\ =& \frac{A^2}{2}\left(\cos\left(2k'x\right) + 1\right) \\ &+ \frac{B^2}{2}\left(\cos\left(2k'x + 2\phi\right) + 1\right) . \end{aligned} \tag{5.5}$$

Here we can see two important changes from the wave function to the density: First, each mode in the wave function gives a constant contribution to the density $(A^2 + B^2)/2$. The reason is that the density can only be positive, while the wave function is complex. Every particle increases the mean value of the density function. In Fourier space this value is described by the $k = 0$ mode. Hence every particle gives a contribution to this mode and the number of total

particles is proportional to the square of $G_{\rho,\rho}(k=0)$. The second difference is that there is no peak at k' in the density-density correlation, but at $2k'$. The reason is that we square a function, which oscillates around zero. This results in a function oscillating with the double frequency around half of the square of the initial amplitude. This explains why $G^{(1)}_{\rho,\rho}(k)$ has a peak at $2k'$ and not at k' like $n^{(1)}(k)$.

The patterns which are created in both side components are in the beginning spatial identical, but the system prefers a flat density because the spin-independent coupling constant c_0 is large. Hence, there has to be also pattern formation in the $m=0$ component. The wave function of $m=0$ differs from the other ones in the condensate mode $k=0$. If a counter mode k_c is excited the wave function is given by $\psi_0(x) = A_0 + A'\cos(k_\mathrm{c}x) + iB'\cos(2k_\mathrm{c}x+\phi)$ with $B', A' \ll A_0$ and the dominant parts of the density are

$$\hat{\rho}_0(x) \approx A_0^2 + 2A_0A'\cos(k_\mathrm{c}x)\,. \tag{5.6}$$

To have patterns with the same wavelength in all three components, we need $k_\mathrm{c} = 2k'$. That coincides with the results of our simulations. The important result of this derivation is that the excitation of two different modes k' and $2k'$ in $n^{(m)}(k)$ can look very similar in $G^{(m)}_{\rho,\rho}(k)$. The occupation of the condensate mode in the wave function has a huge influence on the density in Fourier space. There is also a more mathematical derivation for the excitation of the $2k'$ mode in the next section (Eq. (5.8)).

We now take a closer look at $G^{(m)}_{\rho,\rho}(k)$. In the beginning the height differs between $G^{(0)}_{\rho,\rho}(k)$ and $G^{(1)}_{\rho,\rho}(k)$. At the calculation of $G^{(m)}_{\rho,\rho}(k)$ each mode in the wave function is multiplied with each other mode. Hence the height of all Fourier modes depends on the total occupation of the component. In the side modes the height of the unoccupied modes is very low in the beginning and increases over time. As discussed above, the first excitation in each mode creates a peak at $2k'$ in $G^{(m)}_{\rho,\rho}(k)$. But there is an additional peak around zero. It comes from the fact that the multiplication of two modes k_1 and k_2 gives not only a contribution to the sum of both modes k_1+k_2, as in Eq. (5.5), but also to their difference k_1-k_2 (see Appendix A.1). Hence the peak around $k=0$ comes from the finite width of the peaks in wave function. There is also a small peak at $4k'$ in all components. In $G^{(0)}_{\rho,\rho}(k)$ this peak comes from the mode at $2k'$ in $n^{(0)}(k)$ and in $G^{(1)}_{\rho,\rho}(k)$ the two peaks at k' and $3k'$ in the wave function can give a contribution to $k'+3k'$.

In Figure 5.7 the spectra of the F_y, F_z and of the quadrupole moments $Q_{x,y}$ and $Q_{x,z}$ are plotted. The spectrum of F_x is similar to the spectrum of F_y and gives no additional information. The Bogoliubov excitations are spin excitations and the same peaks as in $n^{(1)}(k)$ can also be seen in F_x and F_y.

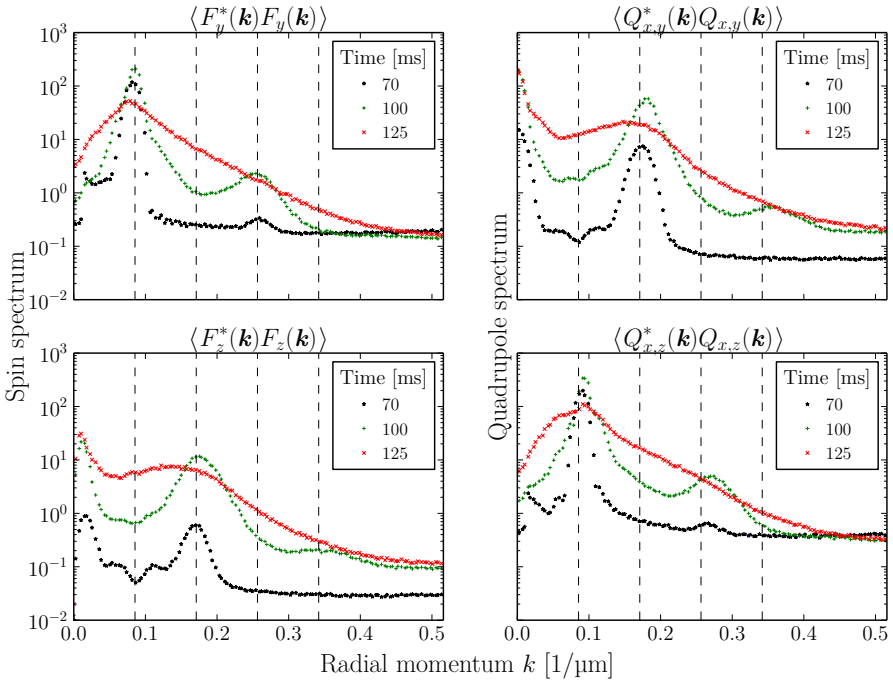

Figure 5.7: Spin and quadrupole spectra for the same runs as in Figure 5.6. The spectra of F_y (upper left), F_z (lower left), $Q_{x,y}$ (upper right) and $Q_{x,z}$ (lower right) are shown. For orientation the position of the most unstable Bogoliubov mode $k_{\text{m.u.}} = 0.085$ µm^{-1} and multiples of it are marked as dashed lines. The spectra of F_y and $Q_{x,z}$ look almost identical. They show the same peaks as the spectra of the $m = 1$ component, but they are more pronounced. The spectrum of F_z has a peak at $2k_{\text{m.u.}}$ and a small peak at $4k_{\text{m.u.}}$. At early times there is also a small peak at $k \approx 0.015$ µm^{-1} visible. Also the spectrum of $Q_{x,y}$ has peaks at $2k_{\text{m.u.}}$ and $4k_{\text{m.u.}}$. An additional peak at $k = 0$ becomes very large at later times.

The peaks are even slightly more pronounced. The spectrum of $Q_{x,z}$ looks almost identical to that of F_x and gives also no new information. The spectrum of F_z has peaks at $2k'$, $4k'$ and at $k \approx 0.015$ µm. The position of the last peak is confirmed by simulations with $L = 4040$ µm, which have a better resolution, and coincides with the peak which is shortly visible in $n^{(0)}(k)$. It corresponds to the large scale pattern observed in Figure 5.1. In the spectrum of $Q_{x,z}$ peaks at $2k'$, $4k'$ and a large peak at $k = 0$ are visible. The last peak keeps growing at later times. It corresponds to the large regions in $Q_{x,z}$, which are stable for long times.

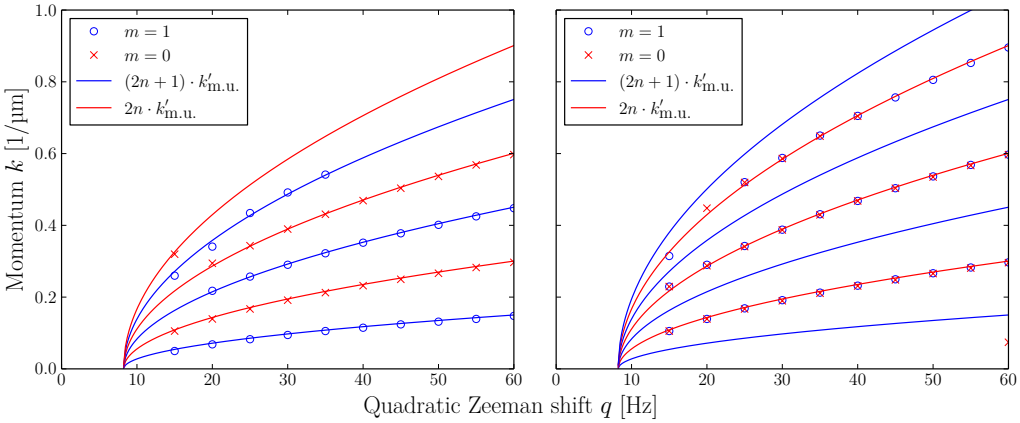

Figure 5.8: Position of the peaks of $n^{(m)}(k)$ (left) and $G^{(m)}_{\rho,\rho}(k)$ (right) for different values of the quadratic Zeeman effect q at $t \approx 190$ ms. The parameters are: $N_s = 16384$, $L = 754.9$ µm, couplings are given in Tab. 3.1 and the density is increased to $R = 50000$ as described in Sec. 3.3. The spectra are averaged over 200 runs before the peaks are detected. For orientation the position of the most unstable Bogoliubov mode Eq. (4.17) and multiples of it are plotted (even multiples: red solid lines, odd multiples: blue solid lines). The peaks in $n^{(1)}(k)$ (blue) are near odd multiplies and the peaks in $n^{(0)}(k)$ (red) are near even multiplies of the most unstable mode. $G^{(m)}_{\rho,\rho}(k)$ shows in all components peaks only at even multiplies of the most unstable Bogoliubov momentum.

5.3 Analysis of secondary excitations

In this section, we take a closer look at the secondary excitations. Their exact position and their growth rates are examined. We find that the latter depends on the density in the system. We compare simulations with different values of R Eq. (3.18). We can find explanations for the positions of the peaks and in the limit of large R also for the growth rates.

At first we study the position of the peaks. Therefore we use high densities. In this case, the occupation numbers of the peaks are higher and the quantum fluctuations have a smaller influence on the dynamics. The number of excitations increases. Their position for different values of q and $R = 50000$ are shown in Figure 5.8. For $k' > 0$ they always show the same pattern. All peaks in $n^{(1)}(k)$ are at odd multiples of k' and all peaks in $n^{(0)}(k)$, $G^0_{\rho,\rho}(k)$ and $G^1_{\rho,\rho}(k)$ are at even multiples of k'. The number of excitations is largest for values around $q = 30$ Hz. If q is small, we are in the regime, where the region of unstable modes also includes $k = 0$. Hence the peaks are smeared out. The algorithm finds no peaks for $q = 10$ Hz and misses some peaks at $q = 15$ Hz.

Interestingly, the highest peak in $G^{(m)}_{\rho,\rho}(k)$ is identical with the highest peak in

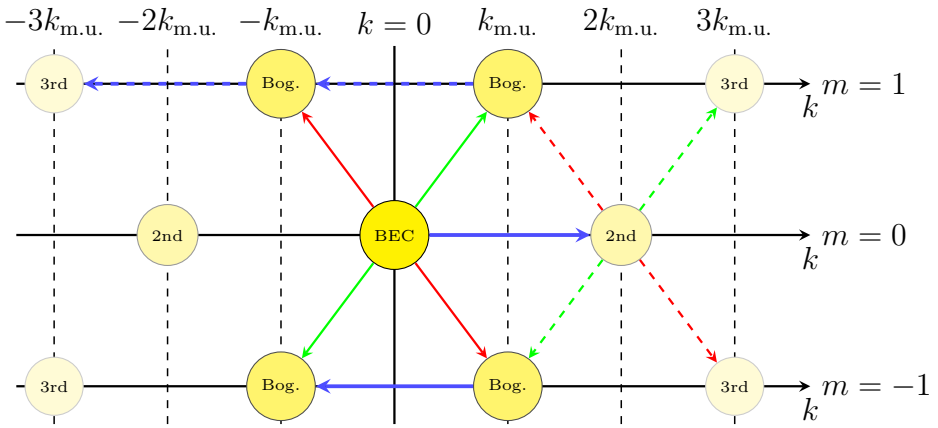

Figure 5.9: Momentum conservation of Bogoliubov and secondary excitations. In early time evolution Bogoliubov modes with momentum $k_{\text{m.u}}$ are excited (solid green and red arrows). The Bogoliubov modes can interact with the condensate and create new modes with momenta $2k_{\text{m.u}}$ in the $m = 0$ mode (one possible interaction in solid blue). There are a number of different ways to excite even higher modes (examples: dashed red, blue and green arrows).

$n^{(0)}(k)$ and there are no peaks at larger momenta. This can also be seen in Figure 5.6: Although there is a peak at $3k'$ in $n^{(1)}(k)$, there is no peak at $6k'$ in $G^{(1)}_{\rho,\rho}(k)$. The reason for this is that the wave function is a complex quantity. Therefore the phase plays an important role and can lead to cancellation of certain terms in $G^{(m)}_{\rho,\rho}(k)$. This can already be seen in Eq. (5.5). For $\phi = \pi/2$ and $A^2 = B^2$ the two cosine terms cancel each other and only the constant term remains. This is also shown for a more general case in the Appendix A.1.

We take now a closer look at the excitations of the higher modes and consider momentum conservation. Some possible processes, that show the creation of the k', $2k'$ and $3k'$ mode, are shown in Figure 5.9. In the beginning the Bogoliubov modes are excited. If $q > nc_1$ the particles get energy and transform it into kinetic energy Eq. (4.18). Particles with momenta k' and $-k'$ are created. One possible explanation for the excitation of the $2k'$ mode could be that two particles each with momenta k', one from $m = -1$ and one from $m = 1$, interact and create two particles in $m = 0$ with momenta, one with $k = 0$ and one with $2k'$. But this process is energetically strongly suppressed, because each particle loses the energy q in this process. Hence the main contribution comes from a second possible process: One particle of one of the side components with momentum k' interacts with one of the remaining particles in the condensate ($m = 0$ and $k = 0$). Thereby the particle from the side component changes its momentum to $-k'$ and the particle in $m = 0$ to $2k'$. In the Hamiltonian both interaction terms (the c_0 and the c_1 term)

include this process:

$$H = c_0 \hat{a}^\dagger_{\mathbf{2k'},0} \hat{a}^\dagger_{\mathbf{-k'},\pm1} \hat{a}_{\mathbf{0},0} \hat{a}_{\mathbf{k'},\pm1} + c_1 \hat{a}^\dagger_{\mathbf{2k'},0} \hat{a}^\dagger_{\mathbf{-k'},\pm1} \hat{a}_{0,0} \hat{a}_{\mathbf{k'},\pm1} + \cdots . \tag{5.7}$$

That this term is also included in the c_1 part can be seen in the explicit expression Eq. (2.11). In ^{87}Rb the main contribution comes from the c_0 term, because $c_0 \approx 30 c_1$. The $2k'$ mode can grow even faster than the primary mode. We can see this using a simple approximation. If we neglect the c_1 term and assume that only the condensate mode and the most unstable mode k' is occupied, the time evolution of the secondary mode is given by

$$i\dot{\psi}_{2k',0} = \left[\omega_{2k'} + c_0(4n^{(\mathrm{s})}(k') + n^{(0)}(0))\right] \psi_{2k',0} + 2c_0 \psi_{-k',\mathrm{s}} \psi^*_{k',\mathrm{s}} \psi_{0,0} \,, \tag{5.8}$$

with $\omega_{2k'} = \epsilon_{2k'} + mq$, s stands for the two side modes $m = \pm 1$ and we assume that the occupation of these modes is the same. The first term gives just a phase rotation. Only the last term contributes to the growth of the mode. We know from Bogoliubov theory that $n^{(s)}(k')$ grows exponentially:

$$\psi_{k',\mathrm{s}} = \sqrt{n^{(\mathrm{s})}(k', t=0)} e^{(|\omega_f| - i\omega_{k'})t} \,, \tag{5.9}$$

where ω_f is the eigenenergy of the Bogoliubov mode Eq. (4.16). The condensate mode is macroscopically occupied and stays during early stages of the time evolution approximately constant: $\psi_{0,0}(t=0) = \sqrt{\rho_0}$, where ρ_0 is the density of the condensate at $t = 0$. Then the time evolution of the secondary mode $\psi_{2k'}(t) \approx \eta(t) \exp\left(i(\omega_{2k'} + c_0 n)t\right)$, with $n = 4n^{(\mathrm{s})}(k') + n^{(0)}(0)$, is given by

$$\dot{\eta}(t) = -i2c_0\sqrt{\rho_0} n^{(\mathrm{s})}(k', t=0) e^{2|\omega_{f_\mu}|t} e^{-i\delta\omega t} \,, \tag{5.10}$$

$$\eta(t) = \frac{2c_0\sqrt{\rho_0} n^{(\mathrm{s})}(k', t=0)}{\delta\omega + i2|\omega_{f_\mu}|} (e^{(2|\omega_{f_\mu}| - i\delta\omega)t} - 1) + \eta(0) \,, \tag{5.11}$$

where $\delta\omega = -\omega_{-k} + \omega_k + \omega_{2k} - \omega_0 = \omega_{2k}$. The occupation number is given by $|\eta(t)|^2$. After a time $t \approx (2\omega_f)^{-1} \approx 10$ ms the -1 can be neglected and the first term grows exponentially $\eta(t) \sim \exp(2|\omega_f|t)$ with twice the rate of the primary mode.

In Figure 5.10 the time evolution of the occupation numbers at the positions of the peaks is plotted. Since the evolution depends on the density, we compare two cases: In the left plot the density of the experiment is used with $R \approx 15$ and in the right one we use $R = 500000$. Bogoliubov theory predicts a growth rate of $\tau^{-1}_{\mathrm{Bog}} = 0.103\ \mathrm{ms}^{-1}$ Eq. (4.22) for the first peak and we expect twice this rate for the second peak. We see that this agrees very well with the results of the high density case. If we use the density of the experiment, the growth rates are smaller. Because of the low density, quantum noise plays an important role.

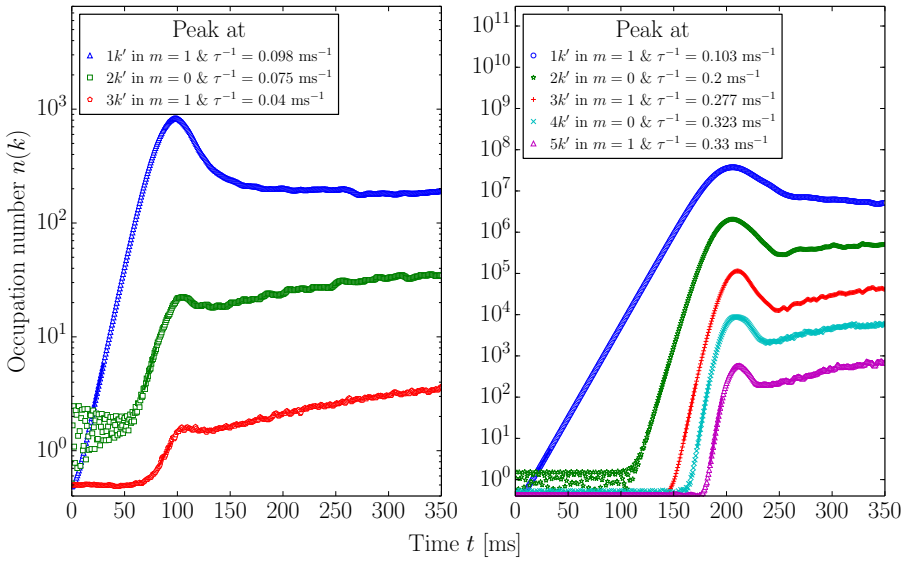

Figure 5.10: Time evolution of the occupation numbers of the peaks at k' and multiples thereof. A fit to the exponential growth is added. Note the different scales on the y-axis. On the left side values averaged over 1000 runs with the parameters given in Figure 5.1 ($R \approx 15$) are plotted. The parameters for the right plot are the same except for: $R = 500000$ as described in Sec. 3.3, $L = 754.9$ µm and $N_s = 16384$. Here 200 runs are averaged. In the right plot one can see an exponential growth of all modes. The Bogoliubov mode grows from the beginning. The next mode starts at $t \approx 100$ ms and grows roughly with the double rate. The larger the momenta of a mode, the later and faster it grows. In the left plot only the first two modes show exponential growth. At early times noise dominates the time evolution of the Bogoliubov mode. The second mode starts to grow earlier than in the case of high densities, but with a smaller rate.

To simulate the quantum noise, each mode is initially occupied. The ratio of their occupation in comparison with the occupation of the condensate mode is larger in the low density case. Hence, the relative importancy of all terms in the Hamiltonian, which do not include the condensate mode, increases. The approximation we used in Eq. (5.8) to predict the growth rate of the second peak is not valid anymore. The system shows even small derivations from Bogoliubov theory. The growth rate of the first peak $\tau^{-1} = 0.098$ ms^{-1} is slightly smaller than in the high density case. For $R = 500000$ the time evolution of higher excitation shows some interesting phenomena. The higher the momenta of the mode the faster the mode grows. They also start to grow later. The maximum value of all excitations decreases exponentially with k and all modes reach their maximum almost at the same time.

The growth rates of the excitations in the spectra of the components and the

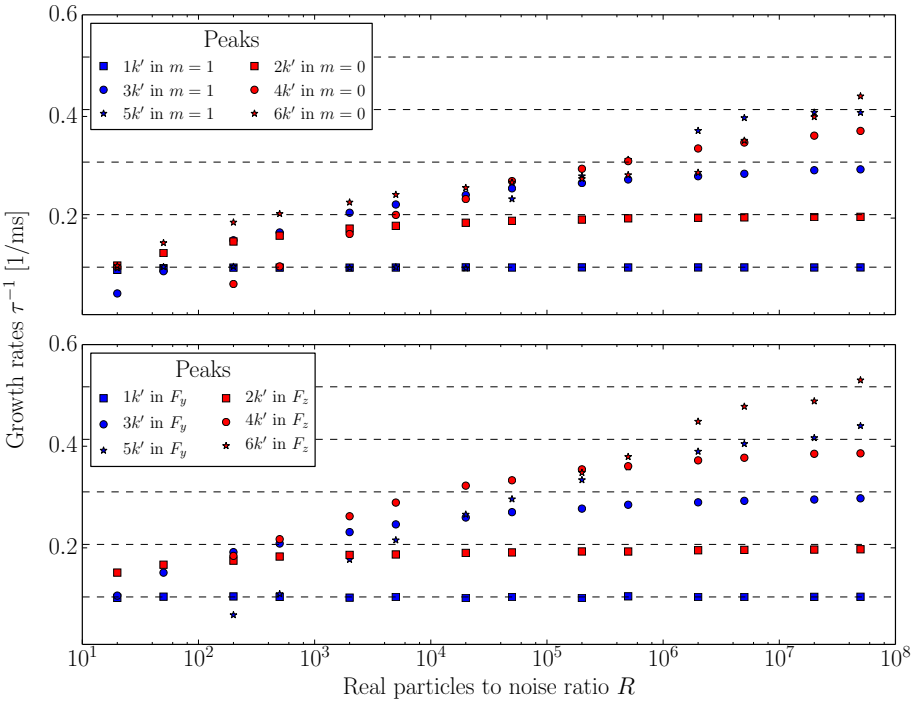

Figure 5.11: Exponential growth rates τ^{-1} of the peaks in the spectra of the components (top) and the spin (bottom) for different R. The remaining parameters are: $N_s = 16384$, $L = 754.9$ µm, $q = -25$ Hz $= -3.04 \cdot nc_1$, couplings are given in Tab. 3.1. For orientation the expected growth rate from Bogoliubov theory τ_{Bog}^{-1} Eq. (4.22) and multiples thereof are plotted (dashed black lines). The growth rates increase for larger R until they approach their final value, which is always a multiple of τ_{Bog}^{-1}. Peaks at high momenta appear only at high values of R. The growth rates of the peaks in the spin spectra reach their maximal growth rate already at lower R than the corresponding rates in the spectra of the components.

spins for different values of R are plotted in Figure 5.11. There are more excitations for large R. Their growth rates increase with R and approach a final value, which is always a multiple of the expected growth rate of Bogoliubov theory τ_{Bog}^{-1} Eq. (4.22). The approached rate of a peak at $n \cdot k'$ is always given by $n \cdot \tau_{\text{Bog}}^{-1}$ with $n \in \mathbb{N}$. This gives an indication for the dominant processes, which excite the modes. We have already given an explanation for the growth rate of the peak at $2k'$. The peak at $3k'$ has a growth rate of $3\tau_{\text{Bog}}^{-1}$. There are several possible processes, which predict this rate. One of them is, that two particles in the side components both with momentum k' interact without changing the hyperfine level and produce two particles with $-k'$ and $3k'$,

respectively:

$$i\dot{\psi}_{3k',\mathrm{s}} \sim c_0 \psi_{k',\mathrm{s}} \psi^*_{-k',\mathrm{s}} \psi_{k',\mathrm{s}} \,. \tag{5.12}$$

All three wave functions on the right hand side grow with $\tau_{\mathrm{Bog}}^{-1}/2$. Hence this process predicts the observed rate for the occupation number $n^{(s)}(3k') \sim \exp(3\tau_{\mathrm{Bog}}^{-1})$. It is shown in Figure 5.9 with blue dashed lines. Another process, in which two particles in $m = 0$ with $2k'$ undergo spin-changing collisions, would even predict a growth rate of $4\tau_{\mathrm{Bog}}^{-1}$. However, this process is proportional to c_1 and therefore sub-dominant.

For higher excitations the number of possible processes increases. Thereby the processes, in which the participating modes have the highest occupation numbers, are most important. We now try to find the growth rate for the excitation of a new peak at $n \cdot k'$ in component m. Without loss of generality we take $n > 0$. We focus on the dominant c_0 term. This means that the particle, which gets excited is initially also in component m. We assume that this particle comes from an arbitrary peak in m and has momentum $l \cdot k'$ with $l \in [-(n-2), -(n-4), \cdots, n-2]$. The second particle in component m' has to transfer the momenta $(n-l) \cdot k'$. All possible processes are given by

$$i\dot{\psi}_{n\cdot k',m} \sim c_0 \psi_{q\cdot k',m'} \psi^*_{(q+n-l)\cdot k',m'} \psi_{l\cdot k',m} \,. \tag{5.13}$$

The occupation numbers of peaks at low momenta are higher. Hence $|q|$ and $|q+n-l|$ have to be small. This means that q has to be negative $q \in [-(n-l), -(n-l)+2, \cdots 0]$. If we assume that all existing peaks with momenta $j \cdot k'$ grow with $j \cdot \tau_{\mathrm{Bog}}^{-1}$, the growth rate for the new peak is given by

$$\tau^{-1}(n \cdot k') = (|q| + |q+n-l| + l) \cdot \tau_{\mathrm{Bog}}^{-1} \,. \tag{5.14}$$

It gives $n \cdot \tau_{\mathrm{Bog}}^{-1}$ for $l \geq 0$ and $(n+2l) \cdot \tau_{\mathrm{Bog}}^{-1}$ for $l < 0$, but the latter case is suppressed. The same process with $l' = -l > 0$ is dominant, because $(n-l')$ is smaller and hence the occupation of the peaks in m' is larger. In conclusion, all processes, which describe the scattering of a particle with momenta $l \cdot k'$ to momenta $n \cdot k'$ predict either a growth rate of $n \cdot \tau_{\mathrm{Bog}}^{-1}$ or are suppressed.

5.4 Dynamics at late times

We take now a look at the late time evolution. At times $t > 200$ ms $n^{(m)}(k)$ and $G^{(m)}_{\rho,\rho}(k)$ are very similar for all hyperfine states and change only slowly in time. They are plotted for $m = 0$ and the parameters of the experiment at

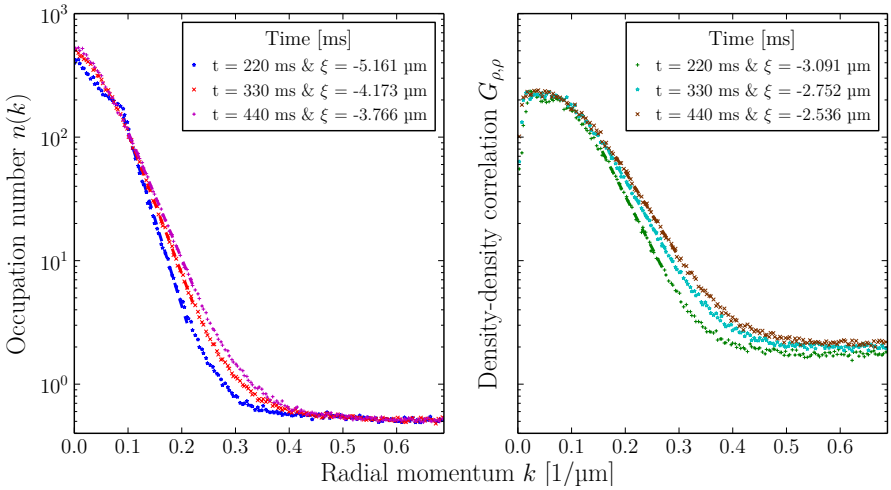

Figure 5.12: Occupation number $n(k)$ (left) and density-density correlations $G_{\rho,\rho}(k)$ (right) of the $m = 0$ component at late times. The parameters are: $\rho = 200 \cdot 10^6$ m^{-1}, $N_s = 8192$, $L = 252.2$ µm, $q = -25$ Hz $= -3.04 \cdot nc_1$, couplings are given in Tab. 3.1. The quantities are averaged over 1000 runs. At late times both $n(k)$ and $G_{\rho,\rho}(k)$ change only slowly. They fall off exponentially and the decay length is fitted. It decreases slowly in time.

three different times in Figure 5.12. The spectrum $n^{(0)}(k)$ falls of exponentially. This is expected at high k, if excitations, which are similar to solitons, are created. In the case of solitons the decay length $\xi_{n(k)}$ depends on their width. At $t = 220$ ms the decay length is $\xi_{n(k)} = 4.27$ µm. It decreases in time and at $t = 440$ ms we have $\xi_{n(k)} = 3.60$ µm. Also $G_{\rho,\rho}(k)$ falls of exponentially, but with a smaller constant. During the observed time it drops from $\xi_{G(k)} = 2.62$ µm at $t = 220$ ms to $\xi_{G(k)} = 2.35$ µm at $t = 440$ ms.

Figure 5.13 shows decay length $\xi_{n(k)}$ at different times. We compare different values of q for the parameters of the experiment and for $R = 50000$. The decay lengths take values between 2.5 µm and 6 µm and are slightly larger for the high density case. They depend strongly on the strength of the quench q and are smaller for high q. They seem to reach a final value at high q around $\xi_{n(k)} \approx 2.7$ µm for the low density and around $\xi_{n(k)} \approx 3.1$ µm for the high density. These values are similar to the spin healing length $\zeta_S = 2.66$ µm. One possible explanation for the q dependency is that the energy that is put into the system through the quench depends on q. For high q values the domains, which are formed during the time evolution, are smaller and their number is higher. This can have an influence on the spectra. It is also possible that the number of topological defects depend on q. As we saw in the position space plots in Figure 5.2, not all structures can be explained by solitons and

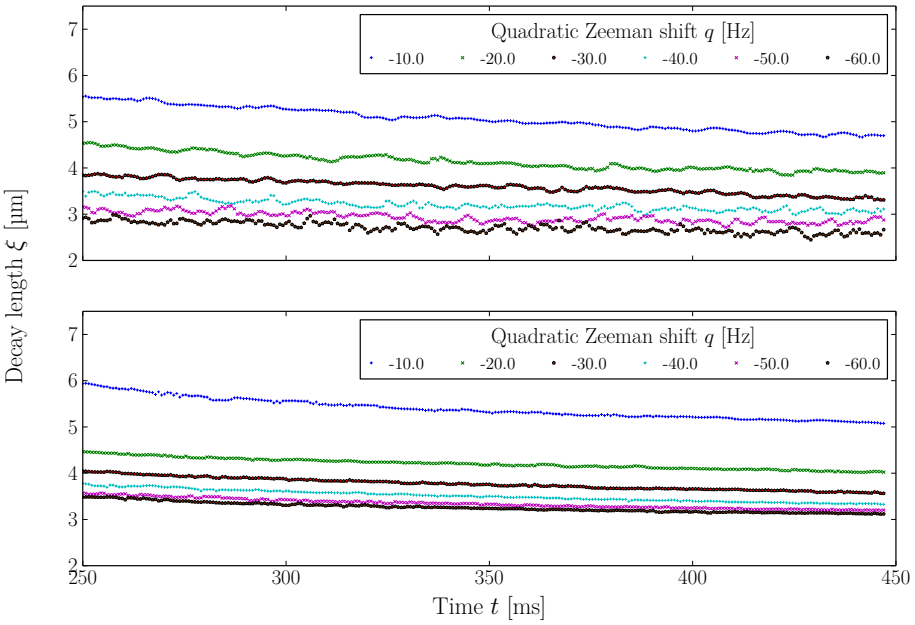

Figure 5.13: The decay length $\xi_{n(k)}$ at different times for the density of the experiment (top), where $R \approx 15$ and a higher density with $R = 50000$ (bottom). Quenches with different values of q are compared. For the high (low) density case the same parameters as in Figure 5.11 (Figure 5.1) are used. The decay length drops slowly to lower values over time. For high negative values of q the decay lengths are smaller. In the case of high density they are larger for the same values of q.

maybe the soliton model is not sufficient to explain the spectra. The strong q dependency of the spectra needs further study.

5.5 Density-Density Correlations in the Experiment

In this section, we compare the density-density correlations measured in the experiment [32] with numerical data. In the experiment two different magnetic fields are used: $B = 1.213$ G and $B = 2.03$ G. The effective value of q can be changed by the detuning δ (see Sec. 3.1). The high magnetic field in the second case increases the energy distance to the $m = \pm 2$ hyperfine states and should improve the three-component description. Here we compare numerical results with experiments, in which $B = 1.213$ G is used and the calculated values for q are $q = -30$ Hz, $q = -33$ Hz and $q = -36$ Hz. The $G^{(-1)}_{\rho,\rho}(k)$ function

for these cases are plotted in Figure 5.14. It turns out that we find a better agreement with the experimental results, if we use smaller q values in the simulation. In Figure 5.14 we use $q = -10$ Hz, $q = -15$ Hz and $q = -20$ Hz for comparison. For these values the behavior of $G^{(-1)}_{\rho,\rho}(k)$ is very similar in the simulation and in the experiment. For both cases one can observe the growth of a peak around $k = 0$ and a second peak at higher k. The position of the second peak increases with larger values of q. At later times the peaks vanish and $G^{(1)}_{\rho,\rho}(k)$ falls of exponentially with k. Also the timescales of experiment and simulation agree very well. The peaks start to grow almost at the same time, but the growth stops a little bit earlier in the experiment.

For the high q values, which we have calculated for the experimental setups, we would expect the peaks at higher momenta. One possible explanation is that the actual values of q are smaller in the experiment. Here one has to keep in mind that q is the difference of two large numbers of the order of 100 Hz (see Sec.3.1). Hence the uncertainty of q is much larger than the uncertainty for one of these numbers. However, there are also other possible reasons for the differences between the numerical and experimental results. There is a finite temperature in the experiment. This means that not all particles are in the condensate mode, but also low momentum modes are initially occupied. This can be an explanation for the smaller k value of the second peak. The Bogoliubov modes grow exponentially. If the modes with small k are initially higher occupied, they will grow faster and the peak is shifted to smaller k. Another important point can be the high uncertainty of the spin-dependent coupling c_1. We will see in Sec. 6.2 that other phenomena in the experiment show better agreement with theory for higher values of $c_1\rho$. On the one hand this would also shift the position of the most unstable mode. One can see in Eq. (4.17) that a higher value of $c_1\rho$ corresponds to a smaller position of the second peak. On the other hand a larger value of $c_1\rho$ would also predict a faster time evolution, which can not be seen in the experiment. Another difference is that the condensate is trapped in the experiment. Therefore the density is not homogeneous. The growth rate of the Bogoliubov modes depends on the density. In the experiment the density is smaller at the sides of the trap and hence the excitation of the modes is slower. That effect can be seen, if one studies the time evolution in position space. This may explain why the second peak is less pronounced in the experiment.

As in the simulation $G^{(0)}_{\rho,\rho}(k)$ looks very similar to $G^{(-1)}_{\rho,\rho}(k)$ in the experiment. A peak at the same position can be seen. This indicates the excitation of a secondary mode at $2k'$ in $m = 0$. This is not predicted by Bogoliubov theory and shows non-linear effects in the experiment.

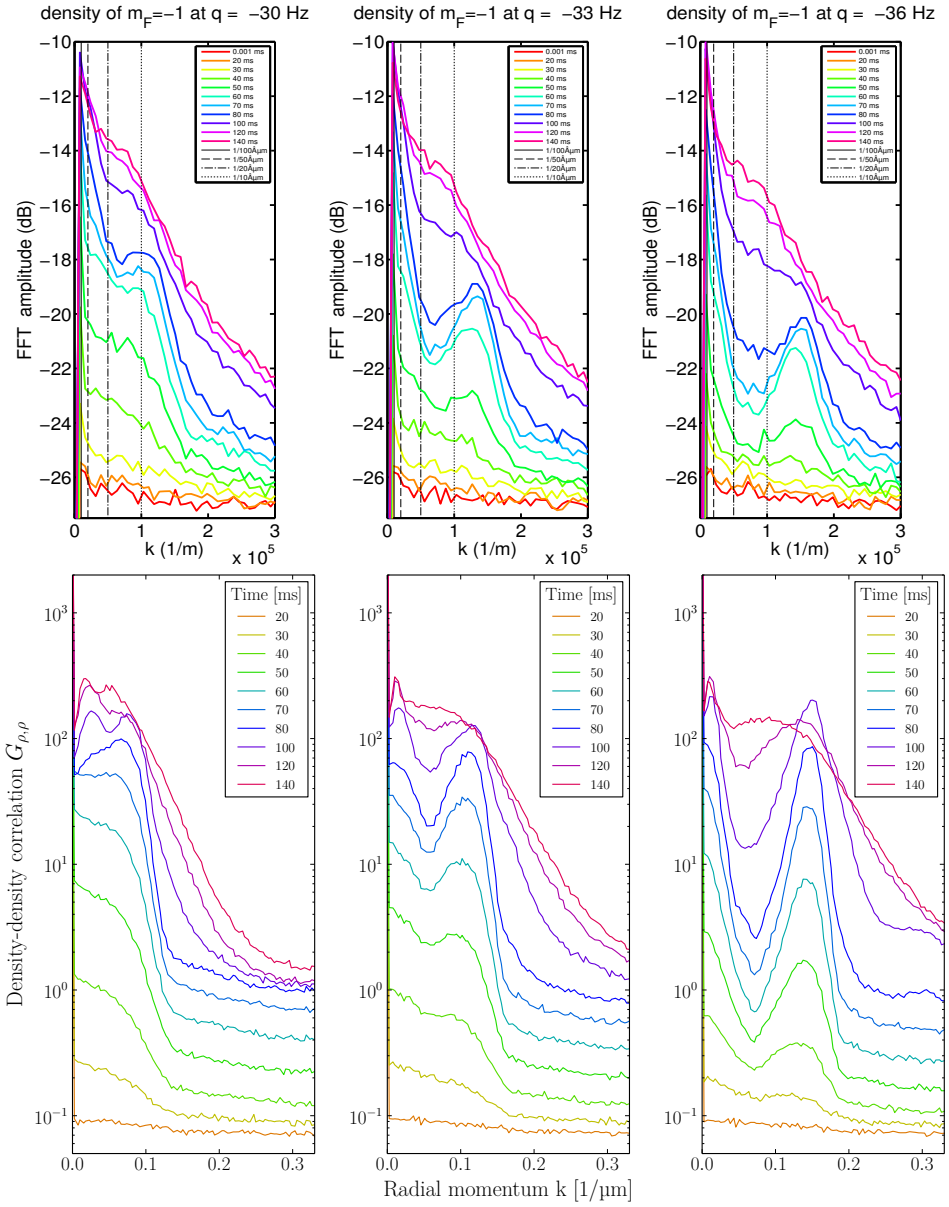

Figure 5.14: Experimental (top) and numerical results (bottom) for $G_{\rho,\rho}(k)$ in $m = -1$ in comparison. The experimental results are from [32] and the $k = 0$ value is set to zero. The Zeeman shifts calculated for the experiments are $q = -30$ Hz (left), $q = -33$ Hz (middle) and $q = -36$ Hz (right). The results agree better, if smaller values are used in the simulations. Here we show the results for $q = -10$ Hz (left), $q = -15$ Hz (middle) and $q = -20$ Hz (right). The numerical results are averaged over 1000 runs. The parameters are: $\rho = 200 \cdot 10^6$ m^{-1}, $N_s = 8192$, $L = 252.2$ µm, couplings are given in Tab. 3.1. In both cases a peak around $k = 0$ and a second peak at finite k starts to grow at $t \approx 40$ ms. The position of the peak in the simulation is roughly at twice the momentum of the most unstable Bogoliubov mode k' Eq. (4.17). For the shifted q value the position of the peaks agree very well. The peaks are most pronounced at 80 ms (experiment) and 100 ms (numeric), respectively.

6

Seeded Initial Conditions

In this chapter, we study the seeded initial conditions. Most particles start again in the $m = 0$ component but a small part of the particles are initially transferred to the side modes. We will call this transferred particles *seed*. The idea behind this preparation is to compare the effects of a real particles with the case in which initially only quantum noise is present in the side modes. To compare our results with experiment we need to know the exact preparation of the initial state. Initially all particles are again prepared in $m = 0$. After this a radio-frequency-pulse (RF-pulse) is used to transfer particles in the side modes. In spin space the pulse acts as a rotation around the x-axis and can be described by the f_x matrix

$$\hat{\psi}(t=0) \sim e^{i\theta f_x} \begin{pmatrix} 0 \\ 1 \\ 0 \end{pmatrix} , \tag{6.1}$$

where θ is the rotation angle. To calculate the state after the rotation one can use that $f_x^3 = f_x$ and $f_x^4 = f_x^2$. This simplifies the exponential to $\exp(i\theta f_x) = f_x^2 \cos\theta + i f_x \sin\theta$. Subsequently the system is again driven out of equilibrium by an external magnetic field to negative q values and the new ground state is in the paramagnetic phase

$$\hat{\psi}_{\text{unseeded}} \sim \begin{pmatrix} 0 \\ 1 \\ 0 \end{pmatrix} \xrightarrow{\text{RF-pulse}} \hat{\psi}_{\text{seeded}} \sim \begin{pmatrix} i\frac{\sin\theta}{\sqrt{2}} \\ \cos\theta \\ i\frac{\sin\theta}{\sqrt{2}} \end{pmatrix} \xrightarrow[q<0]{\text{quench}} \hat{\psi}_{\text{para.}} \sim \frac{1}{\sqrt{2}} \begin{pmatrix} 1 \\ 0 \\ 1 \end{pmatrix} .$$

The rotation does not change the spin of the system, which stays zero as can easily be seen by inserting $\hat{\psi}_{\text{seeded}}$ into Eqs. (2.13) – (2.15).

In the experiments the number of seeded particles varies between 3% to 10 %. In this work, we use a large seed in which 9.3% of the particles are initially

transferred to the side components, when not stated otherwise. The large seed has the advantage that the differences to the unseeded case are more pronounced, although they are also present with a small seed.

6.1 Evolution of a Single Realization in Real Space

We start with the study of a single realization in real space. The density and the spin is plotted for $q = -25$ Hz in Figure 6.1. One can see several differences to the unseeded case. The most prominent is a large, temporal oscillation of the particles between the $m = 0$ and the side components. The oscillation is spatially homogeneous and has a spin orientation in x-direction. A second difference is that the pattern formation starts at later times. We discuss the reason for this when we look at the spectra. The temporal oscillations can also be seen in F_z and interfere with the spatial oscillations. Firstly, we take a closer look at the oscillations.

The oscillation creates always a spin in x-direction and not in y-direction. If one uses initial condition in which the seed in the side modes is created by a rotation around the y-axis instead of the x-axis the oscillation creates a spin in y-direction. This shows that F_x and F_y are not degenerated anymore. This is only possible because the preparation of the initial state breaks the symmetry between the x- and y-direction. Although the expectation value of the spin is zero in both initial states, the fluctuations of the spin differ. One possibility to plot this in the spin basis is shown in Figure 6.2. The unseeded case can be seen as a flat disc in the x-y-plane. F_z is completely known and is zero. Because of the Heisenberg uncertainty this cannot be the case for F_x and F_y. This can also be seen in the numerical implementation. The initial fluctuations in z-direction are proportional to the square of the noise η^2, which we put in the system, while the fluctuations in the two other directions are proportional to $\rho_0\eta$. This changes through the rotation around the x-axis. Now F_z is not completely known anymore. The uncertainty of F_x stays the same, but the uncertainty of F_y becomes smaller and the x-y-symmetry is broken.

To gain a better understanding of the oscillations a single mode approximation (SMA) is helpful. The oscillations are spatially flat and symmetric in the side components $\psi_{\pm 1} = \psi_{\text{side}}$. Thus we can neglect the kinetic term, the F_z term and the interaction proportional to the density. In this approximation the phase of both side components stays the same and thus also F_y can be neglected. This

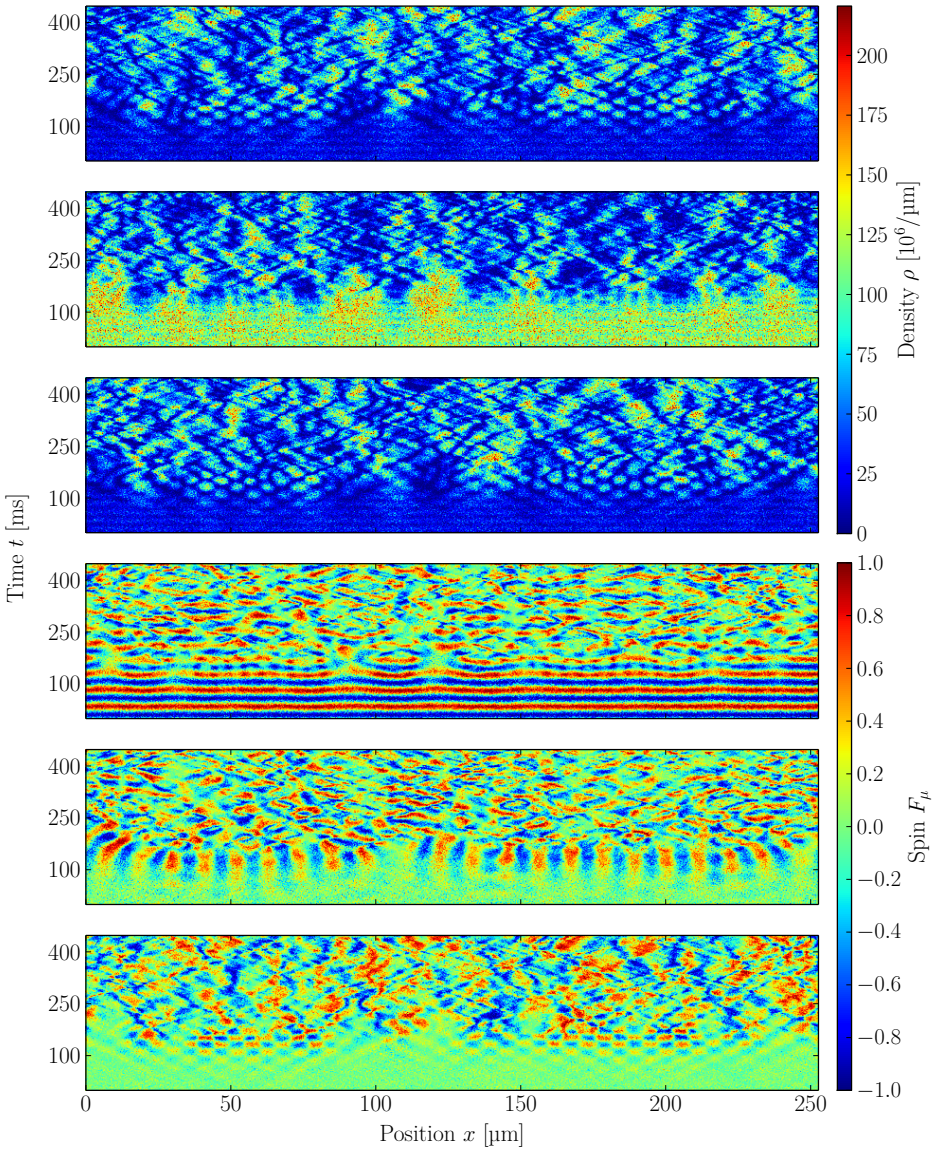

Figure 6.1: Numerical results of a single realization in position space for the seeded initial conditions. The parameters are: $\rho = 200 \cdot 10^6$ m^{-1}, $N_\mathrm{s} = 8192$, $L = 252.2$ µm, $q = -25$ Hz $= -3.04 \cdot nc_1$, couplings are given in Tab. 3.1, initially 9.3% of the particles are in the side modes. The first three plots show the density of the three components $m = 1$ (top), $m = 0$ (middle) and $m = -1$ (bottom). The last three plots show F_x (top) F_y (middle) and F_z (bottom). Particles oscillate between $m = 0$ and the side components at early times. This oscillation creates a spin in x-direction and there is also pattern formation in z-direction. At later times a pattern with a wavelength given by the Bogoliubov modes appears and the oscillation stops. The pattern is most pronounced at $t \sim 150$ ms. At later times the system gets irregular and one can observe solitonic defects.

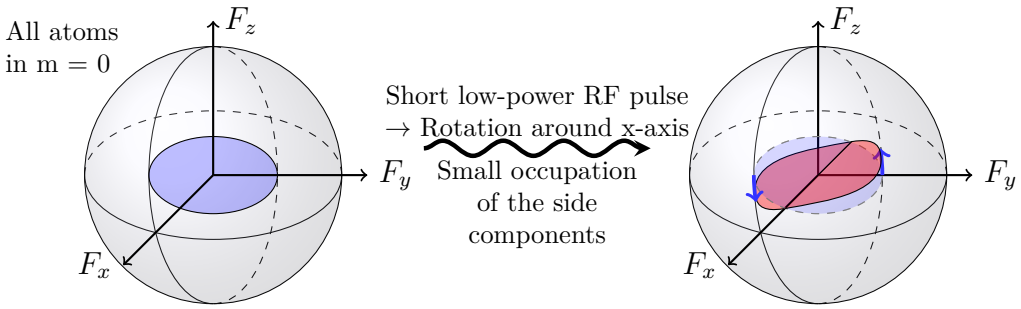

Figure 6.2: Symmetry breaking in the preparation of the seeded initial state. On the left side the unseeded initial state and on the right side the seeded initial state is shown in the spin basis. In the unseeded case F_z is exactly known and the uncertainty of F_x and F_y is equalt. The rotation around the x-axis lowers the uncertainty of F_y, but keeps the uncertainty of F_x. This breaks the symmetry between the x- and y-direction.

simplifies the time evolution of the three components Eqs. (2.20) – (2.22) to

$$i\frac{\partial \psi_\mathrm{s}}{\partial t} = q\psi_\mathrm{s} + c_1(\psi_\mathrm{s}^*\psi_0 + \psi_0^*\psi_\mathrm{s})\psi_0\,, \tag{6.2}$$

$$i\frac{\partial \psi_0}{\partial t} = 2c_1(\psi_\mathrm{s}^*\psi_0 + \psi_0^*\psi_\mathrm{s})\psi_\mathrm{s}\,. \tag{6.3}$$

These are non-linear, coupled differential equations. The numerical solution is plotted in Figure 6.3 together with the results of the simulation of the spatial extended system. One can see that the solution is periodic in time. In the early stages of the time evolution the simulation is well described by the SMA. The largest differences can be seen in the calculation of F_x, which never drops down to zero in the in the case of the spatial simulations. This can be explained by the quantum fluctuations which are not included in the SMA and always keep the value of F_x finite. At later times the influence of the spatial modes gets larger and the oscillations get smaller. The system cannot be longer described by the SMA.

It is possible to find a physical picture which explains the observed oscillation: Initially the system starts in a state where the phase difference between ψ_side and ψ_0 is $\pi/2$. The spin of this state is zero and hence there is no coupling between the three components (compare Eqs. (6.2) and (6.3)). The side components have a energy which is lowered by an amount of q. Therefore their phases evolve slower in time and the phase difference between ψ_side and ψ_0 changes. This creates a spin in x-direction. It is maximal at a phase difference of 0 and π. The modes couple until F_x vanishes again. During the coupling the occupation of the components changes. This has also an influence on the value of F_x and is the reason why the process is not described by a harmonic oscillation.

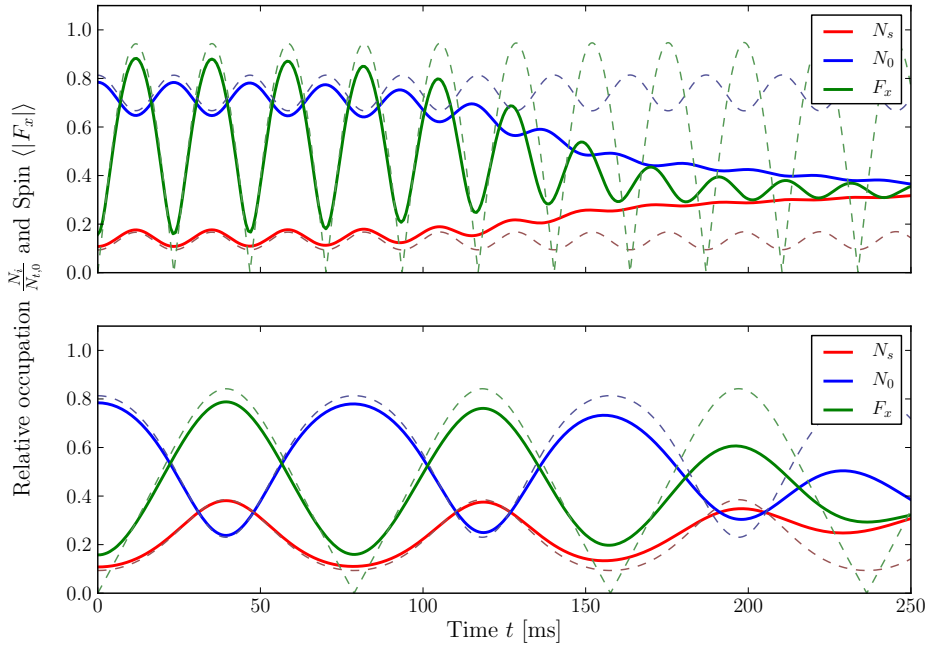

Figure 6.3: Comparison of particle numbers in each mode of the whole spatial simulation with the single mode approximation Eqs. (6.2) and (6.3). In addition the absolute value of the spatially averaged, normalized spin in x-direction is shown. In the upper plot $q \sim -0.54 \cdot c_1\rho$ and in the lower plot $q \sim -2.70 \cdot c_1\rho$. The oscillation amplitude and frequency strongly depends on q. For early times the spatial simulations are well described by the SMA. At later times spatial modes are excited and the single mode approximation breaks down. This happens earlier for large values of q.

We can also solve Eqs. (6.2) and (6.3) analytically. For that we use an approach from [43]. First we split the wave functions into their amplitudes and their phases:

$$\psi_0 = \sqrt{\rho_0} e^{-i\theta_0} \,, \tag{6.4}$$

$$\psi_\mathrm{s} = \sqrt{\rho_\mathrm{s}} e^{-i\theta_\mathrm{s}} \,. \tag{6.5}$$

The total density is given by $\rho_0 + 2\rho_\mathrm{s} = \rho$. Using these equations, Eqs. (6.2) and (6.3) can be written as

$$i\frac{\dot{\rho}_\mathrm{s}}{\rho_\mathrm{s}} + \dot{\theta}_\mathrm{s} = q + c_1\rho_0(e^{i\theta} + 1) \,, \tag{6.6}$$

$$i\frac{\dot{\rho}_0}{\rho_0} + \dot{\theta}_0 = 2c_1\rho_\mathrm{s}(e^{-i\theta} + 1) \,, \tag{6.7}$$

where we used $\theta = 2\theta_\mathrm{s} - 2\theta_0$. ρ_j and θ_j are real quantities and we can therefore split both equations in their real and imaginary parts. The imaginary parts give the time evolution of the densities and the real parts the time evolution of the phases

$$\dot{\rho}_\mathrm{s} = c_1\rho_\mathrm{s}\rho_0 \sin(\theta)\,, \tag{6.8}$$
$$\dot{\rho}_0 = -2c_1\rho_\mathrm{s}\rho_0 \sin(\theta)\,, \tag{6.9}$$
$$\dot{\theta}_\mathrm{s} = q + c_1\rho_0(\cos(\theta)+1)\,, \tag{6.10}$$
$$\dot{\theta}_0 = 2c_1\rho_\mathrm{s}(\cos(\theta)+1)\,, \tag{6.11}$$
$$\dot{\theta} = 2q + 2c_1(\rho_0 - 2\rho_\mathrm{s})(\cos(\theta)+1)\,. \tag{6.12}$$

The first two equations are consistent with $2\rho_\mathrm{s} + \rho_0 = \rho$. The energy of the system in the SMA is given by

$$E = q(\rho - \rho_0) + c_1\rho_0(\rho - \rho_0)(1 + \cos(\theta))\,. \tag{6.13}$$

Eventually, the purpose of this calculations to yield an expression for the time of one period to compare it with experiment and simulation. Therefore we calculate the square of the time derivative Eq. (6.9) of ρ_0

$$(\dot{\rho_0})^2 = 4[E - q(\rho - \rho_0)][(2c_1\rho_0 + q)(\rho - \rho_0) - E]\,. \tag{6.14}$$

which depends on the energy E, but is independent of θ. ρ_0 is a real quantity and thus only positive values on the right hand side have a physical meaning. To find the regime in which the function is positive we calculate their roots x_i

$$x_j = \frac{\rho_0}{\rho}\,, \tag{6.15}$$
$$x_{k,l} = \frac{2c_1\rho - q \pm \sqrt{(2c_1\rho - q)^2 - 8c_1\rho(q-E)}}{4c_1\rho}\,. \tag{6.16}$$

In the following we use $x_1 = \min(x_j, x_k, x_l)$ and $x_3 = \max(x_j, x_k, x_l)$. Using the roots one can write the square of the time derivative as

$$(\dot{\rho_0})^2 = -8c_1\rho q(\rho_0 - x_1)(\rho_0 - x_2)(\rho_0 - x_3)\,. \tag{6.17}$$

To find the duration of one period we take a closer look at this function. Since ρ_0 is a real quantity only positive values for $\dot{\rho_0}$ are physical. In our case $c_1\rho < 0$. Hence the function goes to $-\infty$ for $\rho_0 \to -\infty$ and to ∞ for $\rho_0 \to \infty$. This means the function is positive for $\rho_0 \in [x_1, x_2]$ and for $\rho_0 > 0$, but the latter case is unstable. The stable solution is the oscillation of ρ_0 between x_1 and x_2.

The duration of one period is given by the time which the density needs to change from one of these values to the other:

$$\begin{aligned} T &= \oint \frac{1}{\dot{\rho}_0} \mathrm{d}\rho_0 \\ &= \sqrt{\frac{1}{2|c_1 \rho q|}} \int_{x_1}^{x_2} \frac{\mathrm{d}\rho_0}{\sqrt{[\rho_0 - x_1][\rho_0 - x_2][\rho_0 - x_3]}} \,. \end{aligned} \tag{6.18}$$

Such equations can be solved by complete elliptic integrals of the first kind

$$K(k) = \int_0^1 \frac{\mathrm{d}t}{\sqrt{(1-t^2)(1-k^2 t^2)}} \,. \tag{6.19}$$

To bring Eq. (6.18) in this form one first needs to shift the integration parameter by x_1: $\rho_0 \to \rho_0 + x_1$ and then rescale it by $(x_2 - x_1)$: $\rho_0 \to (x_2 - x_1)\rho_0$. This results in

$$\begin{aligned} T &= \sqrt{\frac{1}{2|c_1 \rho q|}} \int_0^1 \frac{(x_2 - x_1)\mathrm{d}\rho_0'}{\sqrt{(x_2 - x_1)^3 \rho_0' [\rho_0' - 1][\rho_0' - \frac{x_3 - x_1}{x_2 - x_1}]}} \\ &= \sqrt{\frac{1}{2|c_1 \rho q|(x_3 - x_1)}} \int_0^1 \frac{\mathrm{d}\rho_0'}{\sqrt{\rho_0'[1 - \rho_0'][1 - \frac{x_2 - x_1}{x_3 - x_1}\rho_0']}} \,. \end{aligned} \tag{6.20}$$

The last step is the substitution $\rho_0 = t^2 \to \mathrm{d}\rho_0 = 2t\ \mathrm{d}t$. We get

$$\begin{aligned} T &= \sqrt{\frac{2}{|c_1 \rho q|(x_3 - x_1)}} \int_0^1 \frac{\mathrm{d}t}{\sqrt{[1 - t^2][1 - \frac{x_2 - x_1}{x_3 - x_1} t^2]}} \\ &= \sqrt{\frac{2}{|c_1 \rho q|(x_3 - x_1)}} K\left(\sqrt{\frac{x_2 - x_1}{x_3 - x_1}}\right) \,. \end{aligned} \tag{6.21}$$

The oscillation period is therefore a complicated function which depends on the coupling strength c_1, the Zeeman effect q and the total density ρ. Through the roots x_i it also depends on the energy of the system E and hence on the strength of the seed.

6.2 Oscillations in the Experiment

The oscillation described in the previous section can also be measured in the experiment. It is clearly visible at early times and stops 80 – 110 ms after the quench. Depending on the frequency, one can see up to four periods. In this section, we compare frequencies measured in the experiment [32] with the

analytic predictions of the SMA, see Eq. (6.21) and with numerical results. They are plotted in Figure 6.4 for three different seed strengths. One can observe that the frequencies increase with q and with the strength of the seed. The SMA and the numerical results show a very high agreement in all three cases. The results of the experiments are also well described by the SMA, but the deviations are larger. The experimental results agree best with the theoretic predictions in the case of the largest seed. The frequencies can be measured quite exact in the experiment and can be used to fit the parameters of the experiment. If the ratio of the total density ρ to the initial density of the $m = 0$ component is fixed, the SMA only depends on the product $c_1\rho$ and not on c_1 and ρ on its own. In Figure 6.4 the predictions of the SMA for a larger value of $c_1\rho$ are shown, which show a better agreement with the experimental results.

6.3 Spectra and Density-Density Correlation

In this section, we examine the spectrum of the three hyperfine states, of the spins and of the quadrupole moments. We also take a look at the density-density correlation $G^{(m)}_{\rho,\rho}(k)$. Most phenomena which we identified in the unseeded case are also present in the seeded case, but are slightly different. We focus here on the differences and the new phenomena. The mentioned quantities are plotted in Figure 6.5. We also plot the spectra of F_x because F_x and F_y are not degenerated anymore. In all spectra we can find more peaks as in the unseeded case and also their temporal behavior is different. The most pronounced peaks of the unseeded case can also be observed with the seed, but they are at slightly higher momenta. The highest peaks are again created by particles from the $m = 0$ component scattering into the side component with a phase corresponding to a spin in the x-y plane, but this process gives in the seeded case more energy. For simplicity we consider the creation of a spin in x-direction of a particle changing its hyperfine state from $m = 0$ to $m = 1$. The Zeeman energy of the particles changes by q. The energy of F_x is given by $c_1\rho_0\rho_1$, see Eqs. (2.13) and (2.19). If one assumes $\rho_0 \gg \rho_1$ and that the densities of the components are so high, that the scattering of a single pair of atoms does not change them, the change of energy through the spin creation is $c_1(\rho_0 - \rho_1)$. This energy is converted into kinetic energy

$$\frac{k^2}{2M} = -q - c_1(\rho_0 - \rho_1)\,. \tag{6.22}$$

During the early stages of the time evolution the density in the components changes due to the particle oscillation. This changes also the energy which is

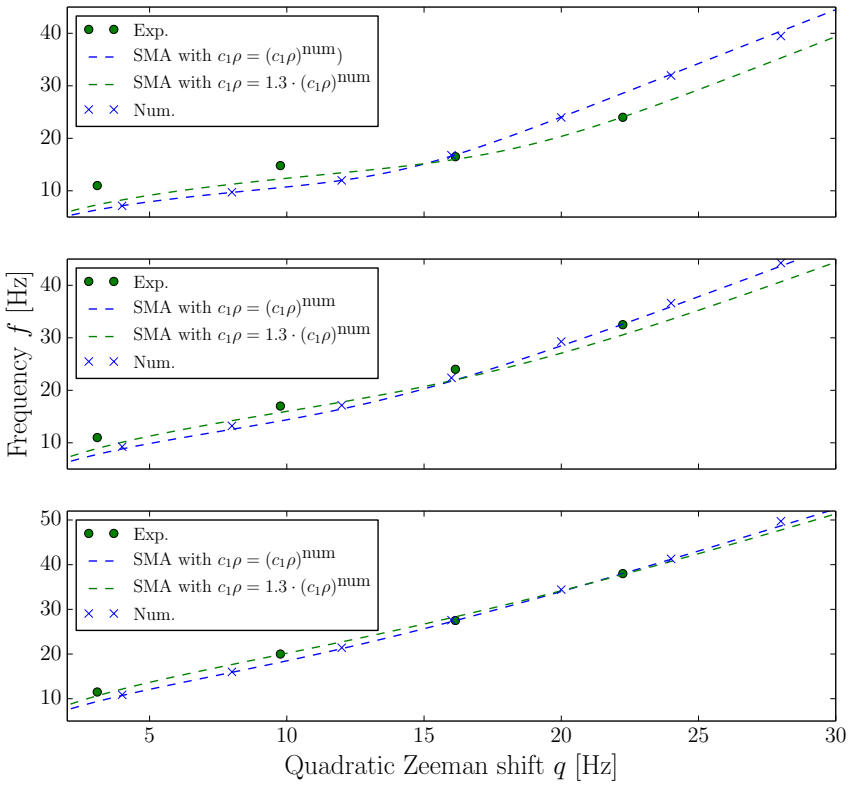

Figure 6.4: Comparison of oscillation frequencies in the experiment [32] (green dots), simulations (blue crosses) and the SMA Eq. (6.21) (dashed lines) for different values of q. Three different seed strengths are compared, in which 3 % (top), 8 % (middle) and 19 % (bottom) are initially in the side components. The parameters of the simulations are: $\rho = 180 \cdot 10^6$ m^{-1}, $N_s = 8192$, $L = 252.2$ µm. The results are averaged over 100 runs. The SMA is given for the values of the simulations (blue) and for an increased value of the product $c_1\rho$ (green), which gives a better agreement with the results of the experiment.

needed for the creation of the spin. It turns out that the above approximation improves if one takes the oscillations into account by averaging the density over the first oscillation period:

$$\frac{k_{\text{sd}}^2}{2M} = -q - c_1(\langle\rho_0\rangle_{\text{1. period}} - \langle\rho_1\rangle_{\text{1. period}})\,. \tag{6.23}$$

where we use k_{sd} in the following to describe the position of excitations with the corresponding energy. If we insert the initial values of the unseeded case, $\rho_0 = \rho$ and $\rho_1 = 0$, in this equation, we get the momentum of the most unstable Bogoliubov mode Eq. (4.17). For the seeded case the momenta are larger. They are marked in Figure 6.5 as dotted lines. One can see that the position of many excitations can be explained by this approximation. At early times there is a high peak at k_{sd} in $n^{(1)}(k)$. Similar to the unseeded case, the particle

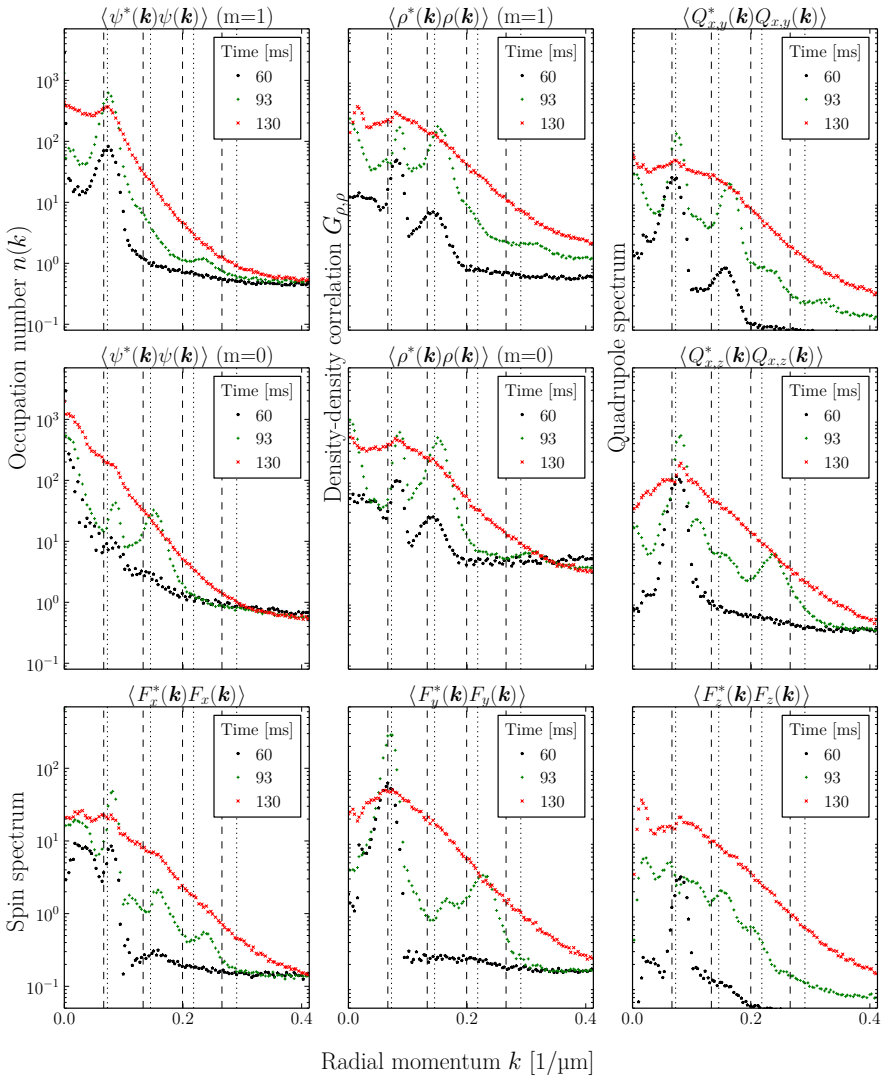

Figure 6.5: Spectra of the hyperfine states, the spins and of the quadrupole moments and the density-density correlations $G^{(m)}_{\rho,\rho}(k)$ for three different times. The same parameters as in Figure 6.1 are used. The quantities are averaged over 1000 runs. For orientation the position of the most unstable Bogoliubov mode $k_{\mathrm{m.u.}} = 0.085\ \mu\mathrm{m}^{-1}$ of the unseeded case and multiples thereof (dashed lines) are marked. In addition we plot the position of the momentum of an approximation Eq. 6.23 which considers the initial seed and multiples thereof (pointed lines). 90 ms after the quench first excitations are visible as peaks. The number of peaks increases over time. At late times the peaks smear out and the spectra fall off exponentially.

of this mode interact with the condensate and peaks at multiples of k_{sd} emerge. In addition there are also new excitations. For example there are small peaks at k_{sd} in $n^{(0)}(k)$ and at $2k_{\mathrm{sd}}$ in $n^{(1)}(k)$ that are not there in the unseeded case. They can be created by interactions where particles of the seed ($k = 0$ and $m = \pm 1$) take part. A possible process which scatters particles into the k_{sd} mode in $n^{(0)}(k)$ is given by

$$i\dot{\psi}_{k_{\mathrm{sd}},0} \sim c_0 \psi_{k_{\mathrm{sd}},\mathrm{s}} \psi^*_{0,\mathrm{s}} \psi_{0,0} \,, \tag{6.24}$$

and a process which excites particles into the $2k_{\mathrm{sd}}$ mode in $n^{(1)}(k)$ is

$$i\dot{\psi}_{2k_{\mathrm{sd}},\mathrm{s}} \sim c_0 \psi_{k_{\mathrm{sd}},\mathrm{s}} \psi^*_{0,\mathrm{s}} \psi_{k_{\mathrm{sd}},\mathrm{s}} \,. \tag{6.25}$$

Another difference is that the height of the peaks oscillates. Small oscillations can be seen in all functions, but they are very large in $G^{(m)}_{\rho,\rho}(k)$ and F_z. The oscillations in $G^{(m)}_{\rho,\rho}(k)$ can be explained by the particle oscillation between $m = 0$ and the side components. This changes the number of particles in the condensate mode of the components. Using Eq. (5.6) one can see that this changes also the height of the peaks in $G^{(m)}_{\rho,\rho}(k)$. The oscillation in F_z has the same frequency and can be seen in the position space plots in Figure 6.1.

There are further new peaks at $k \approx 0.05$ µm. They are clearly visible in $G^{(m)}_{\rho,\rho}(k)$ and can be seen as small oscillating peaks in $n^{(m)}(k)$. There is no corresponding excitation in the unseeded case and the origin of these excitations needs further study.

In Figure 6.6 the positions of the peaks in $n^{(m)}(k)$ and $G^{(m)}_{\rho,\rho}(k)$ at $t \approx 240$ ms are shown. Most peaks can be again explained by the creation of a primary peak at k_{sd} and subsequently scattering of particles with k_{sd} to higher frequencies. These peaks can be found in both components, because of the new condensate mode in the side components. As already discussed the condensate mode is also the reason that there are now peaks at all multiples of k_{s} in $G^{(m)}_{\rho,\rho}(k)$. The temporal oscillations of the peaks make the detection of small peaks more difficult and the algorithm misses some of them. One can see in the plot that sometimes a peak is found for some q values by not for others.

Figure 6.7 shows the time evolution of the occupation numbers at the position of the peaks for two different densities. Similar to the unseeded case in the beginning a primary mode starts to grow exponentially and secondary modes grow at later times with even higher growth rates. A difference to the unseeded case are oscillations in the growth rates. These oscillations can be seen in all modes and they are most pronounced at the new peak at $k \approx 0.04$ µm and for the peak at $2k_{\mathrm{sd}}$. They are caused by the large particle oscillation between $m = 0$ and the side components. The primary peak is created by

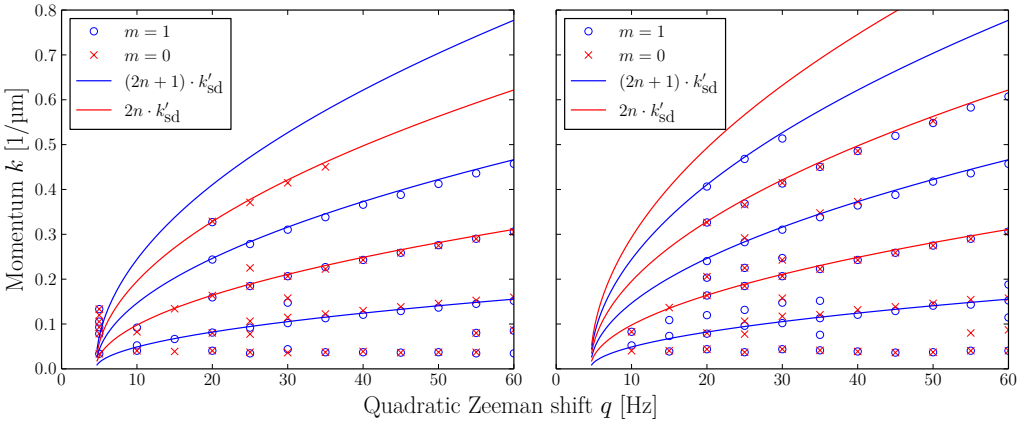

Figure 6.6: Position of the peaks of $n^{(m)}(k)$ (left) and $G^{(m)}_{\rho,\rho}(k)$ (right) for different values of the quadratic Zeeman effect q at $t \approx 240$ ms. The parameters are: $N_s = 16384$, $L = 754.9$ µm, couplings are given in Tab. 3.1 and the density is increased to $R = 50000$ as described in Sec. 3.3. The spectra are averaged over 200 runs before the peaks are detected. For orientation the position of k_{s} Eq. (6.23) for $\langle \rho_0 \rangle = 0.7\rho$ and $\langle \rho_1 \rangle = 0.15\rho$ and multiples of it are plotted (even multiples: red solid lines, odd multiples: blue solid lines). There are excitations at k_{s} and multiples of it, but also excitations which cannot be described by interactions with this mode.

interactions of particles in $m = 0$. Through the oscillations the number of particles in $m = 0$ drops down periodically. During this time the excitation of the k_{sd} mode is suppressed. The peak at $2k_{\mathrm{sd}}$ is created by interactions of particles in the condensate with particles in k_{sd} mode. This explains that the oscillations of the particles in the condensate also influence the growth rates of the $2k_{\mathrm{sd}}$ mode. It also has an influence on higher modes. Presumably the oscillations are the main reason for the slower time evolution in the seeded case in comparison to the unseeded case. The growth of the primary and secondary excitations is slowed down. Hence the formation of pattern and also the subsequent creation of solitonic excitations starts at later times.

We now take a look at the system at times where the peaks have smeared out. Similar to the unseeded case one can observe an exponential decay in $n^{(m)}(k)$ and $G^{(m)}_{\rho,\rho}(k)$ in all three components. In Figure 6.8 the decay lengths ξ for the seeded and unseeded case at $t \approx 450$ ms are shown. We do not compare the decay lengths for the corresponding values of q directly. Instead we calculate the energy which we put into the system through the quench. We assign each atom which is initially in the $m = 0$ mode an energy of q and then calculate a mean energy for all atoms. Thereby also the particles which are put into the system through the noise are taken into account. One can observe that the decay rates depend mainly on the energy added to the system through the

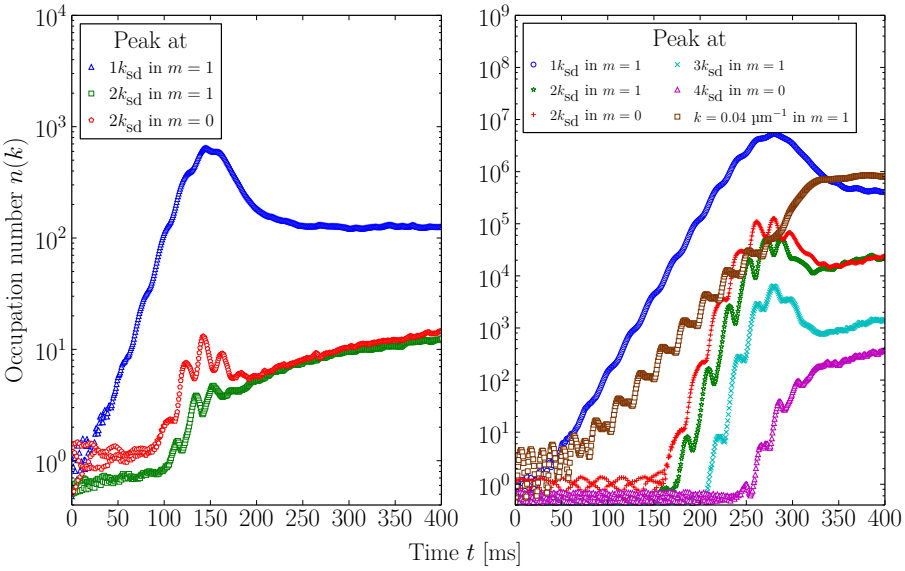

Figure 6.7: Time evolution of the occupation numbers of the Peaks at k_{sd} and multiples thereof. Note the different scales on the y-axis. On the left side averaged values over 1000 runs with the parameters given in Figure 5.1 are plotted. The parameters for the right plot are the same except for: $R = 50000$ as described in Sec. 3.3, $L = 754.9$ µm and $N_s = 16384$. Here 200 runs are averaged. In the right plot also $k = 0.34$ µm is shown. One can see exponential growth of the modes similar to the unseeded case, but an additional oscillation of the occupation number can be observed. The primary mode grows from the beginning and secondary modes start to grow at later times.

quench and not directly on the values of q. The details of the initial conditions are not important for this stage of the time evolution but the state of the system depends mainly on the value of a few conserved quantities like the total energy of the system and the number of particles. This is an important feature of the process of thermalization. In the thermal equilibrium the system has no memory about the details of the initial conditions. However, our system has not reached the thermal equilibrium yet. The number of particles in the three hyperfine states are still changing slowly (see Figure 5.4) and also the decay lengths have not reached a fixed value yet (see Figure 5.13). This can indicate that the system has reached a so called prethermalized state [7]. A system is called prethermalized if it is in a state where some observables have already reached their thermal equilibrium while other quantities still differ from their equilibrium value. For example, the occupation numbers of the momentum modes of the system can be far away from the equilibrium distribution but the kinetic energy has already reached its final value. This value can be used to determine the equilibrium temperature of the system. Thereby the time scales

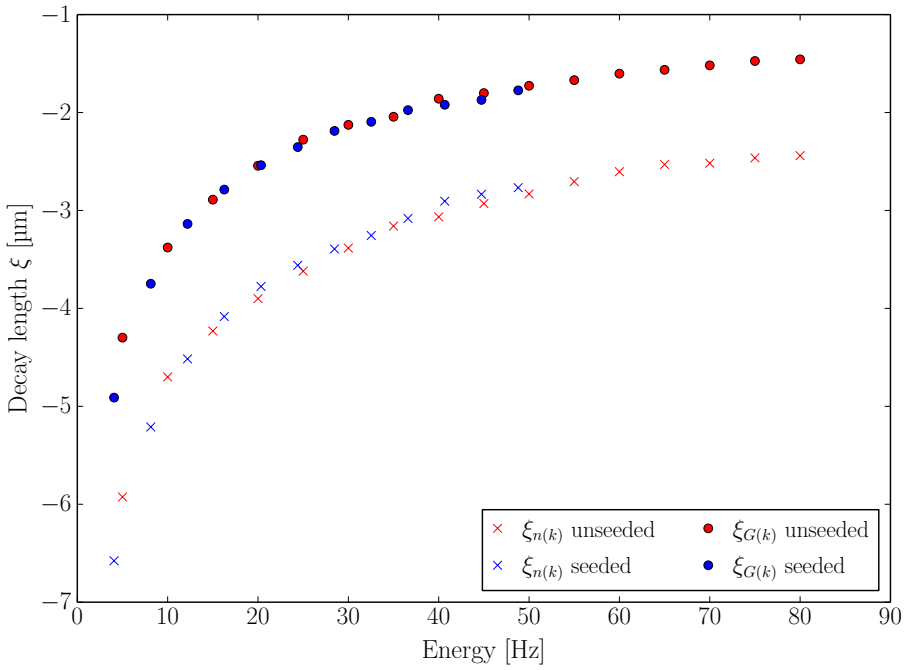

Figure 6.8: Decay lengths $\xi_{n(k)}$ and $\xi_{G(k)}$ for the unseeded and seeded initial conditions at $t \approx 450$ ms as a function of the energy which is added to the system through the quench. The parameters of the experiment are used as given in Figure 5.1 and Figure 6.1. The spectra are averaged over 400 runs. Subsequently the decay lengths of ten time steps are averaged. The q values corresponding to the displayed energies are between 5 Hz and 60 Hz for the seeded initial conditions and between 5 Hz and 80 Hz for the unseeded case.

at which the observables reach their equilibrium value can be very different and the system can stay for long times in a quasi-stationary, prethermalized state. It was shown this phenomena can also occur in Bose gases [8, 61]. It needs further study to clarify if the quasi-steady state which our system reaches at late times is prethermalized.

6.4 Density-Density Correlations in the Experiment

In this section, we compare the density-density correlations measured in the experiment [32] with numerical data. The experimental measurements are again with $B = 1.213$ G and $q = -30$ Hz, $q = -33$ Hz and $q = -36$ Hz. In Figure 6.9 we compare the results with numerical data for $q = -10$ Hz,

$q = -15$ Hz and $q = -20$ Hz. In the experiment one can see one peak around $k = 0.5$ µm clearly and a smaller second peak at twice the momentum. For larger q the second peak is more pronounced and the positions of the peaks shift to higher momenta. Also the effect of the oscillations is visible. Depending on the q values there are times between $t = 20$ ms and $t = 70$ ms, where the height of the peak stays almost the same and times, where it increases very fast. For example for $q = 36$ Hz the height of the peak makes two large jumps between $t = 20$ – 30 ms and $t = 60$ – 70 ms, while it stays almost the same and even slightly decreases in the intermediate time. This phenomenon was not visible in the experimental results of the unseeded case. Another difference to the unseeded case is the time interval in which the peaks are visible. In the case with seed the peaks get smeared out at $t \approx 140$ ms, while in the unseeded case the peaks vanish at $t \approx 100$ ms.

The numerical data show a good agreement with the experimental results. As in the experiment the peaks are visible for longer times. The positions of the peaks are very similar, but presumably one can find q values where the agreement is higher. One difference is that the second peak is more pronounced in the numerical data and in the case of $q = -20$ Hz even a third peak is visible. As discussed in Sec 5.5 there are several explanations for the differences between numerical and experimental data.

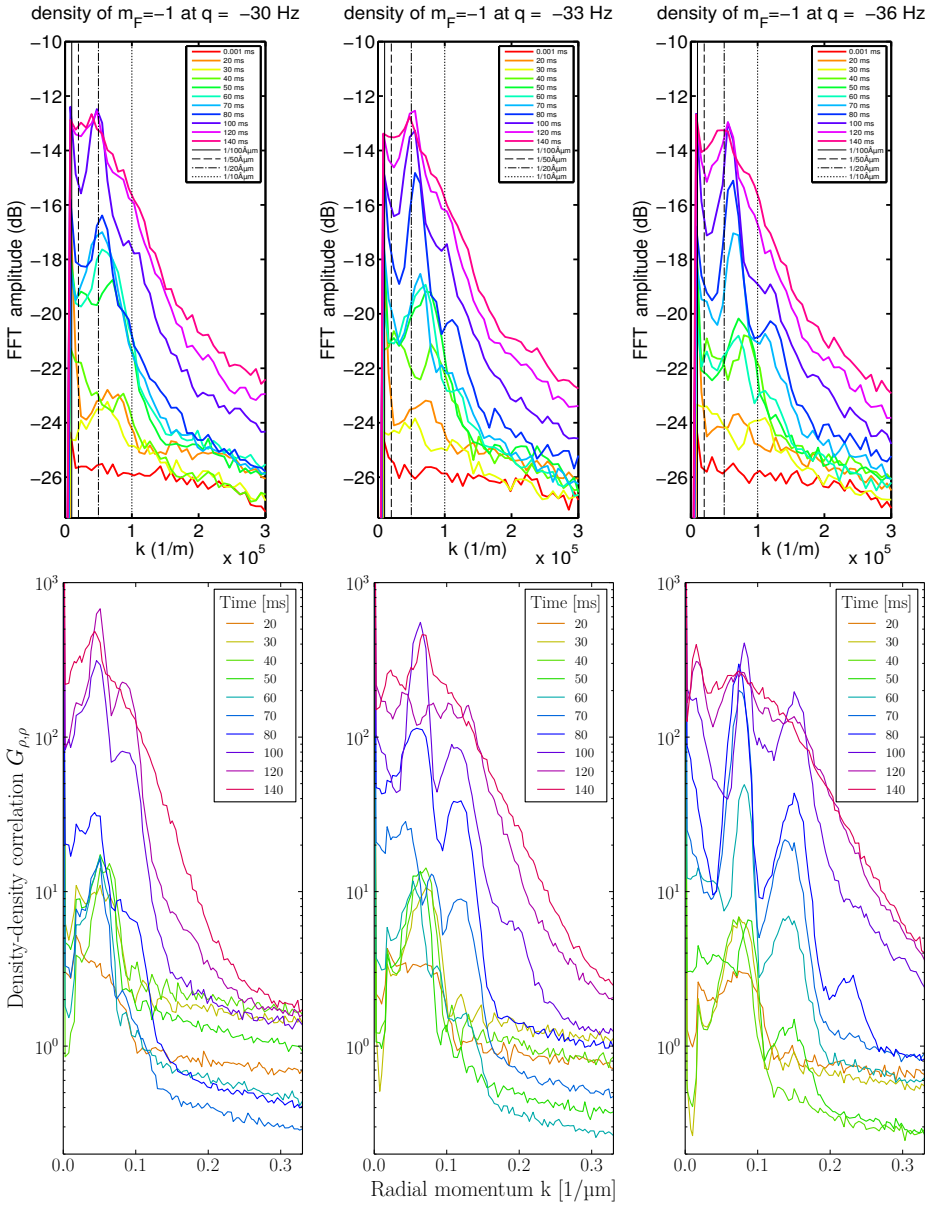

Figure 6.9: Experimental (top) and numerical results (bottom) for $G_{\rho,\rho}(k)$ in $m = -1$ in comparison. The experimental results are from [32] and the $k = 0$ value is set to zero. The Zeeman shifts calculated for the experiments are $q = -30$ Hz (left), $q = -33$ Hz (middle) and $q = -36$ Hz (right). Initially $\approx 3\%$ of the particles are transferred into the side components. The results agree better, if smaller values are used in the simulations. Here we show the results for $q = -10$ Hz (left), $q = -15$ Hz (middle) and $q = -20$ Hz (right). The numerical results are averaged over 400 runs. The parameters are: $\rho = 240 \cdot 10^6$ m^{-1}, $N_s = 8192$, $L = 252.2$ µm, couplings are given in Tab. 3.1. The same seed as in the experiment is used.

7

Conclusion

In this thesis, we studied the non-equilibrium dynamics of a spin-1 Bose gas in one spatial dimension numerically and analytically. We investigated the time evolution of the BEC after a quench for two different initial conditions. First, we studied the *unseeded* case where the system is prepared in the polar phase. The side components are initially empty and one has to take only quantum fluctuations into account. One part of this work was to compare the influence of the quantum fluctuations with the influence of real particles. Therefore we prepared the system in the *seeded* case in a state in which initially the side components are weakly occupied. In both cases the system is driven out of equilibrium by an external magnetic field which lowers the energy of the side components by the quadratic Zeeman shift q. We compared the numerical and analytic results with experiments of the Group of Prof. M. Oberthaler [32] where ^{87}Rb in the $F = 2$ hyperfine manifold are studied. We showed that for the described initial conditions the early stages of the time evolution of the five-component $F = 2$ system in the experiment can be well described by an effective three-component system for which we determined the effective coupling constants.

First, we investigated the unseeded case. In the early stages of the time evolution we observed spin excitations, which can be described by Bogoliubov theory. We used the Bogoliubov approximation to calculate the primary modes, which become unstable, if a condensate in the polar phase is quenched into the paramagnetic regime. The momentum region of unstable modes depends on the strength of the quench. For small external fields the most unstable modes have zero momentum and the excitations can be seen as a peak around $k = 0$ in the occupation spectra of the side components. For larger negative values of q the momentum of the most unstable mode $k_{\mathrm{m.u.}}$ becomes finite. In this case, we observed the excitation of secondary modes with momenta, which are multiples of $k_{\mathrm{m.u.}}$. We explained this by interactions of particles of the primary

mode with particles in the condensate. Such rescattering processes are not described by mean-field-type approximations and show that nonlinear effects play an important role in the system. Using momentum conservation we could explain why we find secondary modes with odd multiples of $k_{\mathrm{m.u.}}$ in the side components and at even multiples in the $m = 0$ component. We saw that the number of secondary modes depends on the density in the system. For small densities quantum fluctuations have more influence on the system. The system is more chaotic and the excitation of secondary modes is suppressed.

Bogoliubov theory proposes an exponential growth of the unstable modes and also predicts the corresponding growth rates τ_{Bog}^{-1}. The growth rates of the Bogoliubov excitations measured in the simulations agree very well with this predictions. We found that also the secondary excitations grow exponentially. Thereby their growth rates depend on the density of the system. They increase for high densities and approach a constant value. Thereby the highest growth rate measured for a mode with momentum $n \cdot k_{\mathrm{m.u.}}$ is given by $n \cdot \tau_{\mathrm{Bog}}^{-1}$. It is possible to predict the approached values if one uses an approximation where only the modes at the positions of the peaks are considered. We found similar excitations in the spectra of the spins. They show the same relation between the position of the peaks and their growth rates. The excitation of secondary modes was also found in the study of parametric resonances in a relativistic field theory in three spatial dimensions from J. Berges and J. Serreau [35]. In this work a primary mode which is excited by the parametric resonance grows exponentially with a rate γ. At later times a broad range of longitudinal modes starts to grow with a rate 2γ and transverse mode grows with 3γ. The growth rates of these modes can be explained using the formalism of the two-particle irreducible effective action [62]. On the one hand the excitations of secondaries found in this work show some common features. We also found that at first longitudinal modes are excited with $2\tau_{\mathrm{Bog}}^{-1}$ and then transverse modes with $3\tau_{\mathrm{Bog}}^{-1}$. On the other hand there are also some differences. The primary mode is not excited by a parametric resonance, but a region of unstable modes is created by changing the ground state of the system. In our simulations, which consider only one spatial dimension, the momentum range of secondary excitations is small and modes are visible as isolated peaks in the spectra. We also found growth rates, which are higher than three times the growth rate of the primary mode. This can be explained by interactions in which particles of secondary modes take part. This demonstrated that our system provides a great opportunity to study nonlinear effects of a quantum field theory in a very controlled manner. It can be used to get a better understanding for other processes in which similar effects play an important role like the preheating of the universe after inflation [38–40] or heavy ion collision [41, 42].

To compare the numerical results with the experiment we calculated the

density-density correlations. In the experiment the wave function of the three hyperfine states is not measured directly. Instead the components are separated by a Stern-Gerlach splitting and their densities are measured. We demonstrated that the relation between the spectra of the wave function and the Fourier transformation of the density is not trivial. The phases of the wave functions and the occupations of the condensate modes play an important role. It was possible to explain why the density-density correlations of the three components look very similar, while their spectra are very different. We found the best agreement between the numerical and experimental data, if we used smaller values for the quadratic Zeeman than calculated for the parameters of the experiment. For these values we found very similar excitations and also the time scales agree very well. Thereby the parameters of the experiment are in a regime where both in the simulations and in the experiment only the first secondary excitation is visible. The primary excitation can be seen as a peak at $2k_{\mathrm{m.u.}}$ in the density-density correlations of the side components and the secondary modes are visible as a peak at same position in the corresponding function of the $m = 0$ component.

In the second part of this work we investigated the seeded initial conditions. In this case we observed new phenomena but also similar excitations as in the unseeded case. It turns out that the phase differences between the wave functions of the modes play an important role. Through the preparation of the seeded case the initial phase difference between the three components is fixed, while this is not the case without seed. The fixed phase differences cause large particle oscillations between the $m = 0$ component and the side components. The oscillation create a spin excitation in x-direction, but not in y-direction. This is possible because the preparation of the seeded initial conditions breaks the $SO(2)$ symmetry in the x-y plane, which the system possesses in the unseeded case. The early stages of the oscillation are well described by a single mode approximation (SMA) [43, 63]. Such oscillations have been recently used to study non-equilibrium dynamics of ^{87}Rb in tightly confined optical traps [64].

The predicted frequencies of the SMA agree very well the simulation, while there are small deviations in the experimental results. The oscillation frequencies can be measured very exactly in the experiment which presumably can be used to fit some parameters of the experiment. The oscillations also have a large influence on the excitations of the modes. As in the unseeded case one can observe the excitation of a primary mode and of secondary modes. Thereby the momenta of the modes are slightly higher. The reason for this is that particles scattering from the $m = 0$ mode into the side modes create a smaller spin and thus the kinetic energy after the scattering is larger. There are more excitations observable than in the unseeded case. One reason is that

particles of the primary mode can scatter with the seeded particles. This creates excitations which can not be seen without the initial condensate in the side modes. However, there are also new excitations at low momenta in all three components, which need further study. We demonstrated that the oscillation has also influence on the time evolution of the excited modes. The occupation number of the excited modes oscillates and the whole time evolution is slowed down. The formation of a pattern starts at later times and the peaks in the spectrum are visible for longer times. This can also be seen in experimental results. If one uses the same smaller values for q as in the unseeded case, the density-density correlations of the simulations agree very well with experimental results.

For both initial conditions the peaks smear out at late times. One can observe that the occupation numbers of all three components fall off exponentially with k. This can also be seen in the density-density correlations both of the experiment and the simulation. We showed in position space plots that the system is dominated by topological defects and we could observe solition-like excitations. It needs further study to determine the exact types of the defects and their influence on the time evolution. We found that the system has lost the memory of the initial conditions. For both initial conditions the decay lengths in the spectra depend mainly on the energy that was added to the system through the quench. The system stays for long times in this quasi-steady state and all observables change only slowly. To determine if the system has reached a prethermalized state needs further study.

Finally, we want to mention that recently new experimental measurements were performed in which also the spectrum of the spin in y-direction was determined. Here one can observe new phenomena. The unstable modes predicted from Bogoliubov theory are only excited for certain values of q. It seems that the trap used in the experiment has an influence on the possible excitations. These observations are not yet completely understood and need further study. Presumably the implementation of the trap in the simulation can help to understand the new results. In this work, we showed that semi-classical simulations in homogeneous space can describe many observations of the experiment and can be used to get a better understanding of the phenomenology in the system. We got a good understanding of the early stages of the time evolution after the quench. For most phenomena we found both physical and analytic explanations. However, there are still interesting open questions. Especially the state of the system at late times where the time evolution slows down and the system is dominated by topological defects needs further investigations.

A

Appendix

A.1 Density and Wave Function in Fourier Space

In the experiments described in Sec. 3.1 it is not possible to measure the wave function directly. Instead the accessible quantity is the density. In this section we calculate the density for a wave function with one, respectively two strongly occupied modes. At first we want to assume the most general case in which one mode k_1 in the wave function is excited

$$\psi(x) = A_{R1}\cos(k_1 x + \phi_{R1}) + iA_{I1}\cos(k_1 x + \phi_{I1})\,, \tag{A.1}$$

with $A_{R1}, A_{I1} \in \mathbb{R}$. We shift the wave such that $\phi_{R1} = 0$. In this case the density is given by

$$\begin{aligned}\rho(x) &= |A_{R1}\cos(k_1 x) + iA_{I1}\cos(k_1 x + \phi_1)|^2 \\ &= \frac{A_{R1}^2}{2}\left(\cos 2k_1 x + 1\right) + \frac{A_{I1}^2}{2}\left(\cos\left(2k_1 x + 2\phi_1\right) + 1\right)\,,\end{aligned} \tag{A.2}$$

where $\phi_1 = \phi_{I1} - \phi_{R1}$. The crossterms cancel and one gets a real quantity. Here one can see two important points. First, every mode in the wave function gives a contribution to the $k = 0$ mode of the density. The reason is that the density can only have positive values. The $k = 0$ mode depends on the mean-density of the field. Second, a highly occupied mode k_1 in the wave function corresponds to a k-vector of $2k_1$ in the density. However, there can be an additional effect: If the phase difference is $\phi_1 = \pi/2$ there is no peak at $2k_1$ in the density distribution. The density is flat and only the $k = 0$ mode is occupied.

Now we take a look at the case where two modes are occupied. In this case we can write the wave function as

$$\begin{aligned}\psi(x) = {} & A_{R1}\cos(k_1 x + \phi_{R1}) + iA_{I1}\cos(k_1 x + \phi_{I1}) \\ & + A_{R2}\cos(k_2 x + \phi_{R2}) + iA_{I2}\cos(k_2 x + \phi_{I2})\end{aligned} \tag{A.3}$$

and the density is given by

$$\begin{aligned}\rho(x) &= |\psi(x)|^2 \\ &= \frac{A_{R1}^2}{2}(\cos 2k_1 x + 2\phi_{R1} + 1) + \frac{A_{I1}^2}{2}(\cos(2k_1 x + 2\phi_{I1}) + 1) \\ &\quad + \frac{A_{R2}^2}{2}(\cos 2k_2 x + 2\phi_{R2} + 1) + \frac{A_{I2}^2}{2}(\cos(2k_2 x + 2\phi_{R2}) + 1) \\ &\quad + A_{R1}A_{R2}\left(\cos(k_1 + k_2)(\phi_{R1} + \phi_{R2}) + \cos(k_1 - k_2)(\phi_{R1} - \phi_{R2})\right) \\ &\quad + A_{I1}A_{I2}\left(\cos(k_1 + k_2)(\phi_{I1} + \phi_{I2}) + \cos(k_1 - k_2)(\phi_{I1} - \phi_{I2})\right) . \quad \text{(A.4)}\end{aligned}$$

The first two lines correspond again to the occupation of the $k = 0$ mode and the $2k_1$ and $2k_2$ modes in the density. However, the bottom two lines show new effects. It is possible that one observes modes in the density with $k_+ = k_1 + k_2$ or $k_- = k_1 - k_2$, but it is also possible that the terms cancel out. The mode k_- explains why we see in the density-density correlations always a peak around $k = 0$. The excited modes in the wave function have a finite momentum range and hence their are contribution where k_- is almost zero.

A.2 Grid momentum

In our simulations both a part of the time evolution and a part of the calculation of the observable are carried out in Fourier space. In this work, we use grid momenta which are not distributed linearly in Fourier space. One can derive them if one calculates the discrete, second order spatial derivative of the wave function:

$$\begin{aligned}\frac{\mathrm{d}^2}{\mathrm{d}x^2}\psi(x_j) &= \frac{\frac{\mathrm{d}}{\mathrm{d}x}\psi(x_{j+1}) - \frac{\mathrm{d}}{\mathrm{d}x}\psi(x_j)}{x_{j+1} - x_j} \\ &= \frac{\left(\frac{\psi(x_{j+1}) - \psi(x_j)}{x_{j+1} - x_j}\right) - \left(\frac{\psi(x_j) - \psi(x_{j-1})}{x_j - x_{j-1}}\right)}{x_{j+1} - x_j} \\ &= \frac{\psi(x_{j+1}) - 2\psi(x_j) + \psi(x_{j-1})}{(\Delta x)^2} . \quad \text{(A.5)}\end{aligned}$$

where $x_{j+1} - x_j = x_j - x_{j-1} = \Delta x$ was used. After a transformation into Fourier space $\psi(x_j) = 1/N \sum_k \psi(k) \exp(-i2\pi kj/N)$ one gets

$$\begin{aligned}\frac{\mathrm{d}^2}{\mathrm{d}x^2}\psi(x_j) &= \frac{1}{N(\Delta x)^2}\sum_k \psi(k)\left(e^{-i2\pi k(j+1)/N} - 2e^{-i2\pi kj/N} + e^{-i2\pi k(j-1)/N}\right) \\ &= \frac{1}{N(\Delta x)^2}\sum_k \psi(k)e^{-i2\pi kj/N}\left(e^{-i2\pi k/N} - 2 + e^{i2\pi k/N}\right) \\ &= -\frac{4}{(\Delta x)^2}\sin^2\left(\frac{\pi n}{N}\right)\psi(x_j) \stackrel{!}{=} -k^2\psi(x_j) \end{aligned} \tag{A.6}$$

In Fourier space the momentum is given by

$$k_n = \frac{2}{\Delta x}\sin\left(\frac{\pi n}{N}\right) \tag{A.7}$$

with $n \in [-N/2, N/2-1]$. For small n the sin-function is almost linear and the momenta are equally spaced. For high momenta the spacing is denser. The highest momentum is $2/\Delta x$ and not $\pi/\Delta x$ as in the linear case.

Bibliography

[1] S. N. Bose, "Plancks Gesetz und Lichtquantenhypothese," *Z. Phys.* **26** no. 3, (1924) . [Am. J. Phys. 44, 1056 (1976)].

[2] A. Einstein, "Quantentheorie des einatomigen idealen Gases," *Sitzungsber. Kgl. Preuss. Akad. Wiss., Phys. Math. Kl.* **1924** (July, 1924) .

[3] M. H. Anderson, J. R. Ensher, M. R. Matthews, C. E. Wieman, and E. A. Cornell, "Observation of Bose-Einstein Condensation in a Dilute Atomic Vapor," *Science* **269** (July, 1995) .

[4] D. M. Stamper-Kurn, M. R. Andrews, A. P. Chikkatur, S. Inouye, H.-J. Miesner, J. Stenger, and W. Ketterle, "Optical confinement of a Bose-Einstein condensate," *Phys. Rev. Lett.* **80** (Mar., 1998) .

[5] J. Sabbatini, W. H. Zurek, and M. J. Davis, "Phase separation and pattern formation in a binary Bose-Einstein condensate." Phys. rev. lett. 107, 230402 (2011), 2011.

[6] E. Nicklas, H. Strobel, T. Zibold, C. Gross, B. A. Malomed, P. G. Kevrekidis, and M. K. Oberthaler, "Rabi Flopping Induces Spatial Demixing Dynamics," *Phys. Rev. Lett.* **107** (Nov, 2011) .

[7] J. Berges, S. Borsányi, and C. Wetterich, "Prethermalization," *Phys. Rev. Lett.* **93** (Sep, 2004) .

[8] R. Barnett, A. Polkovnikov, and M. Vengalattore, "Prethermalization in quenched spinor condensates," *Phys. Rev. A* **84** (Aug, 2011) .

[9] J. Berges, A. Rothkopf, and J. Schmidt, "Nonthermal Fixed Points: Effective Weak Coupling for Strongly Correlated Systems Far from Equilibrium," *Phys. Rev. Lett.* **101** (2008) .

[10] B. Nowak, D. Sexty, and T. Gasenzer, "Superfluid turbulence: Nonthermal fixed point in an ultracold Bose gas," *Phys. Rev. B* **84** (2011) , `arXiv:1012.4437v2 [cond-mat.quant-gas]`.

[11] M. Karl, B. Nowak, and T. Gasenzer, "Universal scaling at non-thermal fixed points of a two-component Bose gas," *Phys.Rev.* **A88** (2013) , `arXiv:1307.7368 [cond-mat.quant-gas]`.

[12] S. Burger, K. Bongs, S. Dettmer, W. Ertmer, K. Sengstock, A. Sanpera, G. V. Shlyapnikov, and M. Lewenstein, "Dark Solitons in Bose-Einstein Condensates," *Phys. Rev. Lett.* **83** (Dec, 1999) .

[13] M. Schmidt, S. Erne, B. Nowak, D. Sexty, and T. Gasenzer, "Non-thermal fixed points and solitons in a one-dimensional Bose gas," *New Journal of Physics* **14** no. 7, (2012) .

[14] A. E. Leanhardt, A. Görlitz, A. P. Chikkatur, D. Kielpinski, Y. Shin, D. E. Pritchard, and W. Ketterle, "Imprinting Vortices in a Bose-Einstein Condensate using Topological Phases," *Phys. Rev. Lett.* **89** (Oct, 2002) .

[15] J. Stenger, S. Inouye, D. M. Stamper-Kurn, H.-J. Miesner, A. P. Chikkatur, and W. Ketterle, "Spin domains in ground-state Bose-Einstein condensates," *Nature* **396** no. 6709, (Nov., 1998) .

[16] H. Saito, Y. Kawaguchi, and M. Ueda, "Topological defect formation in a quenched ferromagnetic Bose-Einstein condensates," *Phys. Rev. A* **75** (Jan, 2007) .

[17] B. Nowak, S. Erne, M. Karl, J. Schole, D. Sexty, and T. Gasenzer, "Non-thermal fixed points: universality, topology, & turbulence in Bose gases," *arXiv preprint arXiv:1302.1448* (2013) .

[18] M. Karl, B. Nowak, and T. Gasenzer, "Tuning universality far from equilibrium," *Scientific Reports* **3** (Aug., 2013) , `arXiv:1302.1122 [cond-mat.quant-gas]`.

[19] J. Berges and G. Hoffmeister, "Nonthermal fixed points and the functional renormalization group," *Nuclear Physics B* **813** no. 3, (2009) .

[20] T. Ohmi and K. Machida, "Bose-Einstein Condensation with Internal Degrees of Freedom in Alkali Atom Gases," *Journal of the Physical Society of Japan* **67** no. 6, (1998) .

[21] T.-L. Ho, "Spinor Bose condensates in optical traps," *Phys. Rev. Lett.* **81** (Jul, 1998) .

[22] W. Zhang, D. L. Zhou, M.-S. Chang, M. S. Chapman, and L. You, "Dynamical Instability and Domain Formation in a Spin-1 Bose-Einstein Condensate," *Phys. Rev. Lett.* **95** (Oct, 2005) .

[23] Y. Kawaguchi and M. Ueda, "Spinor Bose-Einstein condensates," *Physics Reports* **520** no. 5, (2012) .

[24] Q. Gu and R. A. Klemm, "Ferromagnetic phase transition and Bose-Einstein condensation in spinor Bose gases," *Phys. Rev. A* **68** (Sep, 2003) .

[25] D. M. Stamper-Kurn and M. Ueda, "Spinor Bose gases: Symmetries, magnetism, and quantum dynamics," *Rev. Mod. Phys.* **85** (Jul, 2013) .

[26] K. Fujimoto and M. Tsubota, "Spin turbulence in a trapped spin-1 spinor Bose-Einstein condensate," *Phys. Rev. A* **85** (May, 2012) .

[27] K. Fujimoto and M. Tsubota, "Counterflow instability and turbulence in a spin-1 spinor Bose-Einstein condensate," *Phys. Rev. A* **85** (Mar, 2012) .

[28] Y. Aoki and M. Tsubota, "Spin Turbulence Made by the Oscillating Magnetic Field in a Spin-1 Spinor Bose-Einstein Condensate," *Journal of Low Temperature Physics* **171** no. 3-4, .

[29] S. Kobayashi, M. Kobayashi, Y. Kawaguchi, M. Nitta, and M. Ueda, "Abe homotopy classification of topological excitations under the topological influence of vortices," *Nuclear Physics B* **856** no. 2, (2012) .

[30] M. Kobayashi, Y. Kawaguchi, and M. Ueda, "Vortex Tiling in a Spin-2 Spinor Bose-Einstein Condensate," *arXiv preprint arXiv:0907.3716* (2009) .

[31] Sadler L. E., Higbie J. M., Leslie S. R., Vengalattore M., and Stamper-Kurn D. M., "Spontaneous symmetry breaking in a quenched ferromagnetic spinor Bose-Einstein condensate," *Nature* **443** no. 7109, (Sep, 2006) . 10.1038/nature05094.

[32] "Parameters and results are taken from the group of Prof. Dr. Markus K. Oberthaler at the Kirchhoff Institute for Physics in Heidelberg. The experiments are carried out by Wolfgang Müssel, Helmut Strobel, Daniel Linnemann, Maximilian Prüfer, Philipp Kunkel and Sören Bieling,".

[33] S. Uchino, M. Kobayashi, and M. Ueda, "Bogoliubov theory and Lee-Huang-Yang corrections in spin-1 and spin-2 Bose-Einstein condensates in the presence of the quadratic Zeeman effect," *Phys. Rev. A* **81** (Jun, 2010) .

[34] C. Mora and Y. Castin, "Extension of Bogoliubov theory to quasicondensates," *Phys. Rev. A* **67** (May, 2003) .

[35] J. Berges and J. Serreau, "Parametric Resonance in Quantum Field Theory," *Phys. Rev. Lett.* **91** (Sep, 2003) .

[36] J. Berges, K. Boguslavski, and S. Schlichting, "Nonlinear amplification of instabilities with longitudinal expansion," *Phys. Rev. D* **85** (Apr, 2012) .

[37] S. Y. Khlebnikov and I. I. Tkachev, "Classical Decay of the Inflaton," *Phys. Rev. Lett.* **77** (Jul, 1996) .

[38] J. H. Traschen and R. H. Brandenberger, "Particle production during out-of-equilibrium phase transitions," *Phys. Rev. D* **42** (Oct, 1990) .

[39] R. Micha and I. I. Tkachev, "Relativistic Turbulence: A Long Way from Preheating to Equilibrium," *Phys. Rev. Lett.* **90** (Mar, 2003) .

[40] J. Berges and D. Sexty, "Strong versus weak wave-turbulence in relativistic field theory," *Phys. Rev. D* **83** (2011) .

[41] H. Fujii, K. Itakura, and A. Iwazaki, "Instabilities in non-expanding glasma," *Nuclear Physics A* **828** no. 1–2, (2009) .

[42] S. Mrówczyński and B. Müller, "Reheating after supercooling in the chiral phase transition," *Physics Letters B* **363** no. 1–2, (1995) .

[43] W. Zhang, D. L. Zhou, M.-S. Chang, M. S. Chapman, and L. You, "Coherent spin mixing dynamics in a spin-1 atomic condensate," *Phys. Rev. A* **72** (Jul, 2005) .

[44] A. Widera, F. Gerbier, S. Fölling, T. Gericke, O. Mandel, and I. Bloch, "Precision measurement of spin-dependent interaction strengths for spin-1 and spin-2 87 Rb atoms," *New Journal of Physics* **8** no. 8, (2006) .

[45] P. B. Blakie, A. S. Bradley, M. J. Davis, R. J. Ballagh, and C. W. Gardiner, "Dynamics and statistical mechanics of ultra-cold Bose gases using c-field techniques," *Adv. Phys.* **57** (09, 2008) , `arXiv:0809.1487v2 [cond-mat.stat-mech]`.

[46] J. Berges and T. Gasenzer, "Quantum versus classical statistical dynamics of an ultracold Bose gas," *Phys. Rev. A* **76** (Sep, 2007) .

[47] E. Gross, "Classical theory of boson wave fields," *Annals of Physics* **4** no. 1, (1958) .

[48] M. Brewczyk, M. Gajda, and K. Rzażewski, "Classical fields approximation for bosons at nonzero temperatures," *Journal of Physics B: Atomic, Molecular and Optical Physics* **40** no. 2, (2007) .

[49] A. Polkovnikov, "Phase space representation of quantum dynamics," *Annals of Physics* **325** no. 8, (2010) .

[50] J. W. Cooley and J. W. Tukey, "An algorithm for the machine calculation of complex Fourier series," *Mathematics of computation* **19** no. 90, (1965) .

[51] J. P. McKelvey, "Simple transcendental expressions for the roots of cubic equations," *American Journal of Physics* **52** no. 3, (1984) .

[52] W. H. Press, *Numerical recipes : the art of scientific computing*. Cambridge University Press, Cambridge, UK; New York, 2007.

[53] E. J. Putzer, "Avoiding the Jordan canonical form in the discussion of linear systems with constant coefficients," *The American Mathematical Monthly* **73** no. 1, (Jan., 1966) .

[54] S. Heupts, " Nonequilibrium dynamics of an ultracold spin-1 Bose gas," *Master Thesis* (2014) .

[55] N. N. Bogoliubov, "," *J.Phys.(U.S.S.R.)* (1947) .

[56] T.-L. Ho, "Spinor Bose Condensates in Optical Traps," *Phys. Rev. Lett.* **81** (Jul, 1998) .

[57] V. Zakharov and A. Shabat, "Exact theory of two-dimensional self-focusing and one-dimensional self-modulation of wave in nonlinear media," *JETP* no. 34:62, (1972) .

[58] P. O. Fedichev, A. E. Muryshev, and G. V. Shlyapnikov, "Dissipative dynamics of a kink state in a Bose-condensed gas," *Phys. Rev. A* **60** (Oct, 1999) .

[59] J. Ieda, T. Miyakawa, and M. Wadati, "Exact Analysis of Soliton Dynamics in Spinor Bose-Einstein Condensates," *Phys. Rev. Lett.* **93** (Nov, 2004) .

[60] D. Zhao, S.-W. Song, L. Wen, Z.-D. Li, H.-G. Luo, and W.-M. Liu, "Topological defects and inhomogeneous spin patterns induced by the quadratic Zeeman effect in spin-1 Bose-Einstein condensates," *Phys. Rev. A* **91** (Jan, 2015) .

[61] D. A. Smith, M. Gring, T. Langen, M. Kuhnert, B. Rauer, R. Geiger, T. Kitagawa, I. Mazets, E. Demler, and J. Schmiedmayer, "Prethermalization revealed by the relaxation dynamics of full distribution functions," *New Journal of Physics* **15** no. 7, (2013) .

[62] J. M. Cornwall, R. Jackiw, and E. Tomboulis, "Effective action for composite operators," *Phys. Rev. D* **10** (Oct, 1974) .

[63] Chang Ming-Shien, Qin Qishu, Zhang Wenxian, You Li, and Chapman Michael S., "Coherent spinor dynamics in a spin-1 Bose condensate," *Nat Phys* **1** no. 2, (Nov, 2005) . 10.1038/nphys153.

[64] Gerving C.S., Hoang T.M., Land B.J., Anquez M., Hamley C.D., and Chapman M.S., "Non-equilibrium dynamics of an unstable quantum pendulum explored in a spin-1 Bose-Einstein condensate," *Nat Commun* **3** (Nov, 2012) .

Danksagung

An dieser Stelle möchte ich mich bei all denjenigen bedanken, die mich bei der Anfertigung meiner Masterarbeit unterstützt haben.

Ganz besonderer Dank gilt Herrn Prof. Thomas Gasenzer für die Möglichkeit in einem aktuellen und spannenden Forschungsgebiet mitzuarbeiten. Außerdem möchte ich mich für die vielen interessanten Gespräche und die hilfreichen Tipps bedanken.

Desweiteren möchte ich Herrn Prof. Markus Oberthaler für die spannenden Diskussionen und die Zweitkorrektur meiner Arbeit danken. In diesem Zusammenhang möchte ich mich auch bei allen Mitgliedern der Bosonic Quantum Gases Gruppe bedanken. Die Zusammenarbeit mit Experimenatoren hat diese Arbeit stark bereichert und mir interessante Einblicke in die Physik im Labor gegeben.

Besonders möchte ich Markus Karl, Andreas Elben und meiner Mutter, Gisela Klenner, für das ausführliche Korrekturlesen meiner Arbeit danken.

Zuletzt möchte ich mich bei der gesamten Arbeitsgruppe und allen Keller-Büro-Kollegen bedanken, die mir nicht nur bei physikalischen und numerischen Problemen sehr geholfen haben.

Erklärung

Ich versichere, dass ich diese Arbeit selbstständig verfasst habe und keine anderen als die angegebenen Quellen und Hilfsmittel benutzt habe.

Heidelberg, den 24.07.2015 .....